Analysis of Systems for Superimposing Projected Images

Amir Said
Media Technologies Laboratory
HP Laboratories Palo Alto
HPL-2006-129
October 5, 2006*

display, signal synthesis, optical signal processing, image generation, deconvolution, wobulation

The addressable resolution of digital projectors can be increased by using a technique called "wobulation," which consists of using mechanical actuators to rapidly shift projected images (subframes) by fractions of pixel lengths, in one or two directions. This way the visual quality of the superimposed subframes can be improved without changing the expensive spatial light modulators. While experimental tests demonstrate the practical feasibility and the visual improvement, there is still a need to develop theoretical tools for better understanding the potential and limitations of this technique. For instance, it is desirable to know how much resolution improvement can be achieved. This is a signal design problem that is quite different from the restoration problem that results from moving camera sensors. The objective of this work is to introduce some analytical tools, including mathematical models that contain with reasonable accuracy all important practical factors, and that are simple enough for providing good intuition about the problem. Using these models we show that we can rigorously settle some of the questions concerning the range of images and resolution that can be achieved. We also discuss the linear and nonlinear factors involved and how they affect the stability of the signal design methods.

* Internal Accession Date Only
Approved for External Publication

Analysis of Systems for Superimposing Projected Images

Amir Said[1]
Hewlett Packard Laboratories
Palo Alto, CA

[1]**Important note:** *Due to the interest that the draft of this report received, it is being published before all its chapters are finished. In the current version (1.0) chapters 1 to 5 are mostly complete, but there some new results that have not been included yet. The remaining chapters contain mostly an indication of their planned content. Please contact the author (said@hpl.hp.com) for information about corrections and the publication of new versions.*

Abstract

Many visualization applications require digital displays and projectors with very high resolution, and one well-known technique to increase resolution is to spatially arrange several projected images in a tiling configuration. Less known is the fact that projectors also allow a very different type of solution, called "wobulation," which is the superimposition of several projections, each shifted from the others by displacements of a fraction of the pixel size. Such precise positioning can be achieved, for instance, moving the projection elements in time using optical methods. For optimal results this method requires sophisticated pre-processing of the images that are to be projected, taking into account all the combination effects caused by the superimposition, in order to properly produce the desired high-resolution projection.

In this work we study the properties of image superimposition systems, and analyze the determination of the optimal signals to be projected and the techniques for their computation. We show that basically the behavior of the superimposition system can be decomposed in two components. The first is linear, and corresponds to the addition of light intensities. The second is defined by the upper and lower limits in light output, and is nonlinear. The first component can be modeled as a linear dynamic system, which is spatially-invariant if identically shifted images are used, and can be evaluated using basic signal processing techniques. This analysis shows potential problems concerning the existence of solutions and stability of the computations. Next, we develop more realistic models, incorporating the nonlinear behavior, which require optimization techniques and algorithms. While the resulting problems are common in optimization, the imaging problem has very large dimensions, with typically millions of variables and constraints. We study solution methods that can exploit the particularities and sparsity of the problems, and that can cope with the fact that the problems may be numerically ill-conditioned. Finally, we consider methods to improve numerical stability and convergence speed, and show numerical results.

The numerical results indicate that typically, when the subframes are arranged for modest gains in resolution (e.g., twice the original resolution), the system's behavior is dominated by the linear component, and the desired gains in resolution are mostly achieved for many typical types of image. On the other hand, the systems designed for obtaining more than three times the original resolution are much more severely limited by the nonlinear component, and for most images it quickly becomes more difficult to improve resolution.

Contents

Chapter 1

Introduction

1.1 Motivation

While there is little need to stress the significance of the visual component in human communications, the importance of visualization is increasing in a very wide range of human activities, including many that were considered too abstract to be helped by visual means [21, 25, 27, 33].

The economic worth of these visualization applications should be clear when we consider that, in some form or another, they touch virtually every major industry. For instance, the worldwide market for just the interactive data visualization tools (software) is expected to reach about $7 billion in 2007 [39], and the market for large displays is expected to reach $7 billion in 2008 [40]. The total market value, including all the different visualization applications, hardware, software, and services, is of course much larger.

In many of these applications it is very desirable to convey as much visual information at each time as possible, and this requires a combination of large display areas and high resolutions [29]. In fact, some experiments show that for some applications there are great advantages of using "immersive" visualization environments, in which the displays cover, for instance, the walls of a room [11, 35].

An important factor limiting the deployment of such visualization tools is that digital displays and projection systems have costs that tend to grow very steeply at high resolutions.[1] This is important because of the competition with printed media, which lacks the dynamic updating component, but is still one of the most cost-effective methods for visualization.

The motivation of this work is to study one technique, the superimposition of

[1] Appendix A presents an example of a simple cost analysis showing why this behavior is expected.

projected images [44] (also called "wobulation"), which has the potential to greatly reduce the costs of some visualization systems.

1.2 Increasing Image Resolution

A well-known technique for increasing the resolution of digital displays using projectors is called tiling:

- Divide the original image with resolution $W \times H$ into a rectangular grid of $M \times N$ subimages, and use MN projectors, each with resolution $(W/M) \times (H/N)$, to render each of the subimages.

(There is vast literature on the subject, see [30, 31, 32, 36, 42] for some examples.)

Projectors are also allow a very different type of solution for increasing resolution ("wobulation") [44]:

- Use MN images, each with resolution $(W/M) \times (H/N)$, to display full-size images that are superimposed, each displaced by a subpixel spatial shift, in order to create MN possible combinations in each spatial area corresponding to MN pixels at the full resolution (superimposition).

Figure 1.1 shows examples of these two techniques, for a set of 2×2 projected images. Reference [44] contains some practical details about how "wobulation" was implemented in digital projectors, and includes photos of images created using this technique in a digital projector. Following the terminology used in [44], throughout this document we call each of the images to be superimposed a *subframe.*

For each of these two techniques for increasing resolution it is important to consider the brightness and contrast of the final projected image, which are basically defined by projector technology and the number of subframes used. In addition, the two solutions should be compared in terms of implementation cost and image quality. In this document we are mostly interested in the signal processing problems, and thus we frequently use normalizations to simplify the analysis, considering that there is another analysis for deciding product specifications.

We also assume that there are solutions to the problem of aligning the projected images within a certain pre-defined accuracy. We understand that there are complex problems that can be created due to errors in alignment, but we focus on finding out what is achievable when there is exact positioning.

As shown in Figure 1.1, for the tiling method it is common to allow a small overlap of the projected images in order to create a seamless image. The main tech-

(a) Shifted images with small overlap

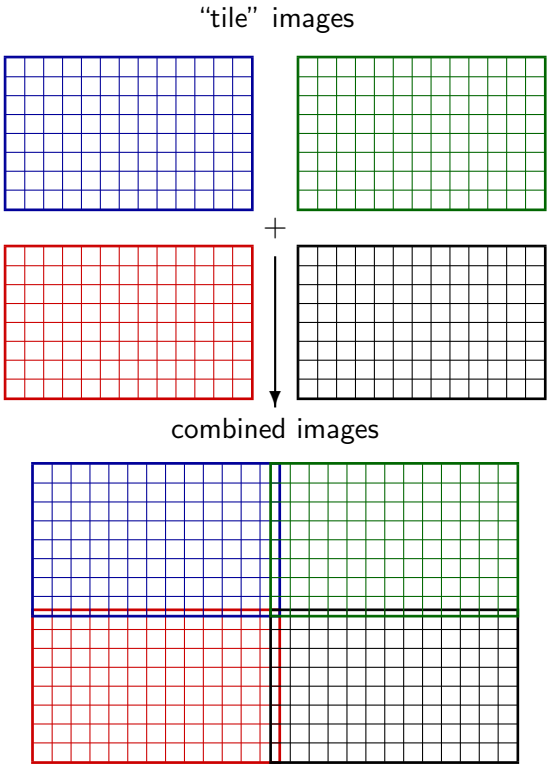

(b) Superimposed images with small shifts

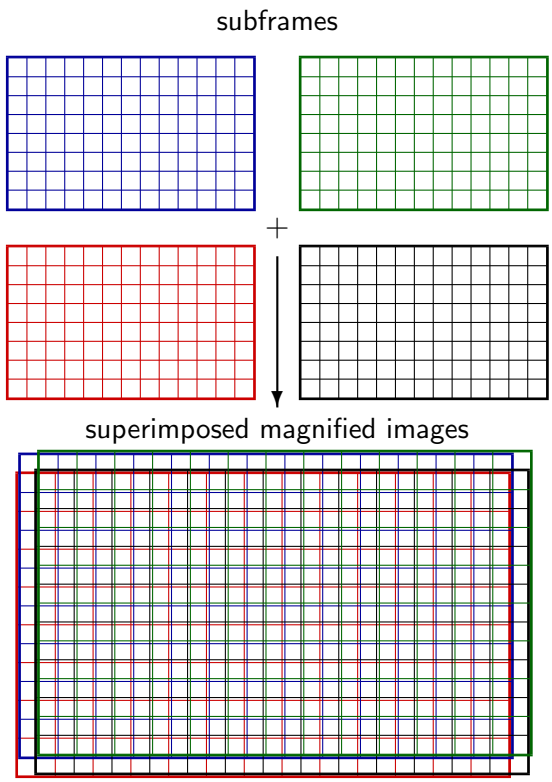

Figure 1.1: Two methods for increasing the resolution of digital projection systems, using 2×2 tiled or superimposed images.

nical challenge is to process the images to be projected in order to eliminate visual artifacts [30, 31, 32, 36, 42]. Among the practical problems we have

- The overlapping regions of the tiled images need to have their luminosity profile changed (edge-blended) to create a seamless projected image.
- Due to unavoidable differences in the light sources, even if the same type of projector is used, without proper calibration the projected images commonly have perceptible differences in brightness and in color.

Thus, while the tiling technique makes it nearly trivial to divide the signals among the subframes, and the increase in resolution is very well defined, there are still challenging technical problems on how to create a single high-quality image.

The technique of superimposing images, on the other hand, is definitely less intuitive, requiring much more sophisticated methods to determine what each subframe should be. In fact, good knowledge of signal processing techniques is needed just to understand the possibility of increase in resolution. As a preview of the results presented in this document, Figure 1.2 shows an example of four subframes that were computed to optimize the visual quality of the image generated by the superposition of 2×2 subframes (as shown in the diagram of Figure 1.1(b)), shifted by half-pixel length in the horizontal and vertical directions.

Note that the individual images to be superimposed (subframes) seem to be very "noisy," with many color pixels that look artificial and out of place. However, when these four images are superimposed in the correct arrangement, with proper horizontal and vertical half-pixel shifts, they produce the image shown in Figure 1.3(a). For reference, Figure 1.3(b) shows the image that would be produced by a projector with twice the horizontal and vertical resolutions,[2] Figure 1.3(c) shows the corresponding image obtained using the projector with original resolution, and Figure 1.3(d) shows the superimposed image created by simply assigning every other pixel to each subframe (which we call "naïve").

From this example it is obvious that the superimposition technique can create images that have significantly more details than those that could be produced using the original resolution of the four subframes. However, we need to ask if the superimposition of the four subframes is indeed doubling the vertical and horizontal resolutions.

Figure 1.4 shows the enlargements of the same part of images (a) and (c), where we can see that the image produced by superimposition is indeed a good approximation of the image with double resolution, but we can also see that they are not identical. In this document we analyze image superimposition systems to define in which conditions

[2]This also corresponds to the image created by 2×2 overlapping tiled projectors (Figure 1.1(a)), in an area without overlapping artifacts.

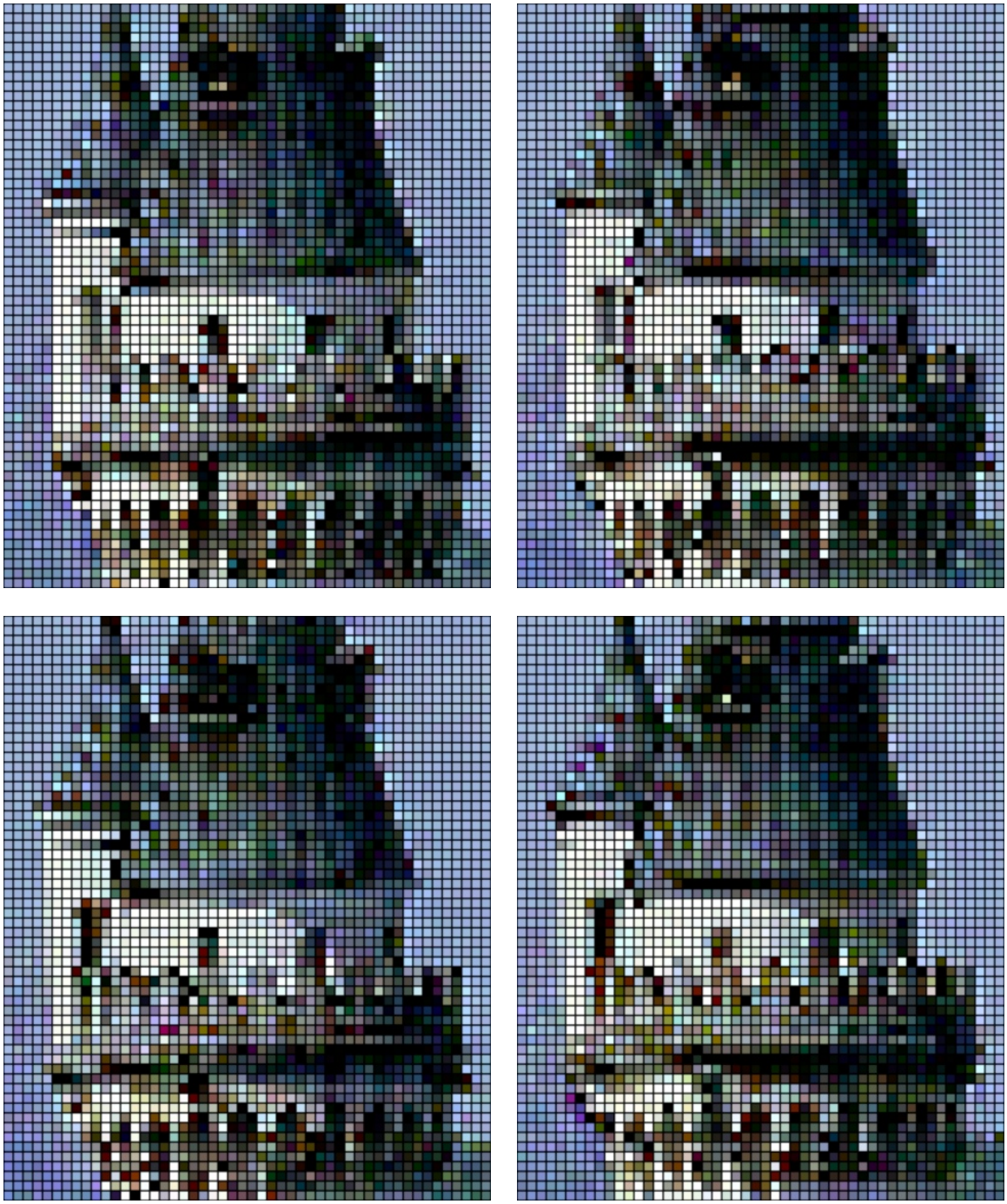

Figure 1.2: Example of subframes optimally designed for 2×2 superimposition, with half-pixel displacement in the horizontal and vertical directions.

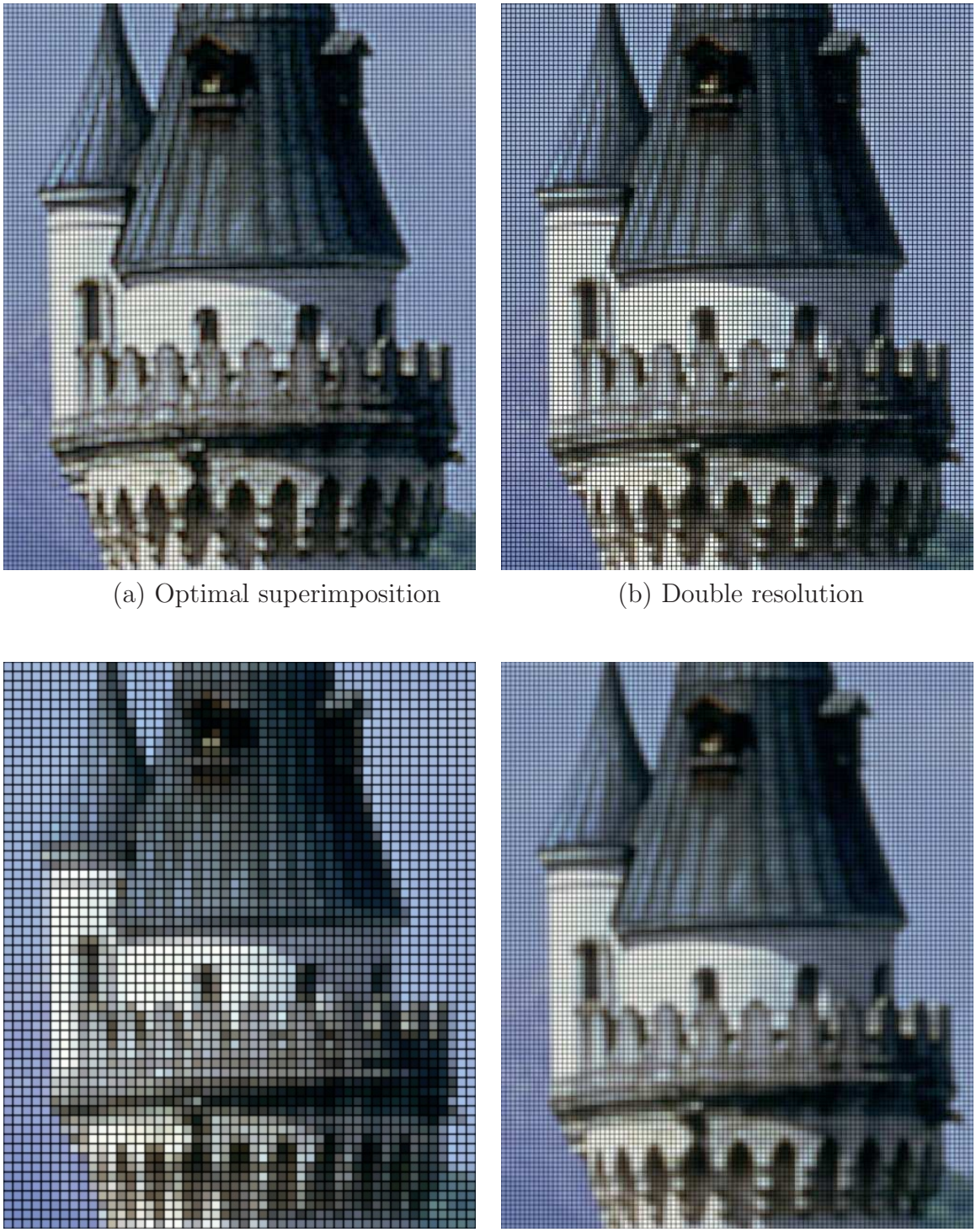

(a) Optimal superimposition (b) Double resolution

(c) Single resolution (d) Naïve design

Figure 1.3: Reference images for comparing the quality of the image generated by superimposed subframes.

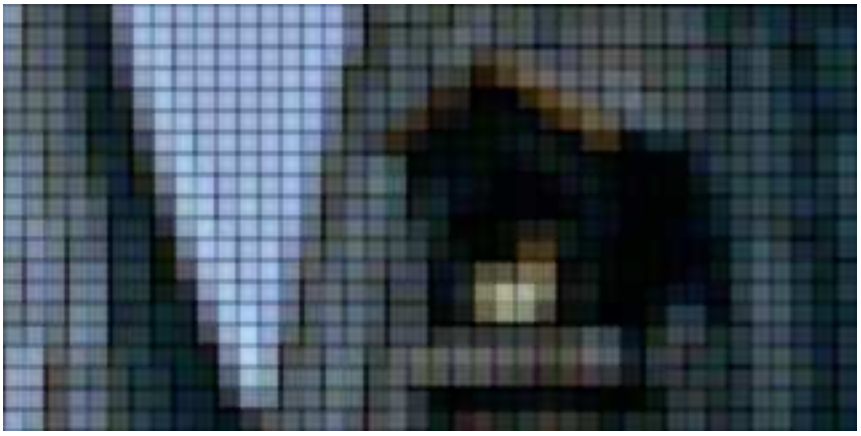

(a) Image resulting from superimposition of 2×2 subframes.

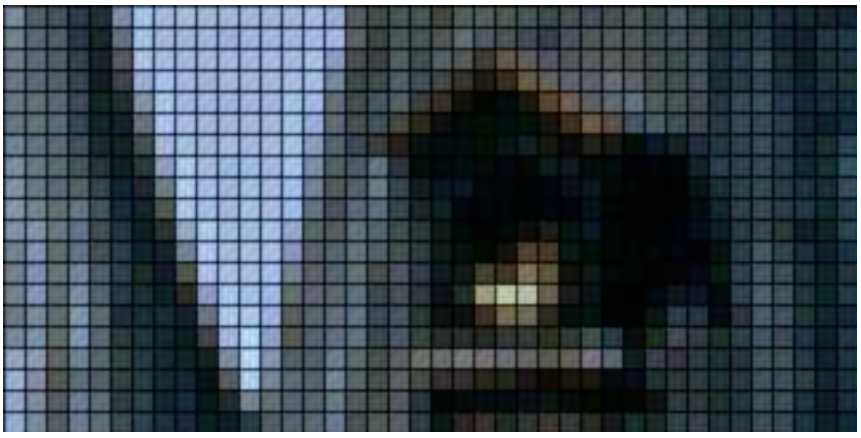

(b) Image from projector with twice the vertical and horizontal resolutions.

Figure 1.4: Magnification of a part of images (a) and (c) in Figure 1.3.

we would have an exact match, and if they can be achieved in practical situations. We also study the visual quality of the resulting images, to determine if the differences are indeed important.

In the next sections we provide a summary of the technical problems that need to be solved for effectively using this multi-projection system.

1.3 Prior Work

While there is a good amount of literature on the use of tiled projectors, there is very little analysis of image superimposition. Takahashi *et al.* describe a system [17] that

uses four subframes to create a high resolution image. However, they use a system in which the pixels are in fact interleaved, and there is no overlapping between pixels in different subframes. This may be a good choice only for projector technologies that are not light-efficient (as considered in [17]), since at most 25% of the light is utilized.

Majumder [43] considers the superimposition case in which the pixels may overlap, and concludes that it cannot possibly produce a projected image with resolution increased by a factor equal to the number of projectors, unless there is no overlap between the pixels of different projected images. Furthermore, Majumder seems unaware of the optical methods used in [17, 44], and assumes that even such approach would be impractical.

The analysis in [43] does not take into account important facts about the generation of the images to be superimposed, and either uses excessively stringent conditions regarding aliasing, or ignores that in many situations alias cancellation is possible. In Appendix D we present a discussion of that article. The examples in Figures 1.3 and 1.4 show a compelling example that, even if exact reproductions at the maximum achievable resolution are not possible, we still can obtain images that look significantly better and more detailed.

There is also a significant amount of earlier work on the equivalent of image superimposition for printers [16, 19, 20]. Printing devices share some characteristics with displays and projectors, related to visual quality and resolution. However, printers use a subtractive system with inks and dyes, and the result of their combination on paper or other media is quite complicated, and certainly not linear like the addition of light from superimposed projections. For this reason the printer solutions are mostly empiric, and commonly use a form of table look-up for determining good combinations.

1.4 Technical Challenges

Creating a reasonably accurate model of the superimposition of projected images is much simpler than modeling the printing system because

(a) When several projected images are superimposed, the light intensity in each area is simply the sum of the contributions from each subframe;

(b) Digital projectors are designed so that the light intensity of each image element (pixel) is, with good accuracy, a linear function of its input signal (defined in terms of light intensity).

Consequently, as we show in details later, even complicated subframe arrangements in the end result in linear models: a vector with the average light intensities in the

combined image, $\mathbf{s}$, is always the result of the multiplication of a vector with all the subframe input signals, $\mathbf{c}$, with a matrix $\mathbf{H}$, plus a minimum amount of light, $s_{\min}$. Formally, we have simply

$$\mathbf{s} = \mathbf{H}\,\mathbf{c} + s_{\min}\,\mathbf{1}. \tag{1.1}$$

In this form, the main challenge in modeling the superimposition system is to determine the elements of matrix H. Similarly, the problem of computing the optimal subframe signals, in the sense that the combined image $\mathbf{s}$ is the best approximation to a reference image $\mathbf{r}$ can be simply stated as an optimization problem in the form

$$\begin{array}{ll} \text{Minimize}_{\mathbf{c}} & D(\mathbf{s}, \mathbf{r}), \\ \text{subject to} & \mathbf{s} = \mathbf{H}\mathbf{c} + s_{\min}\,\mathbf{1}, \\ & \mathbf{0} \leq \mathbf{c} \leq \mathbf{1}. \end{array} \tag{1.2}$$

where $D(\cdot, \cdot)$ is a function that measures the difference between two vectors, like the Euclidean distance, and $\mathbf{0}$ and $\mathbf{1}$ are vectors with all elements equal to 0 and 1, respectively. The inequality constraints represent the fact that each projected image has a limited range of light intensity. In this formulation we are assuming that $\mathbf{H}$ and $\mathbf{r}$ have been normalized such that $[0, 1]$ represents the full interval between minimum and maximum light intensity values.

Later we analyze the properties of this type of optimization problem and of the solution methods. However, we also would like to have more than numerical solutions—we want to have a good understanding of the problem structure, and the type of solutions that can be found. For instance, when we presented the example in Figure 1.4 we already said that it may not be always possible to have $\mathbf{s} = \mathbf{r}$. Thus, it is interesting to know why this happens, what kind of image differences we can expect, and how they are affected by different subframe configurations.

One difficulty with optimization problem (1.2) is that the set of inequality constraints makes it hard to predict the type of solution we can expect. If we ignore those constraints, and use some simple metrics like mean squared-error, we can always obtain a closed-form solution like

$$\mathbf{c} = \mathbf{H}^{+}\,(\mathbf{r} - s_{\min}\,\mathbf{1}), \tag{1.3}$$

where matrix $\mathbf{H}^{+}$ is a generalized inverse [1, 9, 14] of matrix $\mathbf{H}$.

However, unless we have a good knowledge of the structure and properties of matrix $\mathbf{H}$, there is still little insight that is gained. We propose first considering the problem in a more abstract manner, assuming images with infinite size. We show that, defined in that form, the problem can be analyzed with standard signal processing tools, and yields a very good intuition of what type of solutions we can expect from (1.2) and (1.3).

In the first part of this work we show that, if we assume subframes that are equally spaced, then the projection system can be modeled as a simple linear, position-invariant system. This, in turn, indicates that the desired solution may be defined by a very simple, and possibly unique inverse filtering (or deconvolution) operation.

However, it is well known that inverse filtering in imaging problems can be ill-conditioned [2, § 6.1], and the difficulty of finding reasonable approximations depends on the type of system. In fact, we show that for image superimposition we have many common cases that always correspond to singular problems, and in general we expect to encounter some type of numerical instability. These simple facts already show that in some situations, even if we ignore the light intensity constrains (e.g., admit negative light intensity), we cannot find exact inverses. Thus, such analysis shows why the objective of creating a low-cost *exact* replacement of a high resolution projector, may not be achievable in practice.

Next, we show how some changes in the inverse filtering problem can restore stability, but they can potentially degrade performance. In all cases stability is restored by filtering out some high-frequency components, meaning that a significant part of the desired increase in resolution can be lost. One technical challenge is to determine how much change is allowed so that the new optimal solutions are a good approximation of those from problem (1.2). From studying the need for continuously increasing the attenuation of the high-frequency components as we add more shifted subframes to get more resolution, we can identify some fundamental limits on the effectiveness of the superimposition technique.

The mathematical analysis and simulations of the linear system show that it, as we try to get more resolution using more subframes, the problems become increasingly more numerically unstable. Any attempts to solve the problem ignoring the inequality constraints in (1.2) using linear filtering methods faces many obstacles. For instance, one straightforward solution is to reduce dynamic range of all subframes, allowing "safety regions" so that small values of overflow and underflow do not create visual artifacts. This, however, has only limited effectiveness, and creates a very undesirable reduction in contrast. Many studies have shown that the visual quality can be more affected by contrast than total brightness. In addition, contrast specification is very important, and low nominal contrast can greatly reduce the value of a product. Unfortunately, very significant reductions in contrast would be required if resolution is to be increased by significant values.

The conclusion is that the linear analysis is useful for insight, but we eventually need to solve a constrained optimization problem in the form (1.2). Using some commonly used forms for the objective function, like Euclidean distance, we have a "standard" form of optimization problem: a quadratic program with "box" constraints [10]. The practical problem in this case is that for the image superimposition application we typically have millions of variables and constraints.

Thus, another technical challenge is how to exploit the special properties of the problem, like sparsity, to solve the large-scale optimization problem, or at least obtain good approximations, with reasonable amounts of computation. For real world applications we need, in fact, real-time computations to obtain rates of 30, 60, or more frames per second.

One final aspect to be considered is the analysis of how the singularities of the linear systems may cause problems in the convergence of the optimization method. Nearly-singular systems produce inverse solutions with very large signal magnitudes, but those large values that have little effect in the final image quality. Similarly, without proper care, the optimization algorithm may spend lots of computation for small image quality improvements.

1.5 Contributions and Document Organization

In this section we describe the organization of this document, and identify in each part what are the main contributions and novel results.[3] Even though we do not aim to be overly formal, we present some of the main results as theorems, since this help to stress the novelty and importance of the result, and the organization of the proofs. It also makes it easier for cross-reference, since it allows references to specific concepts and general results, instead of full sections or equations.

In Chapter 2 we present a brief review of the basic concepts of image acquisition and representation. One of its main objectives is to establish the foundations for the discussion about image superimposition and also introduce the main conventions and the notation to be used throughout the document.

We begin analyzing the image superimposition problem in Chapter 3 by defining mathematical models. We start with very general models, which can represent a great variety of subframe configurations.

One important contribution in Chapter 3 is the identification of the fact that, for the projection configuration of highest interest, when the subframe signals are properly interleaved the resulting mathematical model is a simple linear dynamic system with a single position-invariant system function. This result is valid for non-separable two-dimensional systems, and it is also shown that a more general case can be analyzed with multirate linear dynamic system, that also has a single position-invariant impulse response.

[3] **Important note:** Due to the interest that the draft of this report received, it is being published before all its chapters are finished. In the current version (1.0) chapters 1 to 5 are mostly complete, but there some new results that had not been included yet. The remaining chapters contain mostly an indication of their planned content. Please contact the author (said@hpl.hp.com) for information about corrections and the publication of new versions.

Choices for finding solutions in the frequency domain are discussed in Chapter 4. In the special case when the subframes are set for maximum gains in resolution there is a straightforward solution using inverse filters, which are unique when they exist. However, as we later show in Chapter 5, in the image superimposition problem we can expect singularities or, at least, numerical instability. We discuss the problem of searching for approximations instead of exact solutions.

Chapter 2

Notation and Basic Imaging

In this chapter we start by defining the basic notation and conventions used in this document. We also use the opportunity to review some basic facts about image acquisition and reproduction. The objective is to introduce the notation related to images, and also cover a few important aspects concerning image quality. We discuss some of the reasons why, when we compare different types of display systems, the visual quality cannot be evaluated with a single specification, like display resolution.

2.1 Notation

In this document we use two types of notation. In the first part, we analyze only the linear component of image superimposition, and use standard signal processing tools and notation. Even though we should be always referring to images, which are of course finite, we consider the fact that images currently have dimensions large enough so that the border effects are of little interest to us. Consequently, at the risk of being a bit less intuitive, we assume that the images have infinite dimension. This greatly simplifies the notation, and still yields the desired understanding of the basic properties of the image superimposition dynamic system.

We adopt many of the conventions of Oppenheim and Schafer's signal processing textbook [5]. We use parenthesis and brackets to indicate, respectively, functions of continuous and discrete variables. For instance, $\psi(x)$ represents a function of continuous variable ($x \in \mathbb{R}$), while $h[n]$ represents a sequence, and n an integer number ($n \in \mathbb{Z}$). One difference is that we represent Fourier transforms in terms of frequencies instead of angular frequencies (i.e., f instead of $\omega = 2\pi f$).

We use the corresponding capital letters to represent the z-transform of a sequence,

as

$$H(z) \equiv \sum_{n=-\infty}^{\infty} h[n]\, z^{-n}, \quad z \in \mathbb{C}, \tag{2.1}$$

where $\mathbb{C}$ is the set of complex numbers. Defining $j \equiv \sqrt{-1}$, the Fourier Transform (FT) of sequence $h[n]$ is represented as

$$H(e^{j2\pi f}) \equiv \sum_{n=-\infty}^{\infty} h[n]\, e^{-j2\pi fn} = \sum_{n=-\infty}^{\infty} h[n]\, \left[\cos(2\pi fn) - j\sin(2\pi fn)\right]. \tag{2.2}$$

The Fourier transform of functions of continuous variables are also represented by capital letters (including Greek letters), and are defined as

$$\Phi(f) \equiv \int_{-\infty}^{\infty} \phi(x)\, e^{-j2\pi fx}\, \mathrm{d}x. \tag{2.3}$$

We prefer the notation of (2.2), having the Fourier transform of sequences depend on $e^{j2\pi f}$ instead of f, because it clearly shows the periodic nature of such transforms, and also helps to distinguish the Fourier transform of sequences from those of functions of continuous variables.

We use the same type of notation for functions of two variables that are related to images. For instance, $\psi(x, y)$ and $h[m, n]$ are, respectively, functions of continuous and integer variables, and we adopt the convention that the first variables (x and m) define the horizontal direction, and the second (y and n) the vertical direction.

For two dimensional Fourier transforms we use f and g to indicate the frequency variables corresponding to, respectively, the horizontal and vertical directions. Examples for functions of continuous and discrete variables are

$$\Phi(f, g) \equiv \int_{-\infty}^{\infty} \int_{-\infty}^{\infty} \phi(x, y)\, e^{-j2\pi(fx+gy)}\, \mathrm{d}x\, \mathrm{d}y, \tag{2.4}$$

$$H(e^{j2\pi f}, e^{j2\pi g}) \equiv \sum_{m=-\infty}^{\infty} \sum_{n=-\infty}^{\infty} h[m, n]\, e^{-j2\pi(fm+gn)}. \tag{2.5}$$

We use subscripts to represent indexes or parameters. For example, we can define a set of functions of a continuous variable as $\{\phi_{m,n}(\cdot)\}$, where m and n are integers in a given range, and $b_{\ell,\sigma}(\cdot)$ to represent functions defined from continuous parameters ℓ and σ. In order to differentiate functions or parameters used for similar purposes, we use superscripts in parenthesis. For instance, $u^{(x)}$ and $u^{(y)}$ represent parameters u that are related to respectively the horizontal and vertical directions.

When there is no danger of confusion, we try to "reuse" definitions whenever we have functions, variables, or parameters that are used for the same purpose, but in

different contexts. For example, we use the function $\phi(x, y)$ for representing pixel light intensity in the two-dimensional analysis, and use the function $\phi(x)$ for the one-dimensional case. Similarly, we remove the subscripts and superscripts when they are not necessary anymore. For example, if all functions in a set $\{\phi_m(x)\}$ are by definition equal, then we use $\phi(x)$ to represent this function.

In Chapter 7, when we incorporate the nonlinear component, we take into account the image dimensions, and use the notation that is conventionally used for linear algebra and optimization. For instance, we use italic letters to represent scalars, lowercase bold letters to represent vectors, and bold capital letters to represent matrices.

2.2 Image Acquisition and Reconstruction

In this section we present some very general models for image acquisition and reconstruction, which are meant to contain mostly the information that we need in our analysis of image superimposition. Thus, we only consider monochrome images, but the extension to color images is straightforward. References [23, 24, 34, 41] contain more information regarding practical image acquisition and reconstruction.

Figure 2.1 shows a diagram of digital image acquisition. We assume an infinite image represented by the light-intensity function $p(x, y)$, which is to be represented by the infinite set of pixel values [34, § 2]

$$r[m, n] \doteq \int_{-\infty}^{\infty} \int_{-\infty}^{\infty} p(x, y)\omega(m\delta - x, n\delta - y)\, \mathrm{d}y\, \mathrm{d}x, \quad m, n \in \mathbb{Z}, \tag{2.6}$$

where δ is the sampling interval, $\omega(x, y)$ is a function representing the filtering required for the analog to digital conversion, and $\mathbb{Z}$ is the set of integer numbers.

Note that to simplify the notation we are assuming a sampling grid with the same interval between samples in the horizontal and vertical directions. The function $\omega(x, y)$ is called the *point spread function*, and is defined by the type of camera, sensors, and optical system. The two-dimensional sequence of pixel values $r[m, n]$ corresponds to samples of the two-dimensional convolution

$$r_c(x, y) \doteq (p * \omega)(x, y) = \int_{-\infty}^{\infty} \int_{-\infty}^{\infty} p(u, v)\omega(x - u, y - v)\, \mathrm{d}u\, \mathrm{d}v, \tag{2.7}$$

in a rectangular lattice, i.e.,

$$r[m, n] = r_c(m\delta, n\delta). \tag{2.8}$$

Consequently, in the frequency domain we have

$$R_c(f, g) = P(f, g)\, \Omega(f, g), \tag{2.9}$$

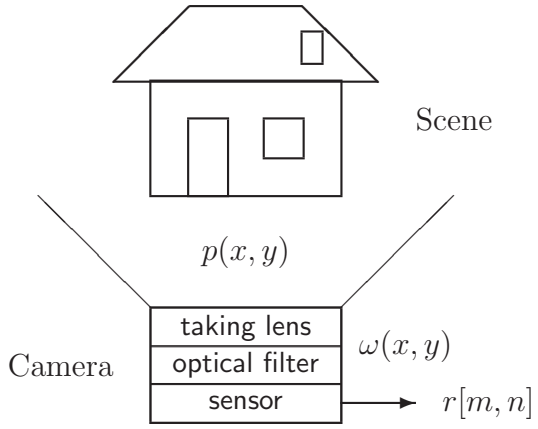

Figure 2.1: Model for image acquisition.

where $P(f, g)$ and $\Omega(f, g)$ are the Fourier transforms of $p(x, y)$ and $\omega(x, y)$. From the sampling theorem [34] we have

$$\begin{aligned} R(e^{j2\pi f}, e^{j2\pi g}) &\equiv \sum_{m=-\infty}^{\infty} \sum_{n=-\infty}^{\infty} r[m, n]\, e^{-j2\pi(fm+gn)} \qquad (2.10) \\ &= \frac{1}{\delta^2} \sum_{m=-\infty}^{\infty} \sum_{n=-\infty}^{\infty} P\left(\frac{f-m}{\delta}, \frac{g-n}{\delta}\right) \Omega\left(\frac{f-m}{\delta}, \frac{g-n}{\delta}\right). \end{aligned}$$

The light intensity of a displayed image is modeled as a linear combination of shifts of the *pixel light intensity profile* (PLIP) function $\phi(x, y)$ which represents the pattern of light intensity of each pixel in the display or projected image. In this model the reconstructed image, $\psi(x, y)$, is defined by

$$\psi(x, y) \doteq \delta^2 \sum_{m=-\infty}^{\infty} \sum_{n=-\infty}^{\infty} r[m, n]\phi(x - m\delta, y - n\delta). \qquad (2.11)$$

It is important to observe this linear model is valid only if the pixel values $r[m, n]$ correspond to actual light intensity. In standard forms, the grayscale or color components of an image are represented by intensity values that are converted using a nonlinear transformation meant to compensate for the "gamma" factor of CRT displays. At the same time the pixel intensity values are converted to integers, normally in the range [0..255], and stored using a single byte. In all our simulations we make sure that the gamma correction is correctly taken into account when converting from RGB pixel values. In Appendix B we provide references, and show some of the equations used for this conversion.

In the frequency domain we have

$$\begin{aligned}\Psi(f,g) &= \delta^2\,\Phi(f,g)\,R(e^{j2\pi\delta f},e^{j2\pi\delta g}) \\ &= \Phi(f,g)\sum_{m=-\infty}^{\infty}\sum_{n=-\infty}^{\infty} P\Big(f-\frac{m}{\delta},g-\frac{n}{\delta}\Big)\,\Omega\Big(f-\frac{m}{\delta},g-\frac{n}{\delta}\Big)\end{aligned} \tag{2.12}$$

This equation shows the fundamental facts of the Nyquist-Shannon sampling theorem: we can have $\psi(x,y) = p(x,y)$, i.e., no information is lost in the sampling process, only if [1]

1. $P(f,g) \neq 0$ only inside the region $f,g \in [-1/(2\delta), 1/(2\delta))$;
2. $\Phi(f,g)\,\Omega(f,g) = 1$ in the set $\{f,g : P(f,g) \neq 0\}$;
3. $\Phi(f,g) = 0$ in the set $\{f,g : P(f-m/\delta, g-n/\delta) \neq 0;\ m,n \in \mathbb{Z} - \{0\}\}$.

Since natural images are obviously not bandlimited, i.e., the first condition above is never satisfied, we conclude that perfect reconstruction cannot be achieved in imaging applications. Furthermore, there are many other factors that distinguish the design of imaging systems from the mathematical analysis of perfect reconstruction sampling.

First, there are also problems with redefining the problem to cases in which only $P(f,g)\Omega(f,g)$ is to be bandlimited. The conditions for perfect-reconstruction are very stringent on the choices of system functions $\Phi(f,g)$ and $\Omega(f,g)$. In other types of application it may be feasible to oversample the signals and apply advanced digital signal processing, but increasing the sampling rate of imaging systems tends to be prohibitively expensive. For that reason some of the filtering is done using optical elements. For example, in Figure 2.1 we show that normally have optical anti-aliasing filters covering the light sensors [23]. Since the choice of optical filters is quite limited—they cannot produce impulse response functions with negative values—some aliasing is inevitable.

Since images are commonly meant to be seen by people, it is also important to take into account at least some psychovisual factors, since some reconstruction approximation problems are visually much more important than others. Appendix C contains a short discussion on how the non-uniform response of the HVS affects the subjective response. Imaging systems need to be designed taking into account the fact that some differences are much easier to visualize. For instance, ideal filters eliminate all aliasing, but create "ringing" artifacts that significantly degrade the image quality [4].

Considering these facts, it should be clear that it makes little sense to try to enforce, in the design of imaging systems, the exact reconstruction conditions, or the

[1] We are not considering modulated signals, like those used in communications, and other cases that do not apply to images.

complete elimination of aliasing. On the other hand, it is important to use realistic models, which take into account the type of approximations resulting from common technical solutions. In the next section we discuss models for light measurement or reproduction profiles in each pixel.

2.3 Pixel Light Intensity Profile

The simplest way to model the pixel light intensity profile (PLIP) in a digital camera or projector is to assume that the pixels are square, each side has length ℓ, and with constant light response, or constant light intensity, in its whole surface. Formally, we can first define the box function

$$b_\ell(x) \doteq \begin{cases} 1/\ell, & 0 \le x \le \ell, \\ 0, & \text{otherwise}, \end{cases} \tag{2.13}$$

and then use it to define $\omega(x, y)$ or $\phi(x, y)$. For instance, we can model cameras assuming that $\omega(x, y) = b_\ell(x)b_\ell(y)$, and model projectors or displays assuming that $\phi(x, y) = b_\ell(x)b_\ell(y)$.

This type of function is very useful as a first approximation, since it allows very simple computations, and still yield a good intuition of the systems characteristics. However, it presents several problems that are actually avoided in practice.

If such type of sensor is used in cameras, the flat response results in very weak rejection of the image components with spatial frequencies beyond $1/(2\delta)$, and the resulting aliasing—caused by the sum of high-frequency terms in (2.10)—can produce strange artifacts in regions with high-frequency repetitive patterns (Moiré artifacts).

For projectors, the problem with $b_\ell(x)$ is that in practice we have $\ell < \delta$, i.e., the interval between pixels is larger than the actual pixel size, and there is a dark band between pixels.[2] These dark lines correspond to spurious high-frequency components that produce a strong visual response, and can be quite annoying.

In both cases the solution most commonly used is to place optical anti-aliasing filters—which are basically lowpass filters—in front of the sensors (see Figure 2.1) or in front of the light valves. A mathematically convenient way to take the contribution of these filters into account is to model the pixel response as a convolution of the box function with Gaussian filters. The resulting response is defined by

$$b_{\ell,\sigma}(x) \doteq \frac{1}{\ell}\left[Q\Big(\frac{x}{\sigma\ell}\Big) - Q\Big(\frac{x-\ell}{\sigma\ell}\Big)\right], \quad \sigma > 0, \tag{2.14}$$

where

$$Q(x) \doteq \frac{1}{\sqrt{2\pi}} \int_{-\infty}^{x} e^{-t^2/2}\, dt. \tag{2.15}$$

[2]The ratio between light and dark areas is called *aperture ratio*.

Some examples of this function, for different values of σ, are shown in Figure 2.2.

Since we have

$$\lim_{\sigma \to 0} b_{\ell,\sigma}(x) = b_\ell(x), \tag{2.16}$$

we define $b_{\ell,0}(x) \doteq b_\ell(x)$.

The advantage of this type of function is that, because of its smoothness, its spectrum decays quite rapidly. The Fourier transform of $b_{\ell,\sigma}(x)$ is

$$B_{\ell,\sigma}(f) = \begin{cases} 1, & f = 0, \\ \dfrac{\sin(\pi \ell f)}{\pi \ell f}\, e^{-\pi \ell f (j + 2\pi \ell f \sigma^2)}, & f \neq 0. \end{cases} \tag{2.17}$$

Figure 2.3 shows the spectra corresponding to the functions shown in Figure 2.2.

Figure 2.4 shows how individual pixels with PLIP functions $\phi(x, y) = b_{\ell,\sigma}(x) b_{\ell,\sigma}(y)$ actually look, for different values of parameter σ. We can see the advantage of using Gaussian filters in our models: in two dimensions they have spherical symmetry, as expected with optical filters. Also note that even though the individual pixels look blurred, we can see in Figure 2.3 that even for relatively large values of σ the attenuation occurs mostly on frequencies that correspond to artifacts created by the discontinuities of $b_\ell(x)$. This can be seen in Figure 2.5, which shows the same pixel profile functions applied to a real image.

Note that this model is a better match to some technologies than others. For instance, it is a reasonably good approximation to projectors that use liquid-crystal or micro-mirrors as light valves, and color-filter wheels for generating color projections.

2.4 Image Bandwidth and Display Quality

It is frequently difficult to evaluate the exact characteristics of display systems [23, 37], and make fair comparisons. Commonly, the comparison is between the same type of devices, and it may be possible to guess differences in image quality using only one of the device's specifications, like nominal resolution. In this section we present some examples that show that when we have different types of devices the comparisons are significantly more complex.

In our mathematical model of image reconstruction (2.11), all the facts that we discuss here are related to the choice of the pixel light intensity profile (PLIP), $\phi(x, y)$. In Section 2.3 we analyzed one type of function that is a particularly good model of what we find in current projectors. The general problem of optimal image reconstruction has been extensively studied (see, for instance, [4, 6]). While there are many factors, depending on viewing conditions, one universal agreement is that using a flat PLIP (i.e., $\phi(x, y) = b_\ell(x) b_\ell(y)$) is far from optimal.

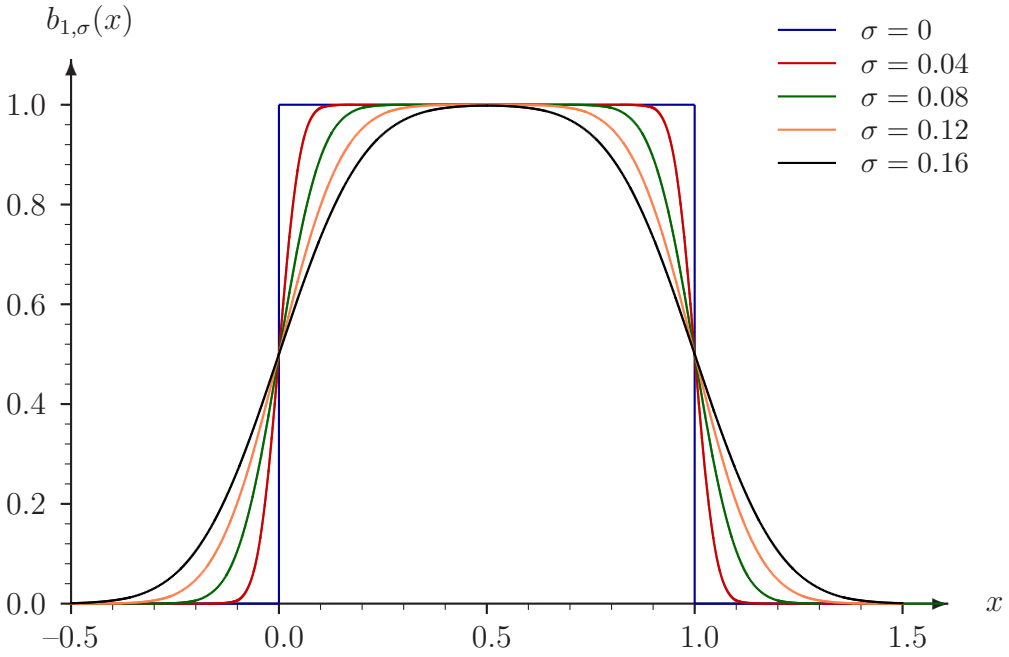

Figure 2.2: Shape of the one-dimensional function corresponding to the convolution of a box function ($\sigma = 0$) with Gaussian filters, varying according to parameter σ.

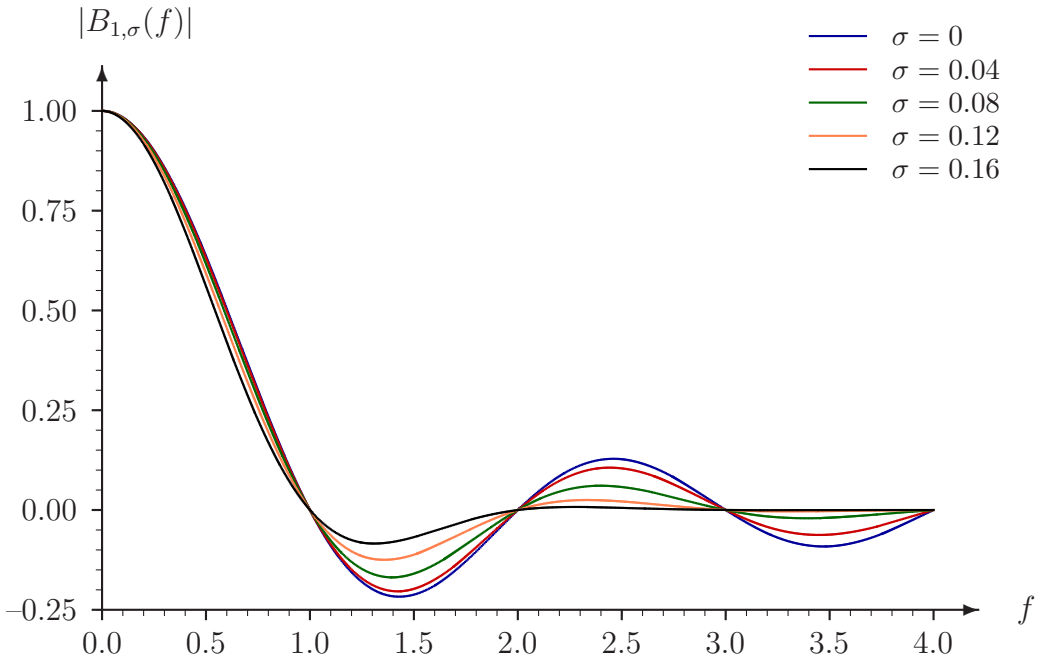

Figure 2.3: Spectrum of the one-dimensional function corresponding to the convolution of a box function ($\sigma = 0$) with Gaussian filters, varying according to parameter σ.

$\sigma = 0$ $\sigma = 0.04$ $\sigma = 0.08$ $\sigma = 0.12$ $\sigma = 0.16$ $\sigma = 0.2$

Figure 2.4: Visual aspect of individual pixels modeled with function $\phi(x, y) = b_{\ell,\sigma}(x)b_{\ell,\sigma}(y)$, with the indicated values of the Gaussian function parameters σ.

This follows easily from (2.12), if $\Phi(f, g)$ is not a good lowpass filter, we can observe "pixelated" images, with the artifacts corresponding to harmonic frequency components in (2.12).

There are many options for recovering images that are functions of continuous variables ($p(x, y)$) from sets of samples ($r[m, n]$). However, for our purposes we can use the fact that very good reproductions (i.e., that are visually pleasant) can be easily obtained using bi-cubic interpolation. Mitchell and Netravali [6] propose a family of functions that are suited for bi-cubic image interpolation, which are defined by two parameters (B, C), and have the form

$$c_{B,C,\ell}(x) = \frac{1}{6\ell} \begin{cases} 6 - 2B + (12B + 6C - 18)|x|^2 + & |x| < \ell \\ \quad (12 - 9B - 6C)|x|^3, & \\ 8B + 24C - (12B + 48C)|x| + & \ell \le |x| < 2\ell \\ \quad (6B + 30C)|x|^2 - (B + 6C)|x|^3, & \\ 0, & |x| \ge 2\ell \end{cases} \tag{2.18}$$

Figure 2.6 shows some examples of these functions for a few selected pairs of parameters, while Figure 2.7 shows their spectra. The main problem is the selection of a filter that achieves a good compromise between the conflicting objectives of minimizing blurring and avoiding visible ringing artifacts.

Figure 2.8 shows the contrast between two images which are generated from the same original data. The first is reproduced using pixels with flat light intensity ($b_\ell(x)$), and the second with the following pixel profile optimized for visual appearance: the bi-cubic interpolation of (2.18) with $B = C = 1/3$. Figure 2.9 shows the same type of comparison using original images with twice the resolution. For comparison, Figure 2.10 shows a 512×512 version of the image.

While the visual quality of Figure 2.8(b) is clearly superior to Figure 2.8(a), the visual quality of Figure 2.9(a) is somewhat better than that of Figure 2.8(b). With the current technologies for digital displays and projectors it is less expensive to manufacture devices with flat pixel light intensity, but more resolution, than to try to obtain good interpolation.

Figure 2.5: Examples of images generated with a projector with 90% aperture ratio, and different anti-aliasing Gaussian filters. The filter parameters are, from left to right, and top to bottom, $\sigma = 0$, 0.04, 0.08, 0.12, 0.16, and 0.2.

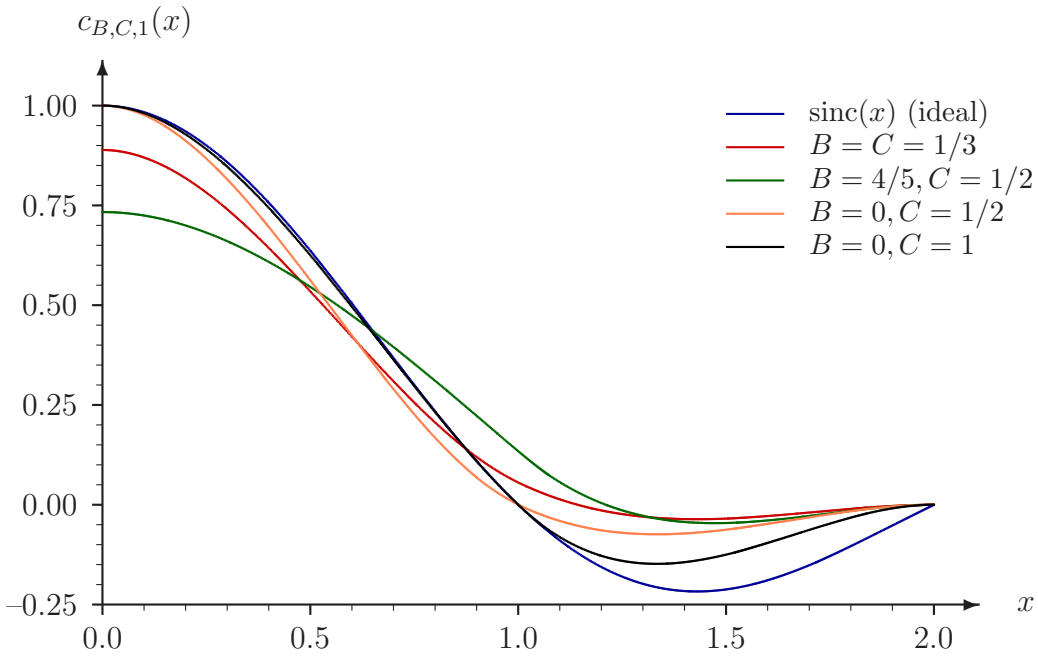

Figure 2.6: Examples of the impulse response of filters that can be used for bi-cubic image interpolation.

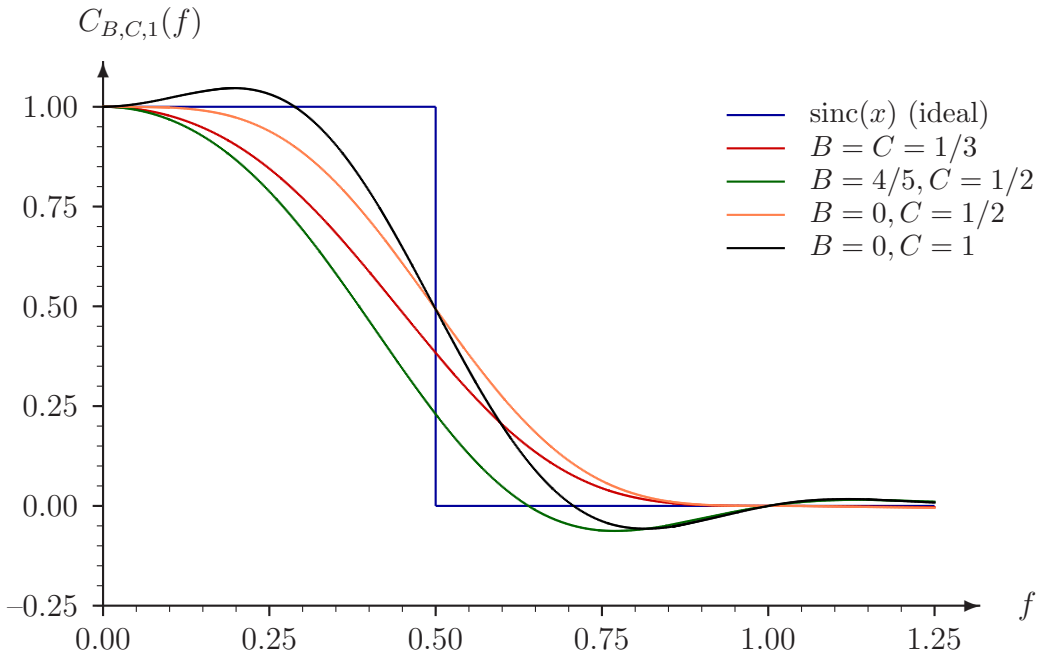

Figure 2.7: Examples of the frequency response of filters that can be used for bi-cubic image interpolation.

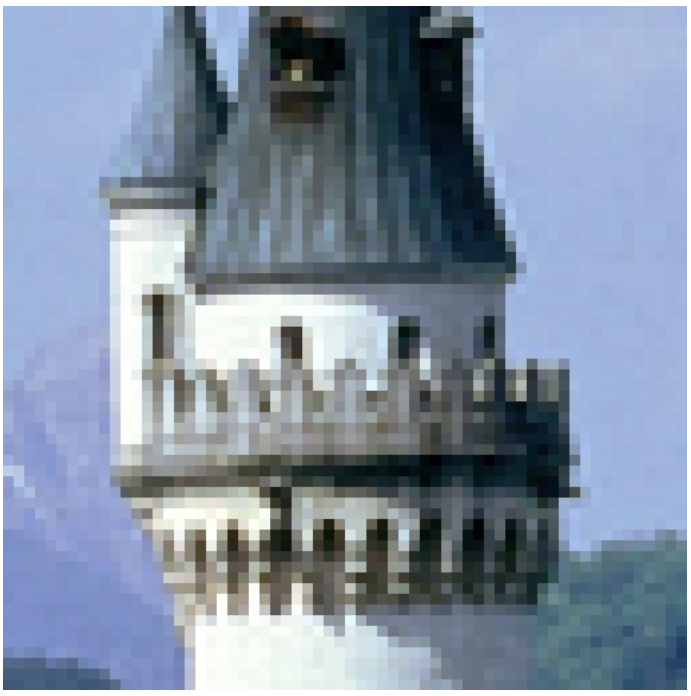

(a) 64×64 image, discrete display.

(b) 64×64 image, interpolated for continuous display.

Figure 2.8: Comparison of visual quality depending on display type: 64×64 image.

(a) 128×128 image, discrete display.

(b) 128×128 image, interpolated for continuous display.

Figure 2.9: Comparison of visual quality depending on display type: double bandwidth.

Figure 2.10: Original 512×512 image.

It is important to note that the optical filtering solution described in Section 2.3 is meant only to improve the visual quality by removing the artificial high frequency components. Comparing the frequency responses in Figures 2.3 and 2.7 we can see that optimal reconstruction requires stronger attenuation of the high frequencies. Using larger values of σ in the optical anti-aliasing filter produces excessive blurring, and any attempts to compensate this with digital signal processing creates problems with projector underflow and overflow, similar to those found with image superimposition.

When we analyze the superimposition of several projected images, we have two important factors to consider. First, it is an application that requires advanced signal processing, including the careful consideration of overflow and underflow, before sending the images to each projects. Second, the superimposed images do not have the same pixel light intensity profile as those in each subframe.

When considering subframes of the same type of PLIP, it is not necessary to consider how it changes the visual quality. With image superimposition we are changing the PLIP, and thus need to take this aspect back into consideration. In other words, just like Figure 2.8(b) has higher visual quality than Figure 2.8(a), even though it is created from an image with same resolution, an image obtained from superimposition may result in a PLIP that yields better visual quality.

Chapter 3

Linear Image Superimposition

In this chapter we present general mathematical models for the superimposition of projected images. We start from a very general formulation, which can only be solved numerically using the methods presented in Chapter 7. Next, we define models that are increasingly more constrained, but sufficiently general to include all the situations we want to study, and that can be in part analyzed in the frequency domain using standard signal processing techniques.

3.1 Models for Image Superimposition

3.1.1 General model

In our most general model for image superimposition we assume that we have a set of P subframes, and the signal corresponding to each subframe $p = 0, 1, \ldots, P-1$, setting the light intensity for each each pixel (m, n), is defined by the two-dimensional *driver array* $c_p[m, n]$. The light intensity of each projected image is modeled as a linear combination of the functions $\phi_{p,m,n}(x, y)$, which represent the distribution of light corresponding to pixel (m, n) of subframe p.

We can choose the pixel values $c_p[m, n]$ in any manner, as long as each value is within certain bounds (commonly normalized to [0,1]), to create the *subframes*

$$\psi_p^{(g)}(x, y) \doteq \sum_{m=-\infty}^{\infty} \sum_{n=-\infty}^{\infty} c_p[m, n]\phi_{p,m,n}(x, y), \quad p = 0, 1, \ldots, P-1. \tag{3.1}$$

Since light intensify combines in a linear manner, we define the two-dimensional *superimposition function* $\psi(x, y)$ that represent the linear combination of the P pro-

jected subframes, as

$$\psi^{(g)}(x,y) \doteq \sum_{p=0}^{P-1} \psi_p^{(g)}(x,y) = \sum_{p=0}^{P-1} \sum_{m=-\infty}^{\infty} \sum_{n=-\infty}^{\infty} c_p[m,n]\phi_{p,m,n}(x,y), \tag{3.2}$$

where product $c_p[m,n]\phi_{p,m,n}(x,y)$ represents the modulated light of the projection element (pixel) originated from subframe p, at position (m,n).

Again it is important to observe that the linear model is valid only when $c_p[m,n]$ is defined in terms of light intensity, with proper gamma correction (cf. Appendix B). In addition, since all the main results in this first analysis are independent of boundary effects, we still assume that $\psi(x,y)$ and $\phi_{p,m,n}(x,y)$ are defined for the whole plane, i.e., we have $x, y \in (-\infty, \infty)$.

This first model is general enough to accommodate many types of image superimposition, including optical distortions and different projector-screen orientations, but too general for detailed theoretical analysis. Note that all the information about the type and configuration of subframes is in the definition of the functions $\phi_{p,m,n}(x,y)$.

The main technical problem studied in this document is the optimal determination of the pixel values $c_p[m,n]$. The methods described in Chapter 7 are capable of numerically solving this general problem, when we consider finite images. However, they do not provide a better understanding of the problem, and properties of the solutions. In the next sections we show that by progressively limiting the type of subframes and the configuration of projected images we obtain linear models that are easier to be analyzed with standard signal processing tools.

Even though we are always referring to images, the analysis of signals in two dimensions is another factor that can make even simple results seem less intuitive. Many of the important properties of image superimposition can be more easily understood by considering the one-dimensional version of the problem, which can be formulated as

$$\psi^{(g)}(x) \doteq \sum_{p=0}^{P-1} \sum_{m=-\infty}^{\infty} c_p[m]\phi_{p,m}(x). \tag{3.3}$$

This type of problem actually occurs in imaging applications if all the subframes are aligned to increase resolution along only one direction. Since we are interested only in the response in that direction, we can measure light intensity along a line to obtain the function $\psi^{(g)}(x)$, as shown in the example of Figure 3.1.[1] Another practical case is explained in Section 3.1.4.

[1]Note that the pixels of each subframe are shown at different horizontal lines at the top of the figure for easier visualization, but only their superimposition is of interest.

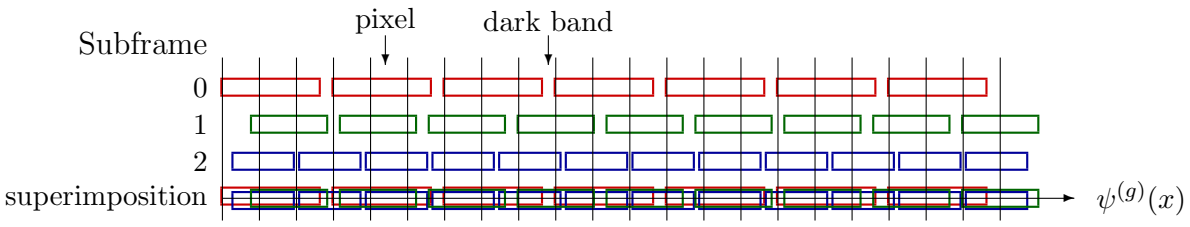

Figure 3.1: Example of how the superimposition of projected lines of pixels can be measured along a line to create the one-dimensional signal function $\psi^{(g)}(x)$.

3.1.2 Standard configuration

The first set of constraints to be added to our general model is:

(a) All pixels corresponding to a subframe p have the same shape (PLIP), defined by $\phi_p(x, y)$, $p = 0, 1, \ldots, P-1$;

(b) All the pixels are arranged in lattices, defined by vectors $(u_p^{(x)}, u_p^{(y)})$ and $(v_p^{(x)}, v_p^{(y)})$, and offset $(\mu_p^{(x)}, \mu_p^{(y)})$.

In this case we have, for $p = 0, 1, \ldots, P-1$, and all $m, n \in \mathbb{Z}$,

$$\phi_{p,m,n}(x, y) = \phi_p\big(x - mu_p^{(x)} - nv_p^{(x)} - \mu_p^{(x)}, y - mu_p^{(y)} - nv_p^{(y)} - \mu_p^{(y)}\big)\,, \tag{3.4}$$

and we can model the superimposition of images as

$$\psi^{(l)}(x, y) \;\doteq\; \sum_{p=0}^{P-1} \sum_{m=-\infty}^{\infty} \sum_{n=-\infty}^{\infty} c_p[m, n]\, \phi_p\big(x - mu_p^{(x)} - nv_p^{(x)} - \mu_p^{(x)}\,, \; y - mu_p^{(y)} - nv_p^{(y)} - \mu_p^{(y)}\big) \tag{3.5}$$

With this periodic repetition of pixels we can start analyzing the superimposition in the frequency domain, and compute the two-dimensional Fourier transform of $\psi^{(l)}(x, y)$ as

$$\Psi^{(l)}(f, g) = \sum_{p=0}^{P-1} \Phi_p(f, g)\, e^{-j2\pi[f\mu_p^{(x)} + g\mu_p^{(y)}]}\, C_p\Big(e^{j2\pi[fu_p^{(x)} + gu_p^{(y)}]}, e^{j2\pi[fv_p^{(x)} + gv_p^{(y)}]}\Big)\,, \tag{3.6}$$

where $\Phi_p(f, g)$ and $C_p(e^{j2\pi f}, e^{j2\pi g})$ are the Fourier transforms of $\phi_p(x, y)$ and $c_p[m, n]$, respectively.

In practice, we cannot expect to see the assumptions above satisfied exactly, since we always have some deformations in the images, caused by imperfections in the lenses

and other optical components. However, as long as we have some reasonable level of consistency in sufficiently large regions (e.g., at least 20×20 pixels), then we can use this model—and its frequency domain analysis—to get a very good understanding of the superimposition system's behavior.

One extra assumption is required mostly for mathematical consistency. We need to assume that the two-dimensional arrays $c_p[m, n]$ have a finite number of nonzero elements (finite support), so that the signal energy is finite

$$\int_{-\infty}^{\infty} \int_{-\infty}^{\infty} [\psi^{(g)}(x, y)]^2 \, \mathrm{d}x \, \mathrm{d}y < \infty, \tag{3.7}$$

and the Fourier transforms are well-defined.[2]

The one-dimensional version of this model is defined by

$$\psi^{(l)}(x) = \sum_{p=0}^{P-1} \sum_{m=-\infty}^{\infty} c_p[m] \, \phi_p(x - mu_p - \mu_p), \tag{3.8}$$

$$\Psi^{(l)}(f) = \sum_{p=0}^{P-1} \Phi_p(f) \, e^{-j2\pi f \mu_p} \, C_p(e^{j2\pi f u_p}). \tag{3.9}$$

3.1.3 Same type of equally spaced subframes

The next case to be considered is when all conditions of Section 3.1.2 are satisfied, and we also require that

(a) All subframes are of the same type, and all images are scaled in the same manner, which means that for $p = 0, 1, \ldots, P-1$ we have $\phi_p(x, y) = \phi(x, y)$, $(u_p^{(x)}, u_p^{(y)}) = (u^{(x)}, u^{(y)})$, and $(v_p^{(x)}, v_p^{(y)}) = (v^{(x)}, v^{(y)})$;

(b) There are $P = MN$ equally-spaces projected images, which are offset from each other according to

$$(\mu_{k+Ml}^{(x)}, \mu_{k+Ml}^{(y)}) = (k\delta^{(x)} + l\epsilon^{(x)}, k\delta^{(y)} + l\epsilon^{(y)}), \qquad \begin{array}{l} k = 0, 1, \ldots, M-1, \\ l = 0, 1, \ldots, N-1. \end{array}$$

When the subframes are not only equally spaced, but also in a configuration that subdivides exactly the cells of the lattice created by the pixels in each subframe, we have the following important result.

[2] In this document we try to avoid using Dirac's delta function.

Theorem 3.1.1 *If we have $P = MN$ equally-spaced images from identical subframes satisfying*

$$\begin{aligned}(\delta^{(x)}, \delta^{(y)}) &= (u^{(x)}/M, u^{(y)}/M), \\ (\epsilon^{(x)}, \epsilon^{(y)}) &= (v^{(x)}/N, v^{(y)}/N).\end{aligned} \tag{3.10}$$

then the superimposed image can be represented as a linear combination modulated by a single two-dimensional array $c[m,n]$, in the form

$$\psi^{(r)}(x,y) = \sum_{m=-\infty}^{\infty} \sum_{n=-\infty}^{\infty} c[m,n] \phi\big(x - m\delta^{(x)} - n\epsilon^{(x)}, y - m\delta^{(y)} - n\epsilon^{(y)}\big)\,. \tag{3.11}$$

where $c[m,n]$ has the interleaved values of the pixel values in the P subframes, according to

$$\begin{aligned} c[mM + k, nN + l] = c_{k+Ml}[m,n], \quad & k = 0, 1, \ldots, M-1, \\ & l = 0, 1, \ldots, N-1, \\ & \forall m, n \in \mathbb{Z}. \end{aligned} \tag{3.12}$$

In addition, this use of a single set of pixel values $c[m,n]$ also results in a simpler form for the Fourier transform. In this case we have

$$\Psi^{(r)}(f,g) = \Phi(f,g)\, C\Big(e^{j2\pi[f\delta^{(x)} + g\delta^{(y)}]}, e^{j2\pi[f\epsilon^{(x)} + g\epsilon^{(y)}]}\Big)\,, \tag{3.13}$$

where $\Phi(f,g)$ and $C(e^{j2\pi f}, e^{j2\pi g})$ are the Fourier transforms of $\phi(x,y)$ and $c[m,n]$.

Proof: Using assumptions (a) and (b), and (3.10) we obtain the following special case of (3.4)

$$\begin{aligned}\phi_{k+Ml,m,n}(x,y) &= \phi\big(x - (mM+k)\delta^{(x)} - (nN+l)\epsilon^{(x)}, \\ &\qquad y - (mM+k)\delta^{(y)} - (nN+l)\epsilon^{(y)}\big)\,,\end{aligned} \tag{3.14}$$

and the equivalent of (3.5) is

$$\begin{aligned}\psi^{(r)}(x,y) &= \sum_{k=0}^{M-1} \sum_{l=0}^{N-1} \sum_{m=-\infty}^{\infty} \sum_{n=-\infty}^{\infty} c_{k+Ml}[m,n] \\ &\qquad \phi\big(x - (mM+k)\delta^{(x)} - (nN+l)\epsilon^{(x)}, \\ &\qquad\quad y - (mM+k)\delta^{(y)} - (nN+l)\epsilon^{(y)}\big)\,.\end{aligned} \tag{3.15}$$

The frequency-domain results follow directly from the computation of the Fourier transforms, but can also be derived from the substitution in (3.6), which yields

$$\begin{aligned}\Psi^{(r)}(f,g) &= \Phi(f,g) \sum_{k=0}^{M-1} \sum_{l=0}^{N-1} e^{-j2\pi[f(k\delta^{(x)} + l\epsilon^{(x)}) + g(k\delta^{(y)} + l\epsilon^{(y)})]} \\ &\qquad C_p\Big(e^{j2\pi[fM\delta^{(x)} + gM\delta^{(y)}]}, e^{j2\pi[fN\epsilon^{(x)} + gN\epsilon^{(y)}]}\Big)\,.\end{aligned} \tag{3.16}$$

Q.E.D.

It is important to note that, because we interleaved the P subframe inputs, $c_p[m,n]$, into a single function, $c[m,n]$, the actual number of subframes and their configuration (P,M,N) does not appear in the mathematical model (3.11). Since these factors are quite important in practice, this may be seem as a practical disadvantage, and that maybe we should avoid using this formulation. In reality, it is a significantly more powerful tool for analysing the cases of greatest interest to us, in which images are superimposed by carefully positioning the subframes in order to obtain higher resolution and better image quality.

The analysis of how the particular arrangement of subframes can be irrelevant for this mathematical model, and how it can be considered implicitly, is better done using the one-dimensional version of the model. First, let us define the equivalent version of Theorem 3.1.1.

Corollary 3.1.2 *In the one-dimensional case of superimposition, if we have P equally-spaced images from identical subframes satisfying*

$$\begin{aligned} \delta &= u/P, \\ \mu_p &= p\delta, \quad p = 0, 1, \ldots, P-1, \end{aligned} \tag{3.17}$$

then the superimposed image can be represented as a linear combination modulated by a single array $c[m]$, in the form

$$\psi^{(r)}(x) = \sum_{m=-\infty}^{\infty} c[m]\phi(x - m\delta), \tag{3.18}$$

where $c[m]$ has the interleaved values of the pixel values in the P subframes, according to

$$c[mP + p] = c_p[m], \quad m \in \mathbb{Z}, \quad p = 0, 1, \ldots, P-1, \tag{3.19}$$

and the equivalent result in the frequency domain is

$$\Psi^{(r)}(f) = \Phi(f)\, C(e^{j2\pi f\delta}), \tag{3.20}$$

where $\Phi(f)$ and $C(e^{j2\pi f})$ are the Fourier transforms of $\phi(x)$ and $c[m]$.

Proof: The substitution of conditions (3.17) into the formula (3.8) with explicit use of P yields

$$\begin{aligned} \psi^{(r)}(x) &= \sum_{p=0}^{P-1} \sum_{m=-\infty}^{\infty} c_p[m]\phi(x - mu - \mu_p), \\ &= \sum_{p=0}^{P-1} \sum_{m=-\infty}^{\infty} c_p[m]\phi(x - (mP + p)\delta). \end{aligned} \tag{3.21}$$

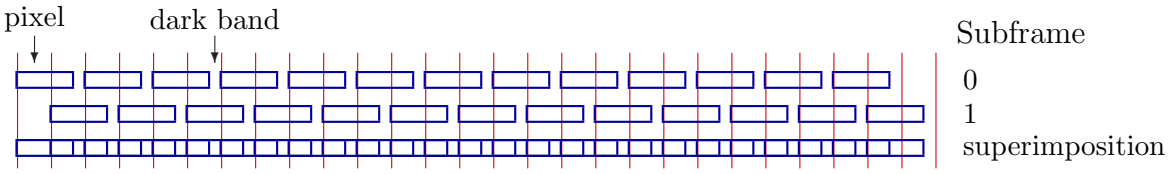

(a) Two subframes, $\ell = 1.8$

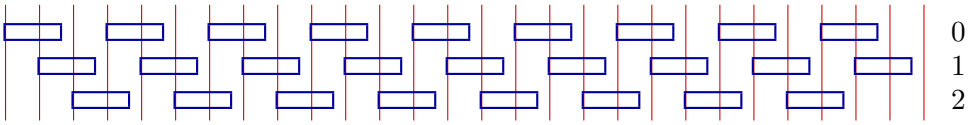

(b) Three subframes, $\ell = 1.8$

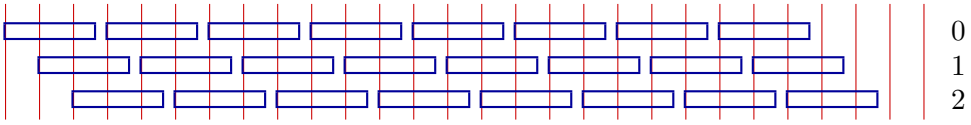

(c) Three subframes, $\ell = 2.7$

Figure 3.2: Examples of superposition with different number of subframes. Cases (a) and (b) have the same mathematical model.

The frequency-domain result follows from direct application of the Fourier transform. It is interesting to note that directly from (3.9) we obtain

$$\Psi^{(r)}(f) = \Phi(f) \sum_{p=0}^{P-1} e^{-j2\pi fp\delta}\, C_p(e^{j2\pi fP\delta}). \tag{3.22}$$

$\mathcal{Q}.\mathcal{E}.\mathcal{D}.$

Figures 3.2 and 3.3 show examples of how the model takes different subframe configurations into account. In the diagram of Figure 3.2(a) we assume that each projected image is shifted by one unit ($\delta = 1$), and we use two subframes with spacing between their pixels $u = 2$. Again, in the top part of figure the pixels of each subframe are shown at different horizontal lines, and the last line shows the superposition. The thin vertical lines indicate the pixel alignment.

In this example we assume that, due to technological constraints, in each pixel interval there is projected light only in a subinterval of length $\ell = 1.8$, and that between the pixels there is a dark interval of length 0.2 (90% aperture ratio, $\phi(x) = b_{1.8}(x)$). This is also shown in Figure 3.3(a), where we can see the superposition of the two subframes.

Figure 3.2(b) shows another case, of three subframes with smaller aperture ratio, in which the spacing between pixels is $u = 3$, and the length of the parts with

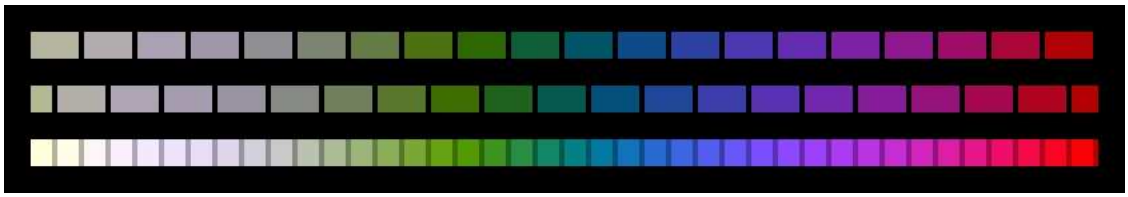

(a) Two subframes, $\ell = 1.8$.

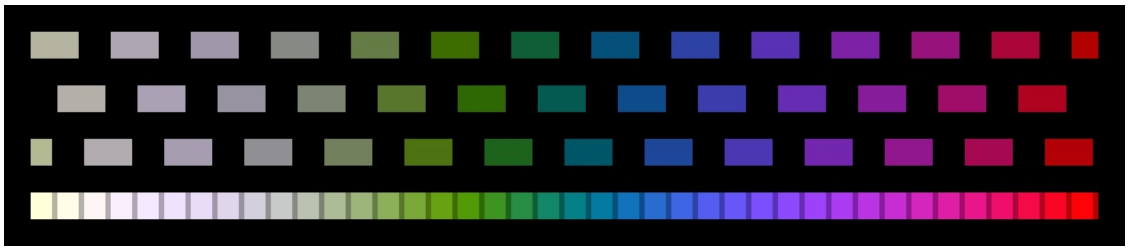

(a) Three subframes, $\ell = 1.8$.

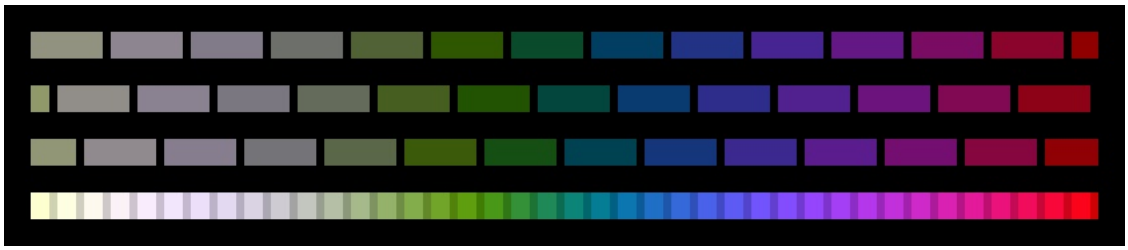

(c) Three subframes, $\ell = 2.7$.

Figure 3.3: Examples of color pixels corresponding to the superposition cases shown in Figure 3.2: in each image the first lines show the pixel colors, and the last line shows the superimposed pattern.

and without light are respectively 1.8 and 1.2 (60% aperture ratio). Despite these differences, in the analysis of the combination of projected images this case is identical to that shown Figure 3.2(a), because it is composed of the same set of projected pixels that can be independently controlled. For instance, the superposition in Figures 3.3(a) and 3.3(b) are identical. In fact, from a mathematical perspective, we could even assume that each pixel comes from a different subframe.

The minimum number of subframes, on the other hand, is determined by the shift δ, and the length of the active part of the pixel. Figure 3.2(c) shows that if we keep $\delta = 1$ but increase the length to $\ell = 2.7$, then we need at least three subframes. Note that these subframes can be the same that are used in Figure 3.2(a), but using different projection magnification ("zooming"), since in both cases we have a 90% aperture ratio. Another difference is that in Figure 3.2(a) the projected images are positioned to double the resolution and brightness, while in Figure 3.2(c) they are arranged for a threefold increase.

3.1.4 Rectangular lattices and separable pixel profile

The next case to be considered is when we add to the conditions of Sections 3.1.2 and 3.1.3 the following conditions

(a) The lattices corresponding to pixels and projected images are defined in the x and y directions, i.e., $\epsilon^{(x)} = \delta^{(y)} = 0$ and $\delta^{(x)} = \delta$, $\epsilon^{(y)} = \epsilon$;

(b) The pixel light intensity function is separable in the x and y directions, i.e., $\phi(x, y) = \phi^{(x)}(x)\phi^{(y)}(y)$.

The new model is considerably simpler:

$$\psi^{(s)}(x, y) \doteq \sum_{m=-\infty}^{\infty} \sum_{n=-\infty}^{\infty} c[m, n]\phi^{(x)}(x - m\delta)\phi^{(y)}(y - n\epsilon), \tag{3.23}$$

and produces a Fourier transform in the following form.

$$\Psi^{(s)}(f, g) = \Phi^{(x)}(f)\, \Phi^{(y)}(g)\, C(e^{j2\pi f\delta}, e^{j2\pi g\epsilon}), \tag{3.24}$$

This model is much less general than the first. However, it is important because it corresponds to the most common type of projection systems, with square pixels. In fact, as we have shown in Section 2.3, even with optical anti-aliasing filters with circular symmetry, we can approximate real projected pixels very well using a separable function like $\phi(x, y) = b_{\ell,\sigma}(x)\, b_{\ell,\sigma}(y)$, where $b_{\ell,\sigma}(\cdot)$ is defined by equation (2.14).

We can see from the equations above that in this case we can analyze the superimposition by studying the filtering operations in the horizontal and vertical directions

independently. The one-dimensional version of this model is identical to the model defined by (3.18). To simplify notation we define this as our standard model, using $\psi(x)$ instead of $\psi^{(r)}(x)$:

$$\psi(x) \doteq \sum_{m=-\infty}^{\infty} c[m]\phi(x - m\delta), \tag{3.25}$$

$$\Psi(f) = \Phi(f)\, C(e^{j2\pi f\delta}). \tag{3.26}$$

3.2 Image Evaluation

Before we tackle the problem of finding the set of optimal pixel values $c_p[m, n]$, we need to identify the criteria to be used for evaluating the quality of a solution. Different evaluation models create different formulations for the optimization of $c_p[m, n]$, and thus may yield optimal solutions with quite different characteristics.

3.2.1 Abstract Model

Ideally we would define the optimal solution, $c_p^*[m, n]$, as the particular $c_p[m, n]$ that minimizes some measure of distortion $D(p(x, y), \psi(x, y))$, where $p(x, y)$ is the original image, and $\psi(x, y)$ is the result of the image superimposition, according to one of the models presented in the last section. However, in practice we obviously can only have sampled pixel values $r[m, n]$ (equation (2.6) in Section 2.2).

We propose a criterion for evaluating the quality of the superimposed images which is simple and convenient, and also quite general and flexible. We use a model that assumes periodic sampling at the output of a linear filter, with impulse response $\zeta(x, y)$, to produce[3]

$$s[m, n] \doteq \int_{-\infty}^{\infty}\int_{-\infty}^{\infty} \psi(x, y)\zeta(m - x, n - y)\, \mathrm{d}x\, \mathrm{d}y, \quad m, n \in \mathbb{Z}. \tag{3.27}$$

The shape and position of function $\zeta(x)$ is defined by the way we want to evaluate the response of the system. We adopt the normalization

$$\int_{-\infty}^{\infty}\int_{-\infty}^{\infty} \zeta(x, y)\, \mathrm{d}x\, \mathrm{d}y = 1. \tag{3.28}$$

Note that (3.27) is similar to the image acquisition (2.6), and $s[m, n]$ can be interpreted as a set of "pixel values." Figure 3.4 shows a diagram that represents this interpretation. First, we assume that some algorithm is used to convert $r[m, n]$ into

[3]Without loss of generality, we use unitary sampling intervals here to simplify the notation.

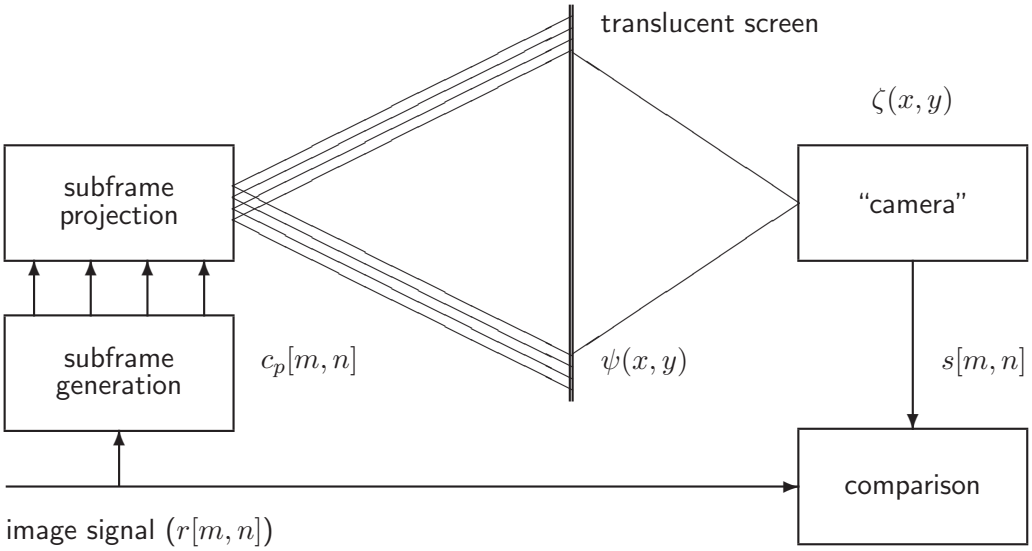

Figure 3.4: Idealized model for evaluation of the superimposed projections.

the subframes $c_p[m, n]$, $p = 0, 1, \ldots, P-1$, which are fed to the P different subframes. Next, we imagine an ideal system in which all the images are projected onto an ideal translucent screen, and an imaginary digital camera converts the continuous superimposed image $\psi(x, y)$ back to discrete samples $s[m, n]$, which can be compared with the original for measuring the quality of the solution $c_p[m, n]$. (Figure 3.5 shows the equivalent mathematical model. A frequency-domain analysis of that dynamic system is done in the next section.)

Note that the stage for subframe generation is an integral part of the system, i.e., the performance of the combined projection system cannot be evaluated without full knowledge of the process that generates the input data for each subframe. This process, in turn, cannot be optimized without knowledge of how the quality is to be measured.

A very important difference between the idealized system of Figure 3.4 and a system that uses real cameras is that, as we show below, the impulse response $\zeta(x, y)$ is defined only to be used in some computations. Thus, we have a great deal of freedom choosing the impulse response $\zeta(x, y)$, including functions with negative value, infinite support, etc. For instance, we can choose it to be an ideal two-dimensional lowpass filter, or some filter that approximates the response of the human visual system [22].

3.2.2 Sampled values and their Fourier transforms

In this section we show how the substitution of the different formulations of $\phi(x, y)$, derived in Section 3.1, into (3.27) results in models where all functions are of discrete

variables. But first, for a more detailed analysis in the frequency domain, we define the convolution signal that is sampled as

$$s_c(x,y) \doteq (\psi * \zeta)(x,y) = \int_{-\infty}^{\infty}\int_{-\infty}^{\infty} \psi(w,z)\zeta(x-w,y-z)\,\mathrm{d}w\,\mathrm{d}z. \tag{3.29}$$

which has Fourier transform

$$S_c(f,g) = \Psi(f,g)\,Z(f,g), \tag{3.30}$$

where $Z(f,g)$ is the two-dimensional Fourier transform of $\zeta(x,y)$.

Since we have unit sampling intervals, $s[m,n] = s_c(m,n)$ and

$$\begin{aligned} S(e^{j2\pi f}, e^{j2\pi g}) &= \sum_{k=-\infty}^{\infty}\sum_{l=-\infty}^{\infty} S_c(f-k,g-l) \\ &= \sum_{k=-\infty}^{\infty}\sum_{l=-\infty}^{\infty} \Psi(f-k,g-l)\,Z(f-k,g-l). \end{aligned} \tag{3.31}$$

Using the most general model, $\psi^{(g)}(x,y)$, in (3.29), we obtain

$$s_c^{(g)}(x,y) = \sum_{p=0}^{P-1}\sum_{m=-\infty}^{\infty}\sum_{n=-\infty}^{\infty} c_p[m,n]\lambda_{p,m,n}(x,y), \tag{3.32}$$

where

$$\lambda_{p,m,n}(x,y) = \int_{-\infty}^{\infty}\int_{-\infty}^{\infty} \phi_{p,m,n}(w,z)\zeta(x-w,y-z)\,\mathrm{d}w\,\mathrm{d}z. \tag{3.33}$$

Using this representation we can define the discrete-variable model as

$$s^{(g)}[m,n] = \sum_{p=0}^{P-1}\sum_{i=-\infty}^{\infty}\sum_{j=-\infty}^{\infty} c_p[i,j]t_p[m,n,i,j], \tag{3.34}$$

where $t_p[m,n,i,j] = \lambda_{p,i,j}(m,n)$.

The particular cases defined in Section 3.1 correspond to different ways to compute $t_p[m,n,i,j]$. For instance, using (3.4) yields

$$\lambda_{p,m,n}(x,y) = \lambda_p\big(x - mu_p^{(x)} - nv_p^{(x)} - \mu_p^{(x)}, y - mu_p^{(y)} - nv_p^{(y)} - \mu_p^{(y)}\big), \tag{3.35}$$

where

$$\lambda_p(x,y) = \int_{-\infty}^{\infty}\int_{-\infty}^{\infty} \phi_p(w,z)\zeta(x-w,y-z)\,\mathrm{d}w\,\mathrm{d}z. \tag{3.36}$$

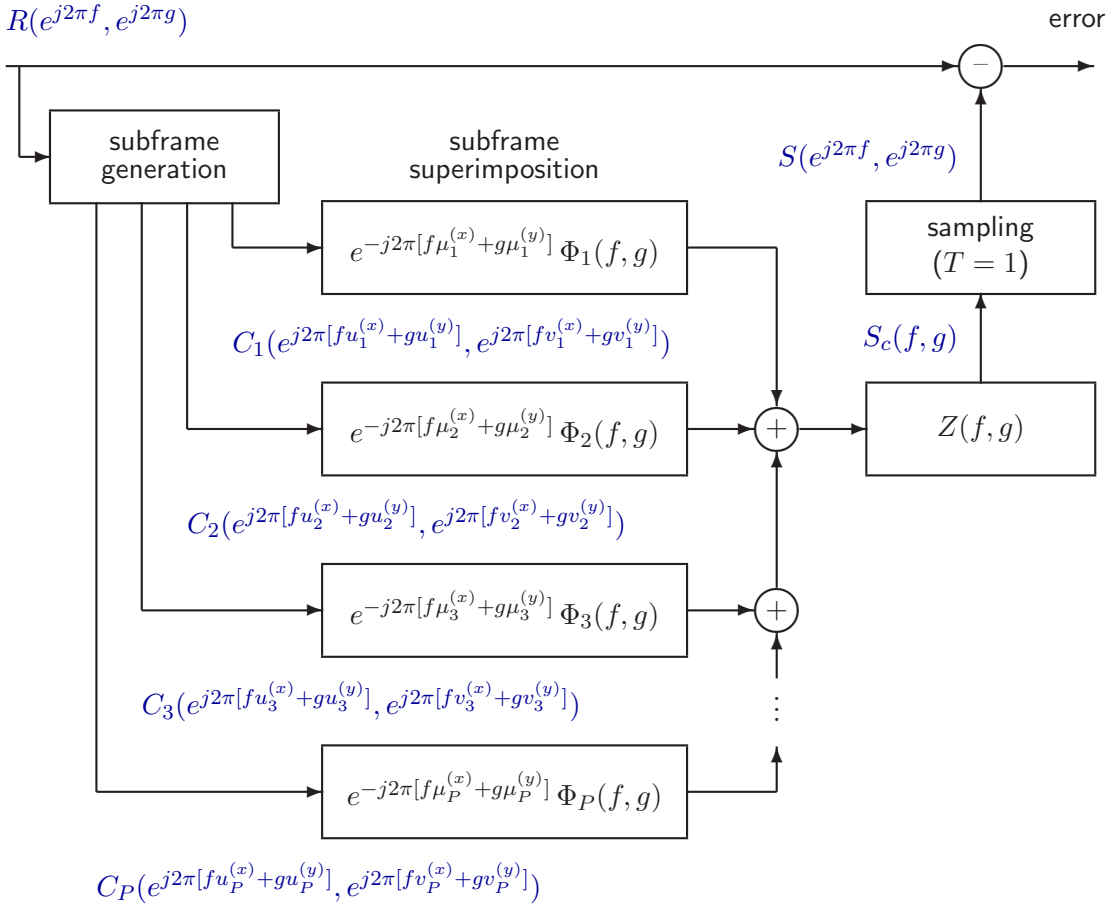

Figure 3.5: Model for evaluation of the superimposed subframes.

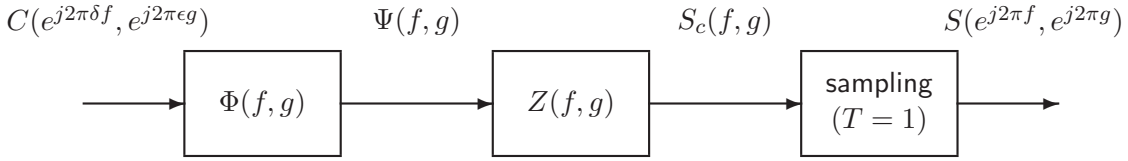

Figure 3.6: Complete system for image generation, projection, and sampling.

Figure 3.5 shows how the system of Figure 3.4 can be mathematically modeled, using the notation defined above.

The superimposition models that use interleaved driver data, like (3.11) yield a model in the form

$$s[m,n] = \sum_{i=-\infty}^{\infty} \sum_{j=-\infty}^{\infty} c[i,j]t[m,n,i,j], \tag{3.37}$$

where now

$$t[m,n,i,j] = \lambda\big(m - i\delta^{(x)} - j\epsilon^{(x)}, n - i\delta^{(y)} - j\epsilon^{(y)}\big)\,, \tag{3.38}$$

and

$$\lambda(x,y) = \int_{-\infty}^{\infty}\int_{-\infty}^{\infty} \phi(w,z)\zeta(x-w, y-z)\,\mathrm{d}w\,\mathrm{d}z. \tag{3.39}$$

We can observe that this is a linear system, but not necessarily separable or position-invariant.

The Fourier transform of this function is

$$\Lambda(f,g) = \Phi(f,g)\,Z(f,g). \tag{3.40}$$

We have a separable system when we can decompose

$$S_c(f,g) = S_c^{(x)}(f)\,S_c^{(y)}(g). \tag{3.41}$$

From (3.30), we conclude that $S_c(f,g)$ is separable when both $\Psi(f,g)$ and $Z(f,g)$ are separable.[4] The conditions for a superimposition model with separable function $\Psi^{(s)}(f,g)$ are presented in Section 3.1.4. Assuming $Z(f,g) = Z^{(x)}(f)Z^{(y)}(g)$ we have

$$\lambda(x,y) = \lambda^{(x)}(x)\,\lambda^{(x)}(y) \tag{3.42}$$

$$= \left[\int_{-\infty}^{\infty} \phi^{(x)}(w)\zeta^{(x)}(x-w)\,\mathrm{d}w\right]\left[\int_{-\infty}^{\infty} \phi^{(y)}(z)\zeta^{(y)}(y-z)\,\mathrm{d}z\right]. \tag{3.43}$$

[4]It is mathematically possible to have a separable $S_c(f,g)$ when $\Psi(f,g)$ and $Z(f,g)$ are not separable, but this is of little relevance to our problem.

Defining $t^{(x)}[m,i] = \lambda^{(x)}(m - i\delta)$ and $t^{(y)}[n,j] = \lambda^{(y)}(n - j\epsilon)$, we can see that under these conditions the discrete-variable model is also separable, since

$$s[m,n] = \sum_{i=-\infty}^{\infty} \sum_{j=-\infty}^{\infty} c[i,j] t^{(x)}[m,i] t^{(y)}[n,j]. \tag{3.44}$$

3.2.3 One-dimensional versions

In the common cases in which the superimposition system and the its sampling function are separable, equations like (3.44) are unnecessarily cumbersome. It is much more convenient to study one-dimensional versions of the models, which we present next.

The one-dimensional equivalent of (3.29) is

$$s[m] \doteq \int_{-\infty}^{\infty} \psi(x)\zeta(m - x)\,\mathrm{d}x, \quad m \in \mathbb{Z}. \tag{3.45}$$

and $\zeta(x)$ is a function that satisfies

$$\int_{-\infty}^{\infty} \zeta(x)\,\mathrm{d}x = 1. \tag{3.46}$$

Similarly to the two-dimensional cases analyzed in the last section, we obtain different formulations depending on the assumptions.

General model

$$\begin{aligned}
s_c^{(g)}(x) &= \sum_{p=0}^{P-1} \sum_{n=-\infty}^{\infty} c_p[n] \lambda_{p,n}(x), && (3.47)\\
\lambda_{p,n}(x) &= \int_{-\infty}^{\infty} \phi_{p,n}(w)\zeta(x - w)\,\mathrm{d}w, && (3.48)\\
s^{(g)}[m] &= \sum_{p=0}^{P-1} \sum_{n=-\infty}^{\infty} c_p[n] t_p^{(g)}[m,n], && (3.49)\\
t_p^{(g)}[m,n] &= \lambda_{p,n}(m). && (3.50)
\end{aligned}$$

Standard subframes

$$s_c^{(l)}(x) = \sum_{p=0}^{P-1} \sum_{n=-\infty}^{\infty} c_p[n] \lambda_p(x - n u_p - \mu_p), \tag{3.51}$$

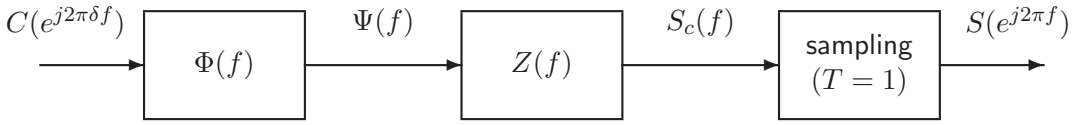

Figure 3.7: System for one-dimensional signal generation, filtering, and sampling.

$$\lambda_p(x) = \int_{-\infty}^{\infty} \phi_p(w)\zeta(x-w)\,\mathrm{d}w, \tag{3.52}$$

$$s^{(l)}[m] = \sum_{p=0}^{P-1} \sum_{n=-\infty}^{\infty} c_p[n] t_p^{(l)}[m,n], \tag{3.53}$$

$$t_p^{(l)}[m,n] = \lambda_p(m - nu_p). \tag{3.54}$$

Equally spaced identical subframes

$$s_c(x) = \sum_{n=-\infty}^{\infty} c_p[n]\lambda(x-n\delta), \tag{3.55}$$

$$\lambda(x) = \int_{-\infty}^{\infty} \phi(w)\zeta(x-w)\,\mathrm{d}w, \tag{3.56}$$

$$s[m] = \sum_{n=-\infty}^{\infty} c[n]t[m,n], \tag{3.57}$$

$$t[m,n] = \lambda(m-n\delta). \tag{3.58}$$

In this case it is also interesting to compute the Fourier transform

$$S_c(f) = C(e^{j2\pi\epsilon f})\Phi(f)Z(f), \tag{3.59}$$

$$\begin{aligned} S(e^{j2\pi f}) &= \sum_{k=-\infty}^{\infty} S_c(f+k) \\ &= \sum_{k=-\infty}^{\infty} C(e^{j2\pi\delta[f+k]})\Lambda(f+k), \end{aligned} \tag{3.60}$$

where

$$\Lambda(f) = \Phi(f)Z(f). \tag{3.61}$$

Figure 3.7 shows a diagram of the complete system.

3.3 Resolution Factors

In the image superimposition model defined in Section 3.1.3 we assume that the $P = MN$ projected images are equally spaced in order to obtain, in the combined image, higher resolution. This is defined in the separable model (3.23) by the parameters δ and ϵ, which set the space between the pixels from all subframes, in the horizontal and vertical directions.

Below we analyze how the choices of δ and ϵ affect the resolution of the superimposed image, and how particular cases affect the analysis of the linear dynamic systems. Note that these choices are relative to unit values, since the sampling (3.27) of the superimposed image is done with $\zeta(x, y)$ repeated in a square grid, with unitary period.

3.3.1 Critically Sampled Systems

In the diagram of Figure 3.4, we can compare the average number of pixel values $c_p[m, n]$ that are fed to the P subframes with the average number of sampled pixels $s[m, n]$, per unit area of the projected image. We say that a system is *critically sampled* when these two numbers are equal. This happens when in (3.38) we have $\delta^{(x)} = \epsilon^{(y)} = 1$ and $\delta^{(y)} = \epsilon^{(x)} = 0$, and thus

$$t[m, n, i, j] = \lambda(m - i, n - j). \tag{3.62}$$

where $\lambda(x, y)$ is defined by (3.39).

Therefore, if we define

$$h[m, n] \doteq \lambda(m, n). \tag{3.63}$$

then the model (3.37) becomes

$$s[m, n] = (c * h)[m, n] = \sum_{i=-\infty}^{\infty} \sum_{j=-\infty}^{\infty} c[i, j]h[m - i, n - j], \tag{3.64}$$

and in the frequency domain we have

$$S(e^{j2\pi f}, e^{j2\pi g}) = C(e^{j2\pi f}, e^{j2\pi g})H(e^{j2\pi f}, e^{j2\pi g}). \tag{3.65}$$

We can see that in this particular configuration the complete image superimposition system can be described as a linear, position-invariant (LPI) system.[5] Graphically, the system represented in Figure 3.6 can be modeled with a single block, as shown in Figure 3.8. The consequences of this fact for the determination of the optimal signal $c[m, n]$ are analyzed in the next chapter.

[5]Here we follow the convention used for imaging applications. These systems are also called time-invariant.

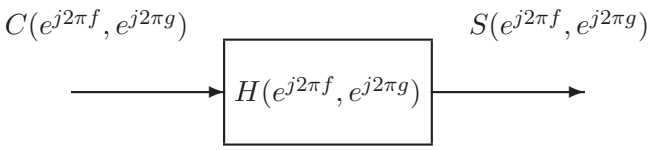

Figure 3.8: Equivalent system for image generation, projection, and sampling.

The equivalent equations for one-dimensional systems are obtained by using $\delta = 1$ in (3.58), which results in

$$t[m, n] = \lambda(m - n), \quad m, n \in \mathbb{Z}. \tag{3.66}$$

Thus, if we define

$$h[m] = \lambda(m) = \int_{-\infty}^{\infty} \phi(x)\zeta(m - x)\,\mathrm{d}x, \quad m \in \mathbb{Z}. \tag{3.67}$$

we have (3.57) equal to

$$s[m] = (c * h)[m] = \sum_{n=-\infty}^{\infty} c[n]h[m - n]. \tag{3.68}$$

In this case, we have the one-dimensional z-transforms (2.1) satisfying

$$S(z) = H(z)\,C(z), \tag{3.69}$$

and

$$H(e^{j2\pi f}) = \sum_{k=-\infty}^{\infty} \Lambda(f - k) = \sum_{k=-\infty}^{\infty} \Phi(f - k)Z(f - k). \tag{3.70}$$

3.3.2 Rational Sampling Factors

For understanding the general form in which sampling rates define resolution, let us consider first the one-dimensional superimposition. The combination of (3.57) and (3.58) produces

$$s[m] = \sum_{n=-\infty}^{\infty} c[n]\lambda(m - n\delta). \tag{3.71}$$

In this case δ corresponds to the ratio between the average number of sampled pixels $s[m]$ and the average number of pixel values $c[m]$ that are fed to the P subframes, per unit of length. Note that this number is not uniquely defined by the number of subframes.

For example, if $\delta = 1/4$ then, in Figure 3.4, we have the superimposed projected image with four times more resolution[6] than that captured by the "camera." On the other hand, if $\delta = 4$ then we have the inverse situation: the camera samples pixels at a rate four times larger than that defined by the projected image.

In conclusion, we can set $\delta < 1$ when we do not desire to achieve the highest possible resolution. The case $\delta > 1$ corresponds to the situations in which we want to evaluate the quality of the projected image at resolutions higher than that defined by the original image samples (by $r[m]$). For instance, we can use this choice in order to have better control over the high frequency components of the superimposed image. Setting δ to increasingly larger values leads to the analysis that would be done comparing images defined by continuous values. However, a practical problem is how to determine the comparison criterion at such high resolutions, since it has to be based on some form of interpolated data.

The general case can be studied considering the cases when δ is a rational number, i.e., $\delta = p/q$, where p and q are positive integers. We have (3.71) in the form

$$s[m] = \sum_{n=-\infty}^{\infty} c[n]\lambda(m - np/q), \tag{3.72}$$

and we can observe the identity

$$s[m + kp] = \sum_{n=-\infty}^{\infty} c[n + kq]\lambda(m - np/q), \quad \forall k, m \in \mathbb{Z}. \tag{3.73}$$

This property, i.e., the periodic repetition of terms in the sum, can be used to simplify the model, as defined by the following theorem for one-dimensional systems.

Theorem 3.3.1 *When $\delta = p/q$, where p and q are positive integers, the one-dimensional superimposition system can be modeled by a multi-rate linear and spatially invariant system. If the driver sequence $c[m]$ is upsampled by factor p according to*

$$\tilde{c}[k + mp] = \begin{cases} c[m], & k = 0, \\ 0, & k = 1, 2, \ldots, p - 1, \end{cases} \qquad \forall\, m \in \mathbb{Z} \tag{3.74}$$

and this sequence is convolved with a sequence

$$h[m] = \lambda(m/q), \tag{3.75}$$

then the resulting sequence

$$\tilde{s}[m] = (\tilde{c} * h)[m] = \sum_{n=-\infty}^{\infty} \tilde{c}[n]h[m - n], \tag{3.76}$$

[6]We are using the word resolution here in a loose way, related to number of addressable image elements, not information bandwidth.

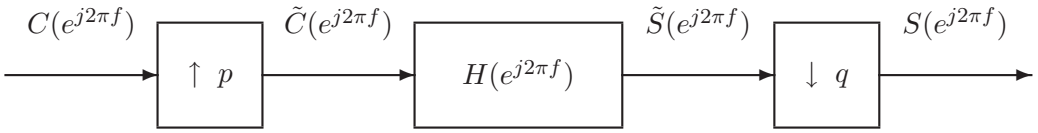

Figure 3.9: Complete system for image generation, projection, and sampling, when $\delta = p/q$.

can be downsampled by factor q to obtain the samples of the superimposed image, as

$$s[m] = \tilde{s}[mq]. \tag{3.77}$$

Proof: Defining

$$\Delta(x) = \begin{cases} 0, & x = 0, \\ 1, & x \neq 0, \end{cases} \tag{3.78}$$

we have a convenient way to represent $\tilde{c}[m]$ as

$$\tilde{c}[m] = \sum_{k=-\infty}^{\infty} \Delta(k - m/p)c[k]. \tag{3.79}$$

Using this representation we have

$$\begin{aligned} \tilde{s}[mq] &= \sum_{n=-\infty}^{\infty} \tilde{c}[n]\lambda(m - n/q) \\ &= \sum_{n=-\infty}^{\infty} \sum_{k=-\infty}^{\infty} \Delta(k - n/p)c[k]\lambda(m - n/q) \qquad (3.80) \\ &= \sum_{k=-\infty}^{\infty} c[k]\lambda(m - kp/q) \qquad (3.81) \end{aligned}$$

which is equivalent to (3.72).

$\mathcal{Q}.\mathcal{E}.\mathcal{D}.$

Figure 3.9 show how the superimposition can be modeled as a multirate system [12]. While mathematically the this result does not apply to cases when α is an irrational number, for practical purposes we can always approximate α with increasingly better rational values.

Note that in the frequency domain we have

$$\tilde{C}(e^{j2\pi f}) = C(e^{j2\pi fp}) \tag{3.82}$$

and

$$\begin{aligned} S(e^{j2\pi f}) &= \frac{1}{q}\sum_{k=0}^{q-1}\tilde{S}(e^{j2\pi(f-k)/q}) \\ &= \frac{1}{q}\sum_{k=0}^{q-1}C(e^{j2\pi(f-k)p/q})H(e^{j2\pi(f-k)/q}). \end{aligned} \tag{3.83}$$

Chapter 4

Frequency-domain Solutions

In the previous chapter we have shown that, if we have the set of pixel values $c_p[m, n]$ that are fed to the subframes, the whole image superimposition system is linear, and many configurations can be studied using frequency-domain analysis. Here we consider the properties of these linear systems, and start analyzing how to choose optimal solutions $c_p[m, n]$.

In order to simplify the presentation, in this chapter we start by analyzing one-dimensional models corresponding to systems of Section 3.3, and then show the equations for two-dimensional cases. Figure 4.1 shows a diagram with the general model for that type of one-dimensional image superimposition, including the generation of the driver sequence $c[m]$, which we want to be chosen so that $s[m]$ approximates $r[m]$ as well as possible.

Note that these pixel values correspond to the desired light output, which we assume are normalized, so $c[m] \in [0, 1]$ represents the projector's physical limits. In Figure 4.1 we show the enforcement of these constraints through a clipping box. Since the signal design problem that incorporates this nonlinear process does not have closed-form solutions, and cannot be fully analyzed, in this chapter we consider how the problem can be solved in the frequency-domain when these physical constraints are ignored.

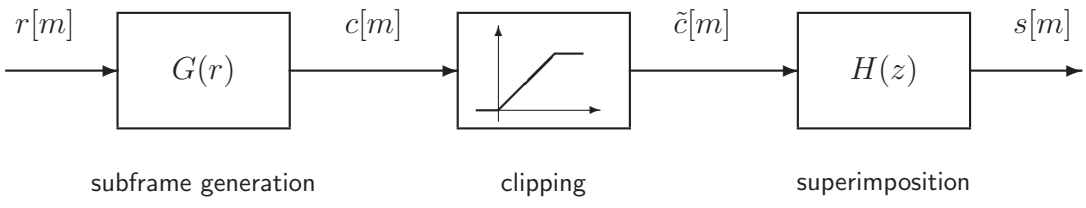

Figure 4.1: General model representing superimposition of equally-shifted subframes.

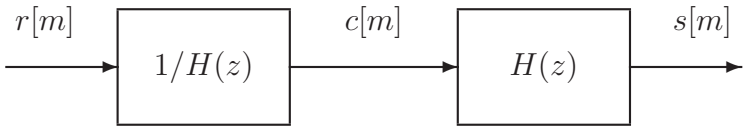

Figure 4.2: Inverse system for computation of optimal subframe driver sequence $c[m]$, when it is unconstrained.

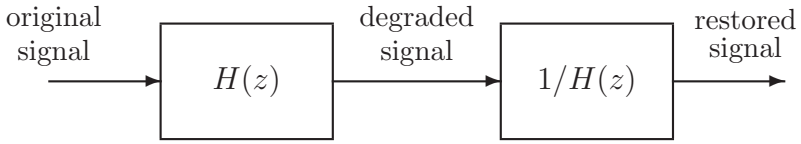

Figure 4.3: Configuration for common inverse filtering problems, like equalization, deblurring, and restoration.

4.1 Exact Solution via Inverse Filtering

Considering equation (3.69), we can see that if we want to have an exact solution to the superimposition problem, with $s[m] = r[m]$, then we can immediately use

$$C(z) = \frac{R(z)}{H(z)}, \tag{4.1}$$

and conclude that if a system with response $1/H(z)$ exists,[1] then $c[m]$ can be computed by simply filtering of the reference sequence $r[m]$, as shown in Figure 4.2.

This process, called *inverse filtering* or *deconvolution*, is a well-known signal processing technique. One important fact is that some of the constraints commonly imposed on inverse filters [5, § 5.2.2], like minimum phase, are required only when the filters need to be causal. This requirement, needed in applications like channel equalization [7, § 6.4], is not commonly required in imaging, where deconvolution can be used for deblurring and restoration [2, 8, 34].

The advantage of using the z-transform is that in some cases we can study the spectral decomposition of $H(z)$, i.e., analyze where are the zeros of $H(z)$ to know when the inverse exists.

[1] A more rigorous approach requires studying the region of convergence of the series defining $H(z)$. We simply assume that it converges on the unit circle, and thus the Fourier transform $H(e^{j2\pi f})$ exists.

One very important difference is that with the superimposed image we have a pre-filtering problem (as shown in Figure 4.2), while common image restoration problems correspond to post-filtering, as shown in Figure 4.3. The mathematical tools are very similar, but in the two cases we encounter very different numerical problems.

- In the post-filtering (restoration) case the signal components that can cause instability are first removed or strongly attenuated by the filter $H(z)$. Without noise, $1/H(z)$ only has to restore signal components to their original amplitude, so there is no expectation of large signal values that may cause overflow or underflow. Stability problems can occur due to the presence of noise, but they may not be severe because the noise amplitude can be expected to be very small.
- In the pre-filtering case some signal components may have to be highly amplified by $1/H(z)$, in order to reverse the later attenuation caused by $H(z)$. Different from low-amplitude noise, these signals have full amplitude at the input of filter $1/H(z)$, and consequently the occurrence of overflow or underflow is much more probable.

While these pre-filtering difficulties can be serious for any system, it is important to keep in mind that they are particularly harmful in our image superimposition problem because the dynamic range of projectors is severely limited by physical factors, as indicated the system of Figure 4.1.

Figure 4.4 shows one type of implementation of inverse filtering. If the Fourier transform is such that $H(e^{j2\pi f}) \neq 0$ for all $f \in [0, 1)$, then we can always compute the desired driver sequence $c[m]$ to obtain $s[m] = r[m]$, simply by computing

$$C(e^{j2\pi f}) = \frac{R(e^{j2\pi f})}{H(e^{j2\pi f})} = \frac{R(e^{j2\pi f})\bar{H}(e^{j2\pi f})}{|H(e^{j2\pi f})|^2}, \quad f \in [0, 1), \tag{4.2}$$

and then computing the inverse transform of $C(e^{j2\pi f})$.

In practice inverse filtering is implemented using some version of the fast Fourier transform algorithm (FFT) [13, § 13.1].

The two-dimensional version of the inverse filtering operation can also be described using Fourier transforms:

$$C(e^{j2\pi f}, e^{j2\pi g}) = \frac{R(e^{j2\pi f}, e^{j2\pi g})}{H(e^{j2\pi f}, e^{j2\pi g})} = \frac{R(e^{j2\pi f}, e^{j2\pi g})\, \bar{H}(e^{j2\pi f}, e^{j2\pi g})}{|H(e^{j2\pi f}, e^{j2\pi g})|^2}. \tag{4.3}$$

4.2 Filters for Approximation

The main caveat in the straightforward use of the inverse filter operation is that if $H(z) = 0$ at any point in the unit circle, then it is mathematically impossible to obtain a sequence of pixel values $c[m]$ such that $s[m] = r[m]$.

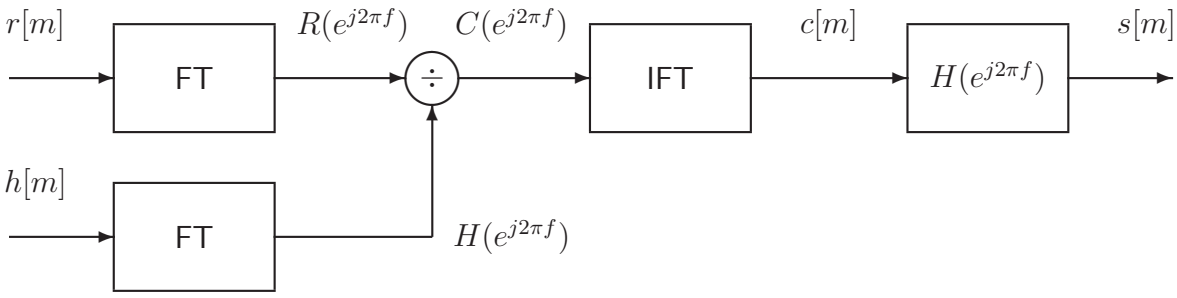

Figure 4.4: Use of the Fourier transform for computation of optimal driver sequence $c[m]$, when it is unconstrained.

1. In practice, we can have numerical instability not only when $H(z)$ is exactly equal to zero, but also whenever $|H(z)|$ is very small.
2. We show in Chapter 5 that in all cases of practical importance $H(z)$ has the behavior of a lowpass filter, and in many cases we can prove that zeros of $H(z)$ lie in the unit circle.

Furthermore, it is important to keep in mind that in the end we need a solution such that $0 \leq c[m] \leq 1$. Thus, even moderately small values of $|H(z)|$ can lead to problems for finding good solutions.

There are two alternatives to deal with this problem, and both require relaxing the demands for the type of solution we can obtain. The first approach, which is studied in this section, is to accept the fact that the exact inverse may not exist, and look for approximations that are optimal in some sense, i.e., we look for $c[m]$ such that $s[m]$ is a good approximation of $r[m]$. The second approach is to reduce the resolution requirements, and is discussed in Section 4.3.

When we use the inverse filtering approach, it is the occurrence of relatively large values of $1/\left|H(e^{j2\pi f})\right|$ that make the solutions violate constraints $c[m] \in [0,1]$. There are simple ways to alleviate the problem by allowing approximate solutions. A standard technique is to use a *pseudo-inverse* in the form [28, § 10.2]

$$1/\tilde{H}(e^{j2\pi f}) = \begin{cases} 1/H(e^{j2\pi f}), & \left|H(e^{j2\pi f})\right| \geq \xi, \\ \xi \exp(-j \arg[H(e^{j2\pi f})]), & \text{otherwise}, \end{cases} \tag{4.4}$$

where ξ is a small positive constant.

Here we investigate another interesting set of solutions, comprehending those that minimize a weighted sum of the squared error and the sum of $(c[m] - 1/2)^2$. Before formulating the optimization problem, we have to consider that, since we are dealing with infinite sequences, adding constants to $c[m]$ creates complications regarding the

convergence of series, and the existence of the Fourier transforms. To avoid having to introduce Dirac's delta functions and more notation, we consider first a simpler problem.

Theorem 4.2.1 *The driver sequence $c[m]$ that minimizes the weighted sum*

$$\Gamma(c) = \sum_{m=-\infty}^{\infty} \left[(r[m] - s[m])^2 + w\,(c[m])^2 \right], \quad w \geq 0, \tag{4.5}$$

has Fourier transform

$$C(e^{j2\pi f}) = \frac{R(e^{j2\pi f})\bar{H}(e^{j2\pi f})}{w + |H(e^{j2\pi f})|^2}, \quad f \in [0,1), \tag{4.6}$$

where $\bar{H}(e^{j2\pi f})$ is the complex conjugate of $H(e^{j2\pi f})$.

In this case, the Fourier transform of the resulting signal is

$$S(e^{j2\pi f}) = \frac{R(e^{j2\pi f})\left|H(e^{j2\pi f})\right|^2}{w + |H(e^{j2\pi f})|^2}, \quad f \in [0,1), \tag{4.7}$$

and the magnitude of the transform is limited by

$$\left|C(e^{j2\pi f})\right| \leq \frac{\left|R(e^{j2\pi f})\right|}{2\sqrt{w}}. \tag{4.8}$$

Proof: Using Parseval's Theorem [5, § 2.9], we have

$$\begin{aligned}
\Gamma(c) &= \int_0^1 \left[\left|R(e^{j2\pi f}) - H(e^{j2\pi f})C(e^{j2\pi f})\right|^2 + w\left|C(e^{j2\pi f})\right|^2 \right] df \qquad (4.9)\\
&= \int_0^1 \left[\left(w + \left|H(e^{j2\pi f})\right|^2 \right) \left|C(e^{j2\pi f})\right|^2 - 2\Re\left\{ R(e^{j2\pi f})\bar{H}(e^{j2\pi f})\bar{C}(e^{j2\pi f}) \right\} \right] df + \\
&\quad \int_0^1 \left|R(e^{j2\pi f})\right|^2 df.
\end{aligned}$$

Since the integrand cannot be negative, and $R(e^{j2\pi f})$ is constant, we can minimize the integral by minimizing the quadratic equation

$$\begin{aligned}
&\left(w + \left|H(e^{j2\pi f})\right|^2 \right) \left|C(e^{j2\pi f})\right|^2 - 2\Re\left\{ R(e^{j2\pi f})\bar{H}(e^{j2\pi f})\bar{C}(e^{j2\pi f}) \right\} = \\
&\left[\left(w + \left|H(e^{j2\pi f})\right|^2 \right) \Re\left\{ C(e^{j2\pi f}) \right\} - 2\Re\left\{ R(e^{j2\pi f})\bar{H}(e^{j2\pi f}) \right\} \right] \Re\left\{ C(e^{j2\pi f}) \right\} + \\
&\left[\left(w + \left|H(e^{j2\pi f})\right|^2 \right) \Im\left\{ C(e^{j2\pi f}) \right\} - 2\Im\left\{ R(e^{j2\pi f})\bar{H}(e^{j2\pi f}) \right\} \right] \Im\left\{ C(e^{j2\pi f}) \right\}
\end{aligned}$$

at every frequency $f \in [0, 1)$. The minimum, found by equating the partial derivatives to zero, occurs when

$$\begin{aligned} \Re\left\{C(e^{j2\pi f})\right\} &= \frac{\Re\left\{R(e^{j2\pi f})\bar{H}(e^{j2\pi f})\right\}}{w + |H(e^{j2\pi f})|^2}, \\ \Im\left\{C(e^{j2\pi f})\right\} &= \frac{\Im\left\{R(e^{j2\pi f})\bar{H}(e^{j2\pi f})\right\}}{w + |H(e^{j2\pi f})|^2}. \end{aligned} \tag{4.10}$$

Equation (4.7) results directly from the substitution of (4.6) into (3.69). It is useful for evaluating the overall response of the system after projection.

Equation 4.8 is obtained by using the fact that the maximum of the function

$$f(x) = \frac{x}{x^2 + w} \tag{4.11}$$

which occurs, for $w > 0$, when $x = \sqrt{w}$.

$\mathcal{Q.E.D.}$

Comparing (4.6) with (4.2) we can see that, with a sufficiently small but positive value of w, we can approximate the inverse while avoiding divisions by very small numbers or zero.

For sequences with finite length we can minimize the sum of $(c[m] - 1/2)^2$ instead of $(c[m])^2$ by changing the variables of the problem. Replacing $c[m]$ and $r[m]$ with

$$\begin{aligned} c'[m] &= c[m] - 1/2, \\ r'[m] &= r[m] - H(1)/2, \end{aligned} \tag{4.12}$$

we can use the DFT version of Theorem 4.2.1 for finding the optimal solution, and then use $c[m] = c'[m] + 1/2$.

Note in equation (4.6) that larger values of w increase the attenuation in all frequencies. This is conveniently similar to the technique of reducing the dynamic range in $r[m]$ to avoid overflow and underflow, and equation (4.6) provides an strategy that is optimal in a well-defined sense. However, it should be clear that in both cases we can have a significant degradation in contrast.

Since in our case $H(z)$ must necessarily be a type of lowpass filter, we can use the value $H(1)$ as reference, and avoid attenuation at low frequencies by replacing (4.6) with

$$C(e^{j2\pi f}) = \left[1 + \frac{w}{|H(1)|^2}\right] \left[\frac{R(e^{j2\pi f})\bar{H}(e^{j2\pi f})}{w + |H(e^{j2\pi f})|^2}\right], \quad f \in [0, 1). \tag{4.13}$$

4.3 Subcritical Systems

As explained in Section 4.2, another approach to alleviate the problems with the inverse filter is to reduce the resolution requirements. In this section we study an approach that produces exact inverses, but on a coarser resolution grid.

For example, suppose we have four subframes. We can consider how well we can do if we try to increase resolution by a factor of two or three, instead of four. In our basic model (3.25), a threefold increase in resolution using four subframes corresponds to using pixels with size $\ell = 3$ and shift $\delta = 3/4$. We analyze if this extra degree of freedom can produce solutions that do not require high gains for inverse filtering.

4.3.1 Rational Factors

When $\delta < 1$ we have a set of conditions for obtaining $s[m] = r[m]$ that is in a way "overdetermined" because the rate of samples of $c[m]$ exceeds the rate of samples of $s[m]$. In general, the set of Fourier transforms $C(e^{j2\pi f})$ that satisfy (3.60) and such that $S(e^{j2\pi f}) = R(e^{j2\pi f})$,

$$\Xi = \left\{ C(e^{j2\pi f}) : \sum_{k=-\infty}^{\infty} C(e^{j2\pi\epsilon[f-k]})\Lambda(f-k) = R(e^{j2\pi f}), \forall f \in [0,1) \right\}, \tag{4.14}$$

contains many elements, and we need ways to characterize the sets of solutions.

Below we show that with rational shifts, i.e., when $\delta = p/q$, where p and q are relatively prime positive integers, we can find sufficient conditions and define solutions using the properties of $p \times q$ matrices.

Theorem 4.3.1 *Let us consider rational shifts $\delta = p/q < 1$, where p and q are relatively prime positive integers, a reference sequence $r[m]$ with Fourier transform $R(e^{j2\pi f})$, and pixel light intensity profile $\phi(x)$ and sampling function $\zeta(x)$, with Fourier transforms $\Phi(f)$ and $Z(f)$, respectively.*

In addition, for each $\alpha \in [0,1)$ we define the p-dimensional complex vector $\mathbf{r}(\alpha)$ and the q-dimensional complex vector $\mathbf{c}(\alpha)$ as

$$r_m(\alpha) \doteq R(e^{j2\pi[\alpha+m]/p}), \quad m = 0, 1, \ldots, p-1, \tag{4.15}$$

$$c_n(\alpha) \doteq C(e^{j2\pi[\alpha+n]/q}), \quad n = 0, 1, \ldots, q-1, \tag{4.16}$$

and also define the $p \times q$ complex matrix $\mathbf{A}(\alpha)$ such that

$$A_{m,n}(\alpha) \doteq \sum_{k=-\infty}^{\infty} \Lambda\left(\frac{\alpha+m}{p} - kq - [[p^{-1}]_q(m-n)]_q \right), \tag{4.17}$$

where $\Lambda(f)$ is defined by (3.61), and

$$[n]_q = n - q\lfloor n/q \rfloor, \tag{4.18}$$

defines operations modulo q, and $[p^{-1}]_q$ is the unique inverse modulo q of p, i.e.,

$$[p^{-1}]_q p \equiv 1 \,(\mathrm{mod}\ q). \tag{4.19}$$

Under these conditions all functions $C(e^{j2\pi f})$ that satisfy the matrix equations

$$\mathbf{A}(\alpha)\mathbf{c}(\alpha) = \mathbf{r}(\alpha), \quad \forall \alpha \in [0,1), \tag{4.20}$$

result in

$$S(e^{j2\pi f}) = R(e^{j2\pi f}), \quad \forall f \in [0,1). \tag{4.21}$$

Proof: Let us consider the function $S(e^{j2\pi f})$ for f in the disjoint intervals

$$\{[0,1/p), [1/p, 2/p), \ldots, [1-1/p, 1)\}. \tag{4.22}$$

From (3.60) we know that, for all $\alpha \in [0,1)$ and $m = 0, 1, \ldots, p-1$,

$$\begin{aligned} S(e^{j2\pi[\alpha+m]/p}) &= \sum_{k=-\infty}^{\infty} C(e^{j2\pi p[(\alpha+m)/p-k]/q})\Lambda\left(\frac{\alpha+m}{p} - k\right) \\ &= \sum_{k=-\infty}^{\infty} C(e^{j2\pi[\alpha+m-pk]/q})\Lambda\left(\frac{\alpha+m}{p} - k\right). \end{aligned} \tag{4.23}$$

We can decompose the infinite sum into two sums by defining $k = ql + \omega$, where $\omega \in [0, q-1]$, and obtain

$$\begin{aligned} S(e^{j2\pi[\alpha+m]/p}) &= \sum_{l=-\infty}^{\infty}\sum_{\omega=0}^{q-1} C(e^{j2\pi[\alpha+m-pql-p\omega]/q})\Lambda\left(\frac{\alpha+m}{p} - ql - \omega\right) \\ &= \sum_{l=-\infty}^{\infty}\sum_{\omega=0}^{q-1} C(e^{j2\pi[\alpha+m-p\omega]/q})\Lambda\left(\frac{\alpha+m}{p} - ql - \omega\right). \end{aligned} \tag{4.24}$$

Since p and q are relatively prime we have [15]

$$\bigcup_{\omega=0}^{q-1}\{(m - p\omega) \,(\mathrm{mod}\ q)\} = \{0, 1, \ldots, q-1\} \tag{4.25}$$

and from (4.19) we have

$$(p\,[[p^{-1}]_q(m-n)]_q) \equiv (m-n)(\mathrm{mod}\ q). \tag{4.26}$$

The substitution of ω by $[[p^{-1}]_q(m-n)]_q$ produces

$$\begin{aligned} S(e^{j2\pi[\alpha+m]/p}) &= \sum_{l=-\infty}^{\infty}\sum_{n=0}^{q-1} C(e^{j2\pi[\alpha+m-(m-n)]/q})\Lambda\left(\frac{\alpha+m}{p} - ql - [[p^{-1}]_q(m-n)]_q\right) \\ &= \sum_{n=0}^{q-1} C(e^{j2\pi[\alpha+n]/q}) \sum_{l=-\infty}^{\infty}\Lambda\left(\frac{\alpha+m}{p} - ql - [[p^{-1}]_q(m-n)]_q\right) \quad (4.27) \\ &= \sum_{n=0}^{q-1} A_{m,n}(\alpha)c_n(\alpha). \end{aligned}$$

Thus, if

$$\mathbf{A}(\alpha)\mathbf{c}(\alpha) = \mathbf{r}(\alpha) \quad (4.28)$$

then

$$S(e^{j2\pi f}) = R(e^{j2\pi f}), \quad \forall f \in [0,1). \quad (4.29)$$

$\mathcal{Q}.\mathcal{E}.\mathcal{D}.$

Note that we avoided reaching the conclusion that the sequences $c[m]$ obtained from computing the inverse Fourier transform of any of the functions $C(e^{j2\pi f})$ that satisfy the conditions of Theorem 4.3.1 result in $s[m] = r[m]$. The theoretical problem is that the theorem specifies pointwise solutions for $C(e^{j2\pi f})$, but does not guarantee that such solutions correspond to analytic functions.

However, it is easy to derive a version of Theorem 4.3.1 for finite sequences (with sequence lengths that are multiples of pq) which defines similar relations between Discrete Fourier Transforms, and the inverse transforms always exist.

While it is beyond the objectives of this work to rigorously analyze all the subtleties regarding the set of functions Ξ, we show next that we can effectively use this result to define good solutions, in a closed form that correspond to analytic functions.

Theorem 4.3.2 *Given a rational shift $\delta = p/q$, where p and q are relatively prime positive integers, a reference sequence $r[m]$ with Fourier transform $R(e^{j2\pi f})$, and pixel light intensity profile $\phi(x)$ and sampling functions and $\zeta(x)$, with Fourier transforms $\Phi(f)$ and $Z(f)$, and $\mathbf{r}(\alpha)$, $\mathbf{c}(\alpha)$ and $\mathbf{A}(\alpha)$ as defined in Theorem 4.3.1.*

If the q-dimensional vector $\mathbf{c}(\alpha)$ defined by

$$\mathbf{c}(\alpha) = \mathbf{A}^{\mathsf{H}}(\alpha)\left[\mathbf{A}(\alpha)\mathbf{A}^{\mathsf{H}}(\alpha)\right]^{-1}\mathbf{r}(\alpha), \quad (4.30)$$

exists, then function $C(e^{j2\pi f})$ corresponding to $\mathbf{c}(\alpha)$ simultaneously satisfies $S(e^{j2\pi f}) = R(e^{j2\pi f})$ and minimizes the integral

$$\int_0^1 \left|C(e^{j2\pi f})\right|^2 df. \quad (4.31)$$

Proof: We can minimize the integral (4.31) by minimizing $\left|C(e^{j2\pi f})\right|$ for every f, subject to the constraints defined by (4.28). This corresponds to solving, for each $\alpha \in [0,1)$, the optimization problem

$$\begin{array}{ll} \text{Minimize}_{\mathbf{c}(\alpha)} & |\mathbf{c}(\alpha)|^2, \\ \text{subject to} & \mathbf{A}(\alpha)\mathbf{c}(\alpha) = \mathbf{r}(\alpha). \end{array} \tag{4.32}$$

This result is similar to the computation of the pseudo-inverse for real-valued matrices, and we need to only show that the solution for complex matrices and vectors corresponds to (4.30). To simplify notation we remove the dependence on α, and define real-valued vectors $\tilde{\mathbf{r}}$ and $\tilde{\mathbf{c}}$, and matrix $\tilde{\mathbf{A}}$ such that

$$\begin{array}{rclrcl} \tilde{r}_{2j} & = & \Re\{r_i\}, & \tilde{r}_{2i+1} & = & \Im\{r_i\}, \\ \tilde{c}_{2j} & = & \Re\{c_j\}, & \tilde{c}_{2j+1} & = & \Im\{c_j\}, \\ \tilde{A}_{2i,2j} & = & \Re\{A_{i,j}\}, & \tilde{A}_{2i,2j+1} & = & -\Im\{A_{i,j}\}, \\ \tilde{A}_{2i+1,2j} & = & \Im\{A_{i,j}\}, & \tilde{A}_{2i+1,2j+1} & = & \Re\{A_{i,j}\}, \end{array} \tag{4.33}$$

for $i = 0, 1, \ldots, p-1$, $j = 0, 1, \ldots, q-1$

With this new notation the optimization problem (4.32) is identical to

$$\begin{array}{ll} \text{Minimize}_{\tilde{\mathbf{c}}} & \tilde{\mathbf{c}}^{\mathsf{T}}\tilde{\mathbf{c}}, \\ \text{subject to} & \tilde{\mathbf{A}}\tilde{\mathbf{c}} = \tilde{\mathbf{r}}. \end{array} \tag{4.34}$$

If there is an optimal solution, then it is defined by [3]

$$\tilde{\mathbf{c}} = \tilde{\mathbf{A}}^{\mathsf{T}}\left(\tilde{\mathbf{A}}\tilde{\mathbf{A}}^{\mathsf{T}}\right)^{-1}\tilde{\mathbf{r}}. \tag{4.35}$$

which is identical to (4.30).

$\mathcal{Q}.\mathcal{E}.\mathcal{D}.$

The result in Theorem 4.3.2 may seem of little practical significance since the computation of $C(e^{j2\pi f})$ requires computing an infinite (in fact, uncountable) number of matrix inversions and products defined by (4.30).

The next two results are direct consequence of Theorem 4.30, considering the cases $p = 1$ and $p = 2$, when we can replace the matrix inverses with closed forms.

Corollary 4.3.3 *If $\delta = 1/q$ then the minimum-energy driver sequence $c[m]$ that results in $s[m] = r[m]$ is defined, for $n = 0, 1, \ldots, q-1$, by*

$$C(e^{j2\pi[f+n]/q}) = \frac{R(e^{j2\pi f})\bar{A}_n(f)}{|A_0(f)|^2 + |A_1(f)|^2 + \cdots + |A_{q-1}(f)|^2}, \quad \forall f \in [0,1), \tag{4.36}$$

where

$$A_n(f) \doteq \sum_{k=-\infty}^{\infty} \Lambda(f - n - kq), \quad n = 0, 1, \ldots, q-1. \tag{4.37}$$

Note that there is some similarity between (4.6) and (4.36). In the first case we have the positive constant w that avoid divisions by zero. In (4.36) we have several non-negative factors, and division by zero occurs only in the improbable case in which all factors are equal to zero.

Corollary 4.3.4 *If $\delta = 2/q$, where q is an odd positive integer, then the minimum-energy driver sequence $c[m]$ that results in $s[m] = r[m]$ is defined, for $n = 0, 1, \ldots, q-1$, by*

$$\begin{aligned} C(e^{j2\pi[f+n]/q}) &= \frac{[\bar{A}_{0,n}(f)B_{1,1}(f) - \bar{A}_{0,n}(f)\bar{B}_{0,1}(f)]R(e^{j\pi f})}{B_{0,0}(f)B_{1,1}(f) - |B_{0,1}|^2} + \\ & \frac{[\bar{A}_{1,n}(f)B_{0,0}(f) - \bar{A}_{0,n}(f)B_{0,1}(f)]R(e^{j\pi(f+1)})}{B_{0,0}(f)B_{1,1}(f) - |B_{0,1}|^2}, \quad \forall f \in [0,1), \end{aligned} \tag{4.38}$$

where

$$\begin{aligned} A_{0,n}(f) &= \sum_{k=-\infty}^{\infty} \Lambda\left(\frac{f}{2} - kq + \left[\frac{(q+1)n}{2}\right]_q\right), \\ A_{1,n}(f) &= \sum_{k=-\infty}^{\infty} \Lambda\left(\frac{f+1}{2} - kq + \left[\frac{(q+1)(n-1)}{2}\right]_q\right), \\ B_{0,0}(f) &= \sum_{n=0}^{q-1} |A_{0,n}(f)|^2 \\ B_{1,1}(f) &= \sum_{n=0}^{q-1} |A_{1,n}(f)|^2 \\ B_{0,1}(f) &= \sum_{n=0}^{q-1} A_{0,n}(f)\bar{A}_{1,n}(f). \end{aligned}$$

4.3.2 Approximated Solutions

The result in the previous section is very strict in the requirement that $S(e^{j2\pi f}) = R(e^{j2\pi f})$ for all $f \in [0, 1)$. Similarly to the cases in which we looked for the exact inverse filter for critical systems, the singular or ill-conditioned problems are not uncommon, and in fact cannot be avoided.

We can again use the technique of Section 4.2 to relax the equality constraints, and obtain approximated solutions.

Theorem 4.3.5 *Given a rational shift $\epsilon = p/q$, where p and q are relatively prime positive integers, a reference sequence $r[m]$ with Fourier transform $R(e^{j2\pi f})$, and pixel*

light intensity profile $\phi(x)$ and sampling functions and $\zeta(x)$, with Fourier transforms $\Phi(f)$ and $Z(f)$, and $\mathbf{r}(\alpha)$, $\mathbf{c}(\alpha)$ and $\mathbf{A}(\alpha)$ as defined in Theorem 4.3.1.

Using the q-dimensional vector $\mathbf{c}(\alpha)$ defined by

$$\mathbf{c}(\alpha) = \left[\mathbf{A}^{\mathsf{H}}(\alpha)\mathbf{A}(\alpha) + w\mathbf{I}\right]^{-1} \mathbf{A}^{\mathsf{H}}(\alpha)\mathbf{r}(\alpha), \tag{4.39}$$

with $w > 0$, the function $C(e^{j2\pi f})$ corresponding to $\mathbf{c}(\alpha)$ minimizes the integral

$$\int_0^1 \left(\left| S(e^{j2\pi f}) - R(e^{j2\pi f}) \right|^2 + w \left| C(e^{j2\pi f}) \right|^2 \right) df. \tag{4.40}$$

Chapter 5

Properties of Systems with Square Pixels

In this chapter we study the type of response we can find in practical situations, and start with what can be considered the simplest case, in which the pixels have square shape, and are arranged in a separable configuration, as described in Sections 3.1.4. In addition we start by considering square-shaped sampling functions (cf. Section 3.2).

Under these assumptions, the separable pixel light intensity profile (PLIP) $\phi(x)$, and the sampling function $\zeta(x)$ are equal to the functions $b_\ell(x)$ or $b_{\ell,\sigma}(x)$, defined by (2.13) and (2.14) in Section 2.3. In Section 5.2 we extend the analysis to $\phi(x) = b_{\ell,\sigma}(x)$, i.e., when the PLIP is defined assuming that optical anti-aliasing filters are used.

One very important issue in our formulation is how to align the origin of periodic repetition of the subframe pixels with the grid that defines the sampling (i.e., the "camera pixels" in Figure 3.4). Figure 5.1 shows a diagram where the pixel is shown in blue and the sampling grid in red. The offset between the origin of these two periodic patterns is $(\mu^{(x)}, \mu^{(y)})$, while $(\ell^{(x)}, \ell^{(y)})$ is the width and height of the pixel. The sampling period is always normalized to one.

In the one-dimensional model the offset is represented simply by μ. In this chapter we analyze how this value affects the superimposition inverse filtering problem, and consequently the quality of the images.

This problem may seem somewhat strange when we consider that when we visually evaluate the quality of an image we do not need an absolute system of coordinates. The answer to this paradox is in the comparison that is done in Figure 3.4). If humans had to evaluate quality using a semi-transparent template of the desired image, they would also have to move the template in front of their eyes to do the comparison. In our case the template position is fixed, but we move all the projected images, and

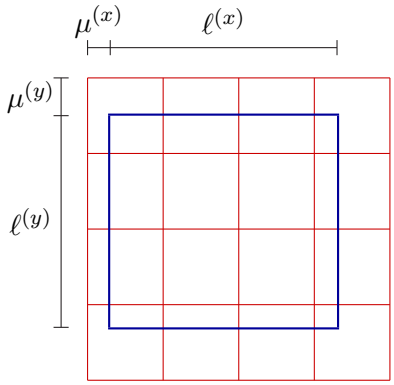

Figure 5.1: Diagram showing the alignment of the subframe pixels (blue) with the sampling grid (red).

only the fractional values become important. Thus, in this chapter we will normally assume that $\mu \in [0, 1)$.

5.1 Critically Sampled Systems

As explained in Section 3.3.1, a superimposition system is called critically sampled when we want to model the cases in which we have the maximum increase in resolution. Thus, we consider the impulse response $h[m]$ in the one-dimensional model defined by (3.68). Since we are particularly interested in the existence of the inverse filter, we analyze mostly its z-transform, $H(z)$.

Below we derive some results showing that, except in some nearly trivial cases, the image superposition problems are in a sense guaranteed to be ill-defined, and that in fact inverse filters do not exist for an important class of projection systems.

Lemma 5.1.1 *The impulse responses $h[m]$ of the systems resulting from pixel light intensity profiles $\phi(x) = b_\ell(x - \mu)$, $\ell = 1, 2, \ldots$, $\mu \in [0, 1]$, and sampling function $\zeta(x) = b_1(x)$, have z-transform*

$$H(z) = \frac{1}{\ell}\left(\mu z^{-1} + 1 - \mu\right) \prod_{k=1}^{\ell-1} \left(z^{-1} - e^{j2\pi k/\ell}\right). \tag{5.1}$$

Proof: The application of (3.67) yields the impulse response

$$h[m] = \frac{1}{\ell} \begin{cases} 1 - \mu, & m = 0, \\ 1, & m = 1, 2, \ldots, \ell - 1, \\ \mu, & m = \ell, \\ 0, & \text{otherwise.} \end{cases} \tag{5.2}$$

Its z-transform is the system function

$$H(z) = \frac{1}{\ell}\left[1 - \mu + z^{-1} + z^{-2} + \cdots + z^{1-\ell} + \mu z^{-\ell}\right]. \tag{5.3}$$

Multiplying by $(z^{-1} - 1)$ results in

$$\ell(z^{-1} - 1)H(z) = \mu z^{-\ell-1} + (1 - \mu)z^{-\ell} - \mu + z^{-1} - 1 + \mu, \tag{5.4}$$

and thus

$$H(z) = \frac{(z^{-\ell} - 1)(\mu z^{-1} + 1 - \mu)}{\ell(z^{-1} - 1)}. \tag{5.5}$$

The substitution of factorization

$$z^{-\ell} - 1 = \prod_{k=0}^{\ell-1}\left(z^{-1} - e^{j2\pi k/\ell}\right) \tag{5.6}$$

produces the desired result (5.1).

$\mathcal{Q}.\mathcal{E}.\mathcal{D}.$

Lemma 5.1.1 shows that when ℓ is an integer, the system function $H(z)$ has at least $\ell - 1$ zeros on the unit circle. If $\mu \neq 0$ then one of the zeros is always real and is equal to $\mu/(\mu - 1)$. Thus, this zero is in the interval $(-1, 0]$ when $\mu < 1/2$, equal to -1 when $\mu = 1/2$, and in the interval $(-\infty, -1)$ when $\mu > 1/2$. This means that $1/H(e^{j2\pi f})$ is undefined in at least $\ell - 1$ frequencies.

Figures 5.2 to 5.7 show the magnitude of the Fourier transform, $\left|H(e^{j2\pi f})\right|$, of the corresponding systems for small values of ℓ. Note how the attenuation of the high frequencies becomes more severe when ℓ increases. For $\ell \geq 2$ the first zero in the transform occurs at $f = 1/\ell$.

Since parameter μ is defined according to the choice of reference for pixel sampling, it can be chosen as the value that produces the best results. The frequency responses shown in Figures 5.2 to 5.7 indicate that $\mu = 0$ is always the best choice, since it results in the least attenuation of high frequencies. This is proved to be true in general in the following theorem.

Theorem 5.1.2 *Let $H(z)$ be the system functions obtained from pixel light intensity profiles $\phi(x) = b_\ell(x - \mu)$, $\ell = 1, 2, \ldots$, $\mu \in [0, 1)$, and sampling function $\zeta(x) = b_1(x)$. Defining*

$$\left|H_0(e^{j2\pi f})\right| = \frac{1}{\ell}\sqrt{\frac{1 - \cos(2\pi f\ell)}{1 - \cos(2\pi f)}}, \tag{5.7}$$

the corresponding Fourier transforms are such that

$$\left|H(e^{j2\pi f})\right| = \sqrt{1 - 2\mu(1 - \mu)[1 - \cos(2\pi f)]}\ \left|H_0(e^{j2\pi f})\right|, \tag{5.8}$$

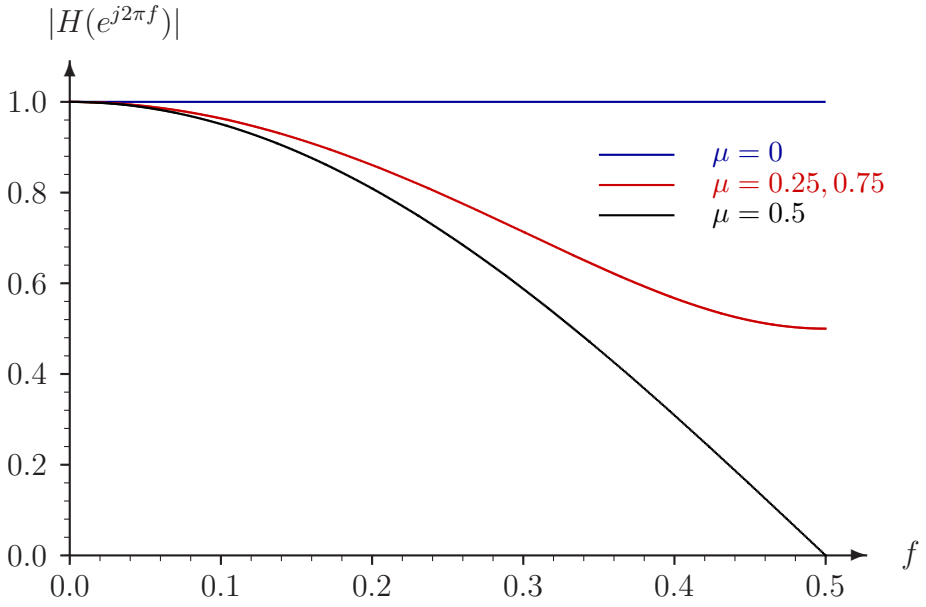

Figure 5.2: Frequency response of superimposition systems with sampling function $\zeta(x) = b_1(x)$ and PLIP $\phi(x) = b_1(x - \mu)$ $(\ell = 1)$.

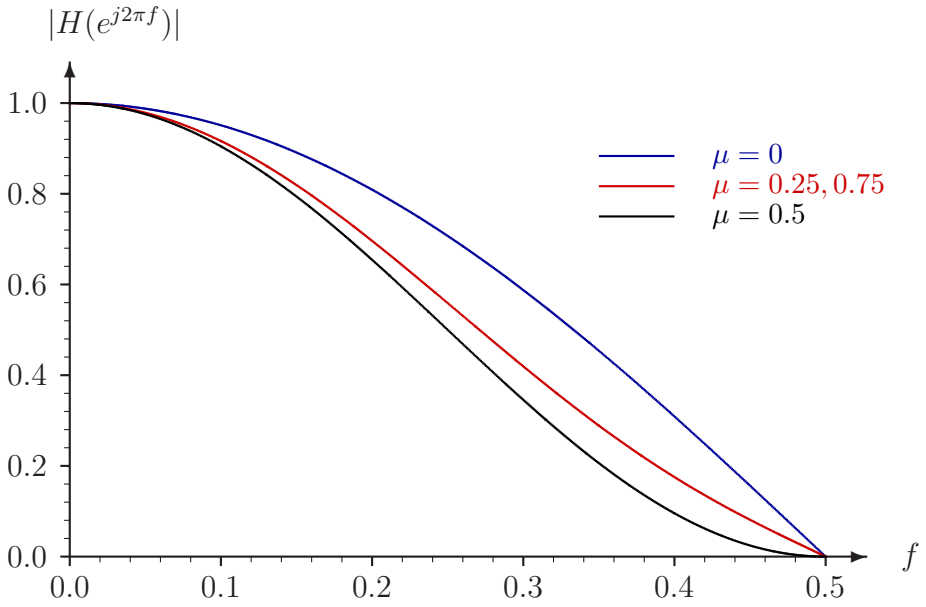

Figure 5.3: Frequency response of superimposition systems with sampling function $\zeta(x) = b_1(x)$ and PLIP $\phi(x) = b_2(x - \mu)$ $(\ell = 2)$.

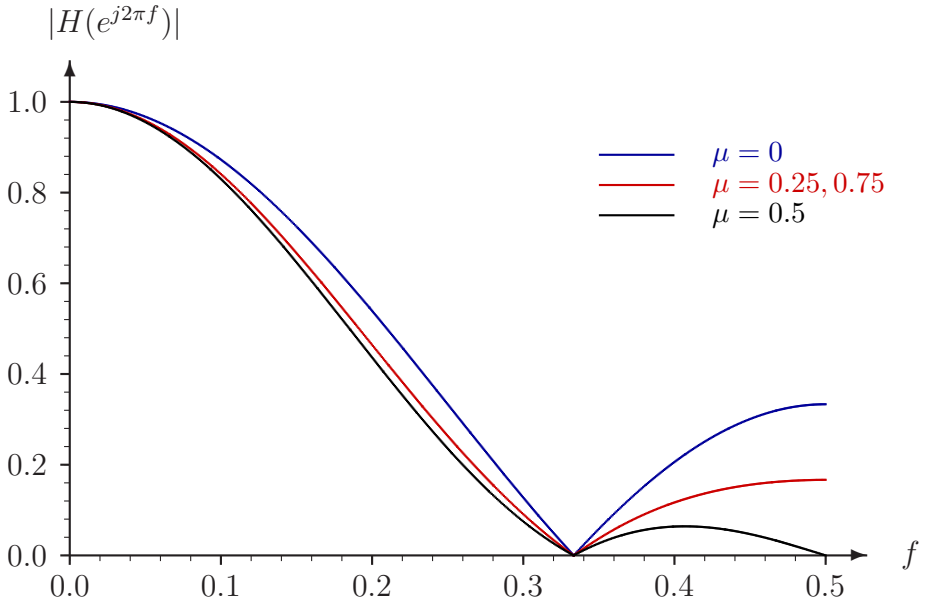

Figure 5.4: Frequency response of superimposition systems with sampling function $\zeta(x) = b_1(x)$ and PLIP $\phi(x) = b_3(x - \mu)$ $(\ell = 3)$.

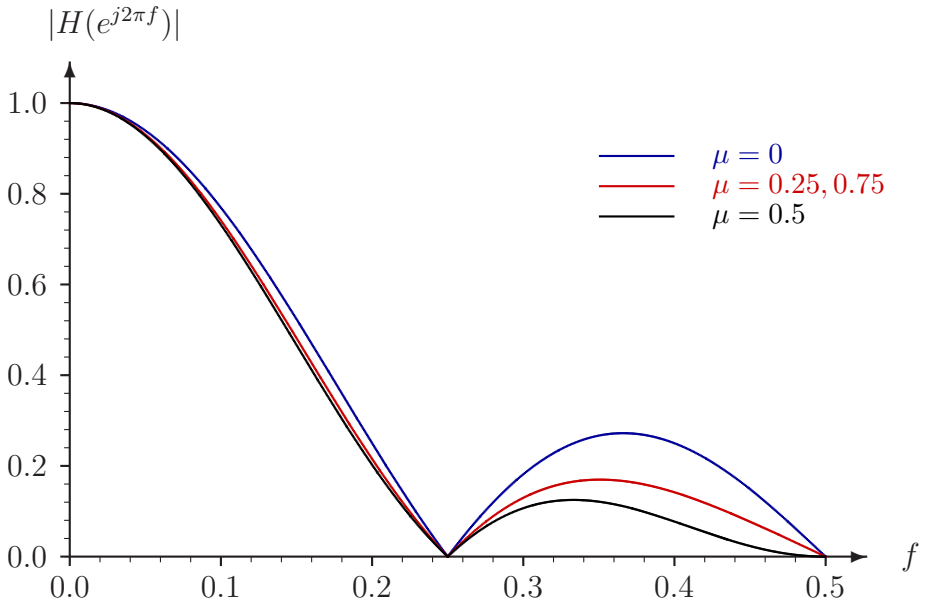

Figure 5.5: Frequency response of superimposition systems with sampling function $\zeta(x) = b_1(x)$ and PLIP $\phi(x) = b_4(x - \mu)$ $(\ell = 4)$.

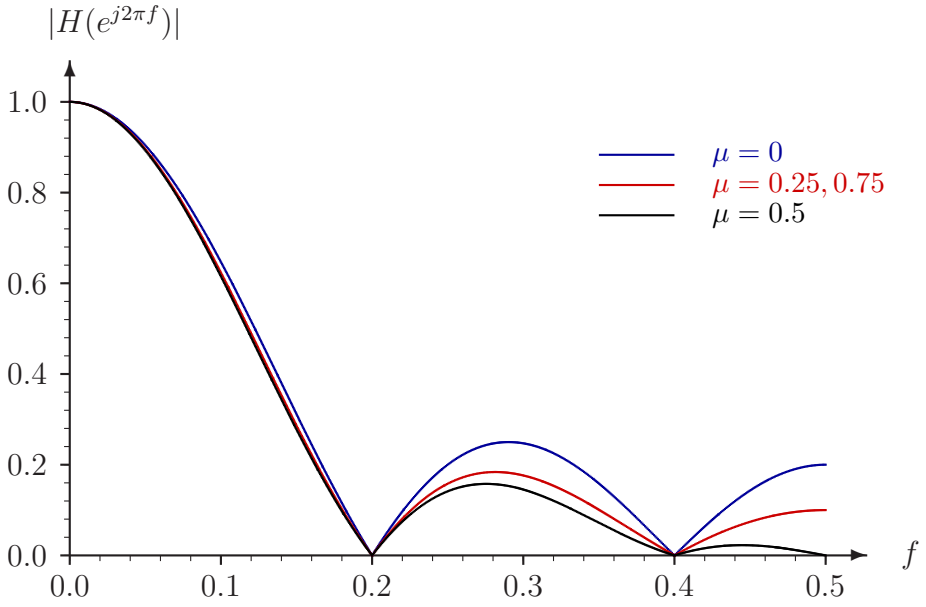

Figure 5.6: Frequency response of superimposition systems with sampling function $\zeta(x) = b_1(x)$ and PLIP $\phi(x) = b_5(x - \mu)$ $(\ell = 5)$.

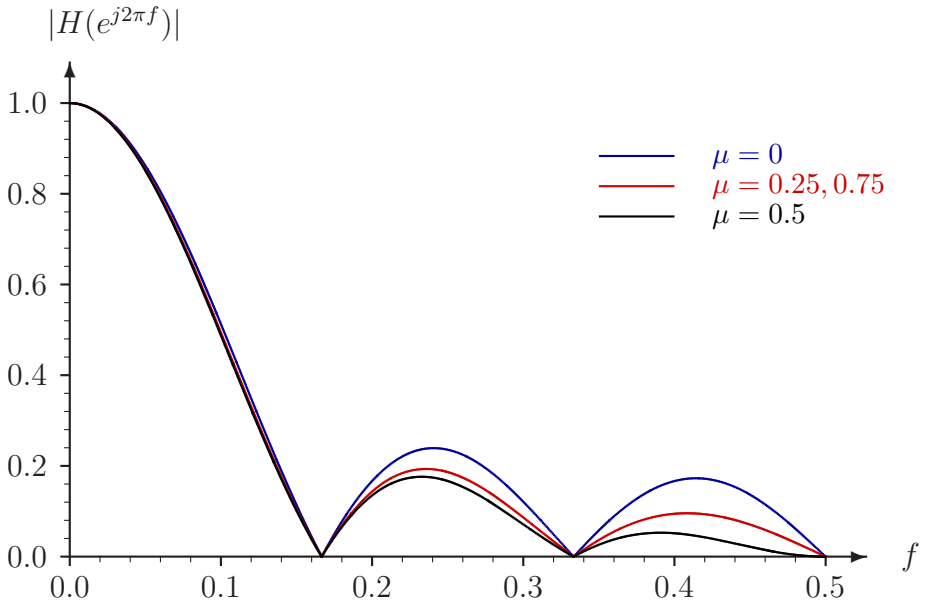

Figure 5.7: Frequency response of superimposition systems with sampling function $\zeta(x) = b_1(x)$ and PLIP $\phi(x) = b_6(x - \mu)$ $(\ell = 6)$.

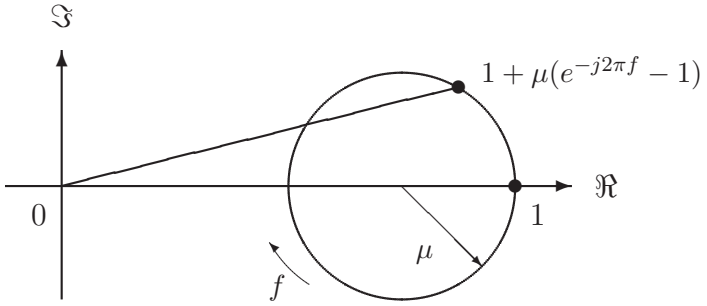

Figure 5.8: Complex-plane diagram showing factors used in the proof of Theorem 5.1.2.

and consequently

$$\left|H_0(e^{j2\pi f})\right| \geq \left|H(e^{j2\pi f})\right| \geq \sqrt{1-4\mu(1-\mu)}\ \left|H_0(e^{j2\pi f})\right|, \quad \forall f \in [0,1). \tag{5.9}$$

Proof: From (5.5) we have

$$|H(z)| = |H_0(z)|\,|1+\mu(z^{-1}-1)|. \tag{5.10}$$

where

$$H_0(z) = \frac{z^{-\ell}-1}{\ell(z^{-1}-1)}. \tag{5.11}$$

Figure 5.8 shows a diagram in the complex plane where we can see the locations of the factor $1+\mu(e^{-j2\pi f}-1)$. Its magnitude can be computed as

$$\left|1+\mu(e^{-j2\pi f}-1)\right|^2 = 1-2\mu(1-\mu)[1-\cos(2\pi f)], \tag{5.12}$$

and hence

$$\sqrt{1-4\mu(1-\mu)} \leq \left|1+\mu(e^{-j2\pi f}-1)\right| \leq 1. \tag{5.13}$$

The substitution of (5.13) into (5.10) yields the desired result (5.9).

$\mathcal{Q}.\mathcal{E}.\mathcal{D}.$

Now we focus our attention to the cases in which ℓ is not integer. There is no closed form for the factors of the system function $H(z)$, but it can be defined as the sum of three terms.

Lemma 5.1.3 *The impulse responses $h[m]$ of the systems resulting from pixel light intensity profile $\phi(x) = b_\ell(x-\mu)$, $L = \lceil \ell+\mu \rceil - 1$, $\gamma = \ell - L$, and sampling function $\zeta(x) = b_1(x)$, have z-transform*

$$H(z) = \frac{1}{\ell}\left[(\gamma+\mu)\,z^{-L} - \mu + \frac{z^{-L}-1}{z^{-1}-1}\right]. \tag{5.14}$$

ℓ	Interval	$L_0 = \lceil \ell \rceil - 1$	$L = \lceil \ell + \mu \rceil - 1$	$\gamma_0 = \ell - L_0$	$\gamma = \ell - L$
2	$\mu = 0$	1	1	1	1
2	$\mu \in (0, 1)$	1	2	1	0
2.4	$\mu \in [0, 0.6]$	2	2	0.4	0.4
2.4	$\mu \in (0.6, 1)$	2	3	0.4	–0.6
3	$\mu = 0$	2	2	1	1
3	$\mu \in (0, 1)$	2	3	1	0
3.7	$\mu \in [0, 0.3]$	3	3	0.7	0.7
3.7	$\mu \in (0.3, 1)$	3	4	0.7	–0.3

Table 5.1: Examples of how parameters defined in Lemma 5.1.3 change with μ.

Proof: In this case, the application of (3.67) produces the sequence

$$h[m] = \frac{1}{\ell} \begin{cases} 1 - \mu, & m = 0, \\ 1, & m = 1, 2, \ldots, L - 1, \\ \gamma + \mu, & m = L, \\ 0, & \text{otherwise}, \end{cases} \tag{5.15}$$

Note that $\gamma + \mu$ is always a valid value for $h[L]$ because, from its definition, we have

$$\gamma + \mu = \ell + \mu + 1 - \lceil \ell + \mu \rceil \in [0, 1). \tag{5.16}$$

Thus, we have the system function defined by

$$\begin{aligned} \ell H(z) &= 1 - \mu + z^{-1} + z^{-2} + \cdots + z^{1-L} + (\gamma + \mu) z^{-L} \\ &= \gamma z^{-L} + \mu(z^{-L} - 1) + \sum_{n=0}^{L-1} z^{-n} \\ &= \gamma z^{-L} + \mu(z^{-L} - 1) + \frac{z^{-L} - 1}{z^{-1} - 1}. \end{aligned} \tag{5.17}$$

$\mathcal{Q}.\mathcal{E}.\mathcal{D}.$

The parameters L and γ are defined in such a way that $H(z)$ is conveniently defined by a single equation. However, when using (5.14) it is important to note that the number of zeros in $H(z)$ is equal to L, which changes with μ, and that the value of γ also changes when L changes. Table 5.1 shows some examples.

Figures 5.9 to 5.14 show the magnitude of the frequency response for some values of ℓ. They are similar to the cases when ℓ is integer, but we can see that now, for some values of μ, $H(z)$ has no zeros on the unit circle. This means that in those cases the inverse filter operation is well defined because $1/H(e^{j2\pi f})$ exists for all $f \in [0, 1)$.

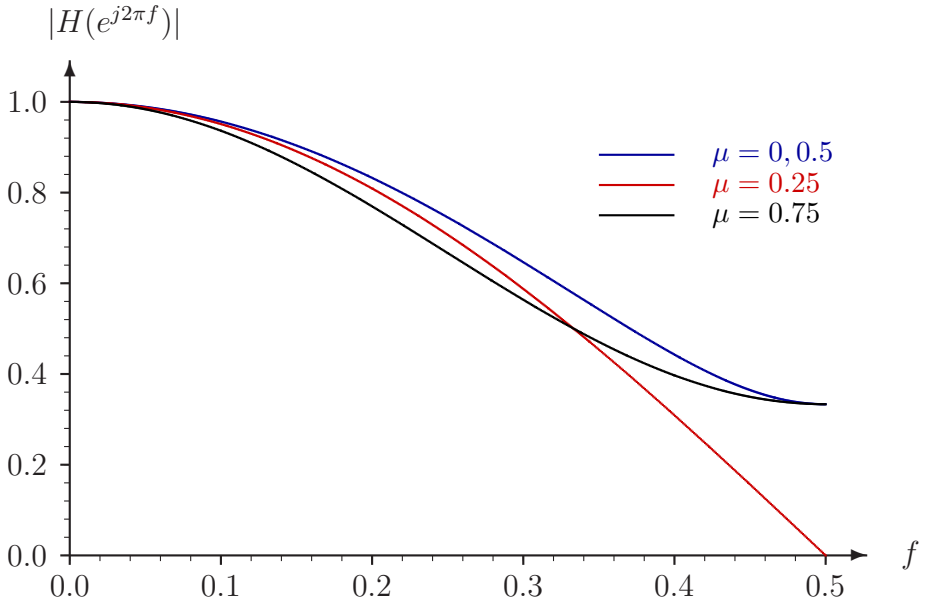

Figure 5.9: Frequency response of superimposition systems with sampling function $\zeta(x) = b_1(x)$ and PLIP $\phi(x) = b_{1.5}(x - \mu)$ $(\ell = 1.5)$.

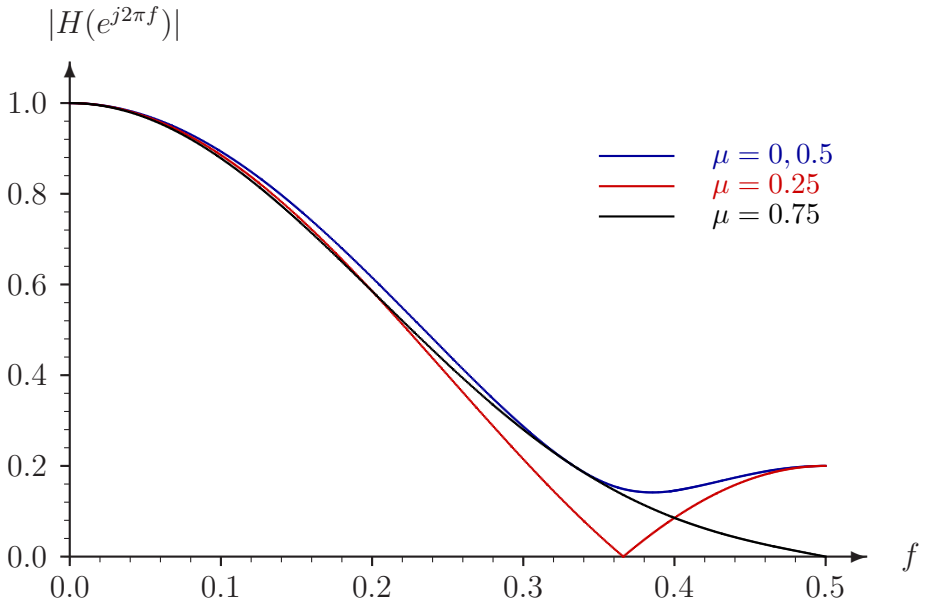

Figure 5.10: Frequency response of superimposition systems with sampling function $\zeta(x) = b_1(x)$ and PLIP $\phi(x) = b_{2.5}(x - \mu)$ $(\ell = 2.5)$.

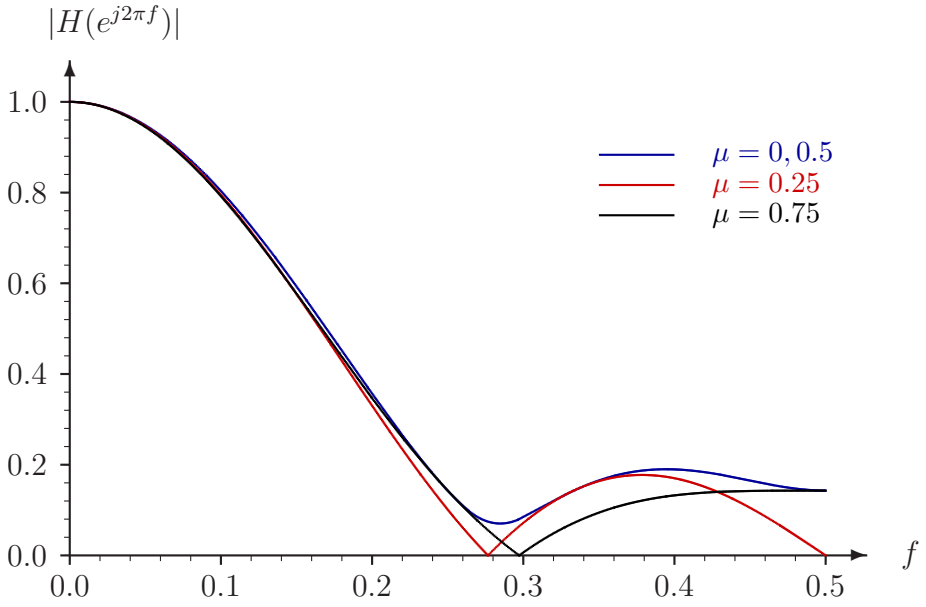

Figure 5.11: Frequency response of superimposition systems with sampling function $\zeta(x) = b_1(x)$ and PLIP $\phi(x) = b_{3.5}(x - \mu)$ $(\ell = 3.5)$.

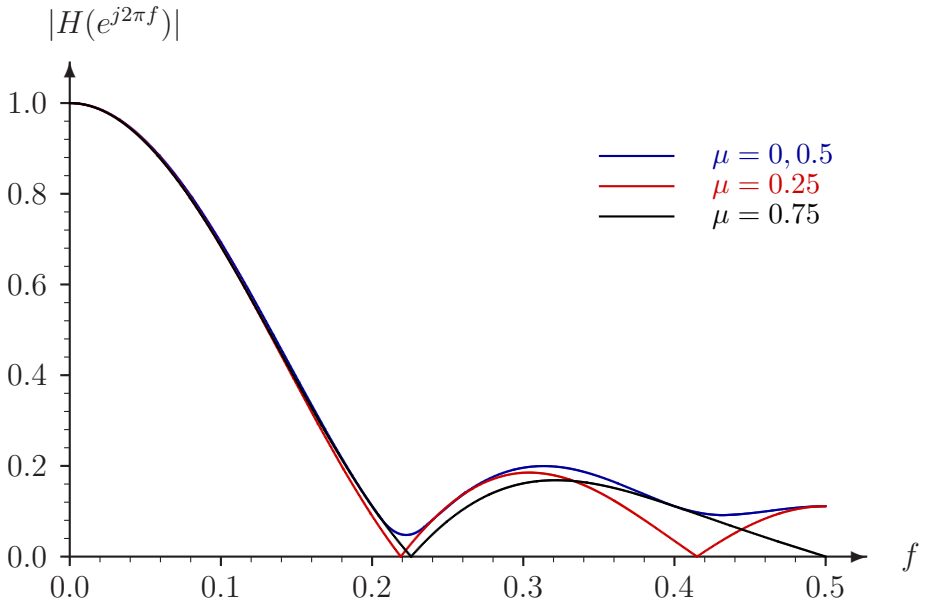

Figure 5.12: Frequency response of superimposition systems with sampling function $\zeta(x) = b_1(x)$ and PLIP $\phi(x) = b_{4.5}(x - \mu)$ $(\ell = 4.5)$.

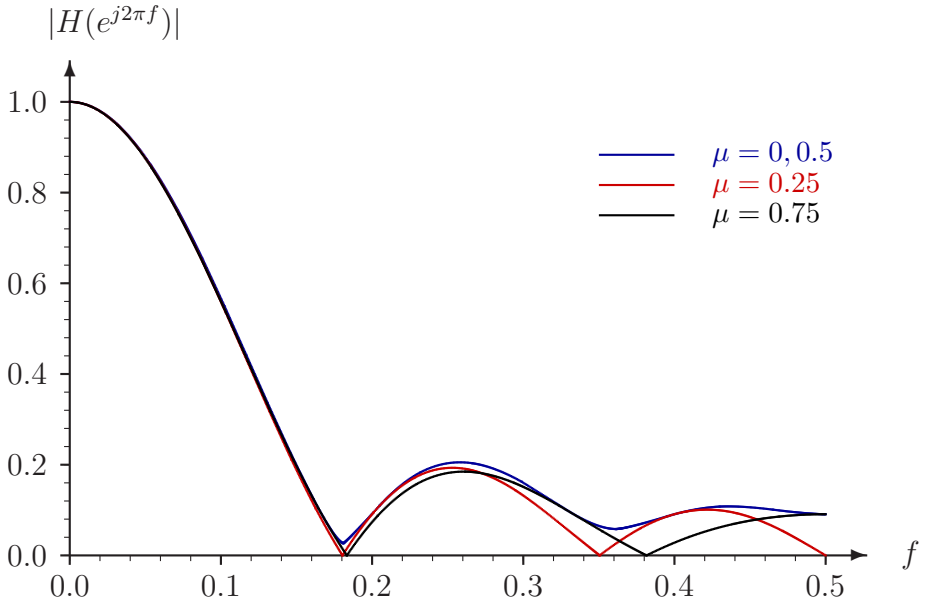

Figure 5.13: Frequency response of superimposition systems with sampling function $\zeta(x) = b_1(x)$ and PLIP $\phi(x) = b_{5.5}(x - \mu)$ ($\ell = 5.5$).

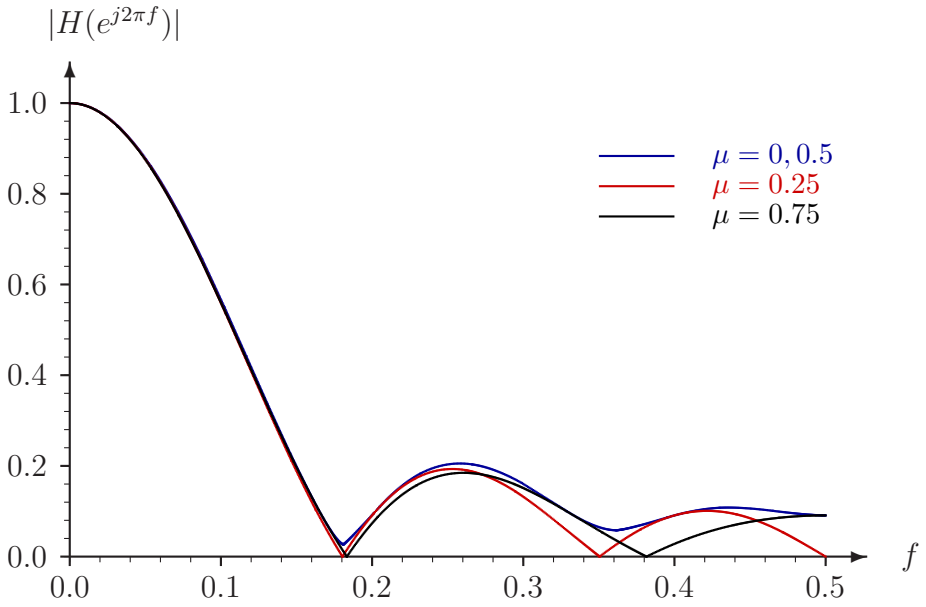

Figure 5.14: Frequency response of superimposition systems with sampling function $\zeta(x) = b_1(x)$ and PLIP $\phi(x) = b_{6.5}(x - \mu)$ ($\ell = 6.5$).

Theorem 5.1.2 shows that, when ℓ is an integer, using $\mu \in (0,1)$ can only decrease the magnitude of the Fourier transform $H(e^{j2\pi f})$. This is intuitive, since having $\mu \in (0,1)$ implies that there is an additional real-valued zero, which may increase attenuation in nonzero frequencies. Next we show a less intuitive result: in the general case (non-integer ℓ), having $\mu \in (0,1)$ does not necessarily add a new zero, but can only increase attenuation of nonzero frequencies.

Theorem 5.1.4 *Let $H_\mu(z)$ be the system functions obtained from pixel light intensity profile $\phi(x) = b_\ell(x-\mu)$, and sampling function $\zeta(x) = b_1(x)$, with $L = \lceil \ell + \mu \rceil - 1$, $\gamma = \ell - L$ (as used in Lemma 5.1.3). Defining $L_0 = \lceil \ell \rceil - 1$, $\gamma_0 = \ell - L_0$, and*

$$H_0(z) = \frac{\gamma_0 z^{-L_0}}{\ell} + \frac{z^{-L_0} - 1}{\ell(z^{-1} - 1)}. \tag{5.18}$$

The magnitudes of the corresponding Fourier transforms are such that

$$\left|H_0(e^{j2\pi f})\right|^2 - \left|H_\mu(e^{j2\pi f})\right|^2 = \frac{1}{\ell} \begin{cases} 2\mu(1-\gamma-\mu)[1-\cos(2\pi f L)], & L = L_0, \\ 2(1-\mu)(\gamma+\mu)[1-\cos(2\pi f L)], & L > L_0, \end{cases} \tag{5.19}$$

and consequently

$$\left|H_0(e^{j2\pi f})\right| \geq \left|H_\mu(e^{j2\pi f})\right|, \quad \forall\, f, \mu \in [0,1). \tag{5.20}$$

Proof: In this proof we use the following identity: for any two complex numbers u and v we have

$$|u|^2 - |v|^2 = 2\Re\left\{\bar{u}(u-v)\right\} - |u-v|^2. \tag{5.21}$$

Let us consider first the case $L = L_0$, which corresponds to $\mu \in [0, 1-\gamma_0]$. Using (5.14) and (5.18) we can compute the difference

$$H_0(z) - H_\mu(z) = \mu(1 - z^{-L}). \tag{5.22}$$

Defining

$$\Delta_\mu = \left|H_0(e^{j2\pi f})\right|^2 - \left|H_\mu(e^{j2\pi f})\right|^2, \tag{5.23}$$

we can use (5.21), with $u = H_0(e^{j2\pi f})$ and $v = H_\mu(e^{j2\pi f})$, to compute

$$\begin{aligned} \Delta_\mu &= 2\Re\left\{\bar{H}_0(e^{j2\pi f})\left[H_0(e^{j2\pi f}) - H_\mu(e^{j2\pi f})\right]\right\} - \left|H_0(e^{j2\pi f}) - H_\mu(e^{j2\pi f})\right|^2 \\ &= 2\mu\Re\left\{\left(\gamma e^{j2\pi f L} + \frac{e^{j2\pi f L} - 1}{e^{j2\pi f} - 1}\right)\left(1 - e^{-j2\pi f L}\right)\right\} - \mu^2\left|1 - e^{-j2\pi f L}\right|^2 \\ &= 2\mu(1-\gamma)[1-\cos(2\pi f L)] - 2\mu^2[1-\cos(2\pi f L)] \\ &= 2\mu(1-\gamma-\mu)[1-\cos(2\pi f L)]. \end{aligned} \tag{5.24}$$

We can also conclude that $\left|H_0(e^{j2\pi f})\right| \geq \left|H_\mu(e^{j2\pi f})\right|$ whenever $\gamma + \mu \leq 1$, which we know from (5.16) is always true.

The second case, when $L > L_0$, is different because there is an increase in the number of zeros in $H_\mu(z)$ (cf. Table 5.1). Unfortunately, the difference in the order of $H_\mu(z)$ and $H_0(z)$ complicates the derivation considerably. To avoid this problem, in the second part of the proof we use the fact that, if $H_1(z)$ is the system function corresponding to case $\mu = 1$, we have

$$H_1(z) = z^{-1}H_0(z) \quad \Longrightarrow \quad \left|H_1(e^{j2\pi f})\right| = \left|H_0(e^{j2\pi f})\right|, \tag{5.25}$$

because integer values of μ corresponds to only changes in the phase of $H(e^{j2\pi f})$.

Thus, when $L = L_0 + 1$ and $\mu \in [1 - \gamma_0, 1]$ we still can use (5.14) to compute

$$H_1(z) = (\gamma + 1)z^{-L} - 1 + \frac{z^{-L} - 1}{z^{-1} - 1}, \tag{5.26}$$

and

$$H_1(z) - H_\mu(z) = (1 - \mu)(z^{-L} - 1). \tag{5.27}$$

Now we can combine these results using

$$\Delta_\mu = \left|H_0(e^{j2\pi f})\right|^2 - \left|H_\mu(e^{j2\pi f})\right|^2 = \left|H_1(e^{j2\pi f})\right|^2 - \left|H_\mu(e^{j2\pi f})\right|^2, \tag{5.28}$$

and, similarly to the first case, compute

$$\begin{aligned}
\Delta_\mu &= 2\Re\left\{\bar{H}_1(e^{j2\pi f})\left[H_1(e^{j2\pi f}) - H_\mu(e^{j2\pi f})\right]\right\} - \left|H_1(e^{j2\pi f}) - H_\mu(e^{j2\pi f})\right|^2 \\
&= 2(1-\mu)\Re\left\{\left((\gamma+1)e^{j2\pi fL} - 1 + \frac{e^{j2\pi fL} - 1}{e^{j2\pi f} - 1}\right)\left(e^{-j2\pi fL} - 1\right)\right\} - \\
&\quad -(1-\mu)^2\left|1 - e^{-j2\pi fL}\right|^2 \\
&= 2(1-\mu)(1+\gamma)[1 - \cos(2\pi fL)] - 2(1-\mu)^2[1 - \cos(2\pi fL)] \\
&= 2(1-\mu)(\gamma+\mu)[1 - \cos(2\pi fL)].
\end{aligned} \tag{5.29}$$

In this case we also conclude that $\left|H_0(e^{j2\pi f})\right| \geq \left|H_\mu(e^{j2\pi f})\right|$ because we always have $\mu \leq 1$ and $\gamma + \mu \geq 0$.

$\mathcal{Q.E.D.}$

This result is quite important because it lets us "close the case" on the need to shift the sampling function using $\mu \neq 0$, when looking for better results. Since having more attenuation on the high frequencies produces more difficult inverse filtering problems, we should focus our attention to the system functions defined by the cases when $\mu = 0$.

Figures 5.15 to 5.17 show some sets of frequency responses resulting from pixel light intensity profile (PLIP) $b_\ell(x)$ ($\mu = 0$), and Table 5.2 shows the sets of zeros of the corresponding system functions $H(z)$.

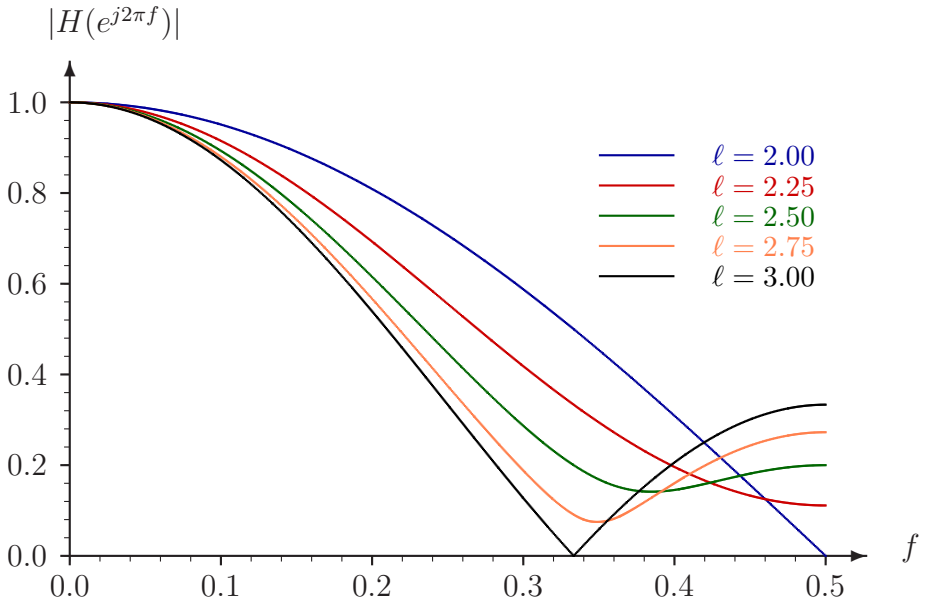

Figure 5.15: Frequency response of linear-phase systems with sampling function $\zeta(x) = b_1(x)$ and PLIP $\phi(x) = b_\ell(x)$ $(\mu = 0)$, for some values of ℓ between 2 and 3.

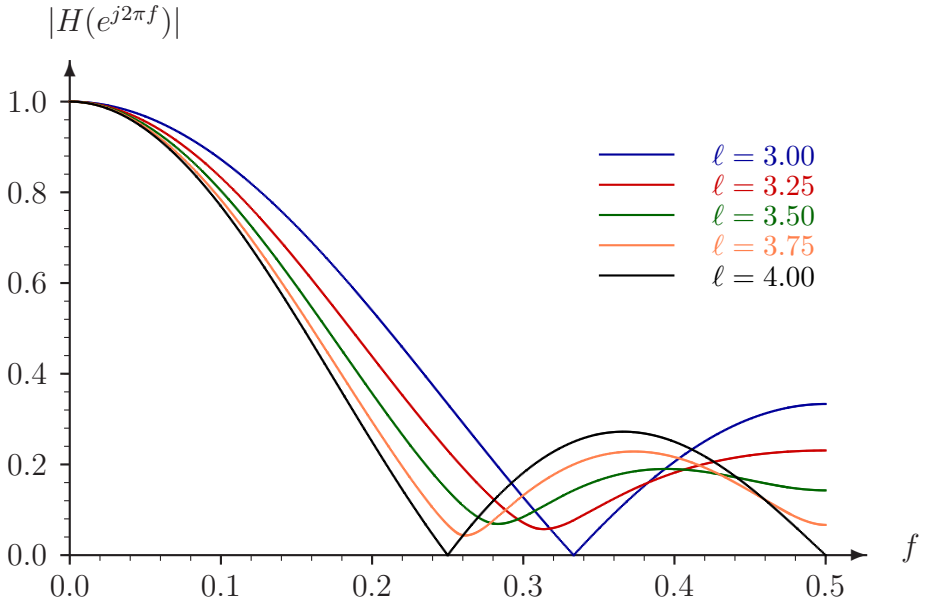

Figure 5.16: Frequency response of linear-phase systems with sampling function $\zeta(x) = b_1(x)$ and PLIP $\phi(x) = b_\ell(x)$ $(\mu = 0)$, for some values of ℓ between 3 and 4.

ℓ	Zeros of $H(z)$		
2.0	–1		
2.1	–0.887	–0.113	
2.2	–0.724	–0.276	
2.3	(0.548, ±155.9°)		
2.4	(0.632, ±142.2°)		
2.5	(0.707, ±135.0°)		
2.6	(0.775, ±130.2°)		
2.7	(0.837, ±126.7°)		
2.8	(0.894, ±124.0°)		
2.9	(0.949, ±121.8°)		
3.0	(1, ±120°)		
3.1	(0.949, ±117.9°)	–0.111	
3.2	(0.903, ±114.7°)	–0.245	
3.3	(0.872, ±110.3°)	–0.394	
3.4	(0.867, ±105.6°)	–0.533	
3.5	(0.879, ±101.6°)	–0.648	
3.6	(0.899, ±98.2°)	–0.742	
3.7	(0.924, ±95.6°)	–0.821	
3.8	(0.949, ±93.4°)	–0.888	
3.9	(0.975, ±91.5°)	–0.947	
4.0	(1, ±90°)	–1	
4.1	(0.976, ±88.4°)	–0.944	–0.111
4.2	(0.957, ±86.4°)	–0.869	–0.251
4.3	(0.945, ±84.2°)	–0.735	–0.457
4.4	(0.941, ±81.9°)	(0.672, ±160.3°)	
4.5	(0.943, ±79.7°)	(0.750, ±153.1°)	
4.6	(0.950, ±77.7°)	(0.815, ±149.5°)	
4.7	(0.961, ±76.0°)	(0.871, ±147.3°)	
4.8	(0.973, ±74.5°)	(0.919, ±145.8°)	
4.9	(0.986, ±73.2°)	(0.962, ±144.8°)	
5.0	(1, ±72°)	(1, ±144°)	
5.1	(0.987, ±70.8°)	(0.961, ±143.1°)	–0.111
5.2	(0.977, ±69.5°)	(0.916, ±141.6°)	–0.250
5.3	(0.971, ±68.1°)	(0.870, ±138.5°)	–0.421
5.4	(0.969, ±66.7°)	(0.847, ±133.7°)	–0.594
5.5	(0.969, ±65.4°)	(0.860, ±129.3°)	–0.720
5.6	(0.972, ±64.1°)	(0.886, ±126.0°)	–0.807
5.7	(0.978, ±62.9°)	(0.917, ±123.8°)	–0.872
5.8	(0.984, ±61.8°)	(0.946, ±122.2°)	–0.922
5.9	(0.992, ±60.9°)	(0.974, ±120.9°)	–0.964
6.0	(1, ±60°)	(1, ±120°)	–1

Table 5.2: Sets of zeros of the system functions $H(z)$ corresponding to $\zeta(x) = b_1(x)$, $\phi(x) = b_\ell(x)$ ($\mu = 0$). Complex pairs are shown in polar notation.

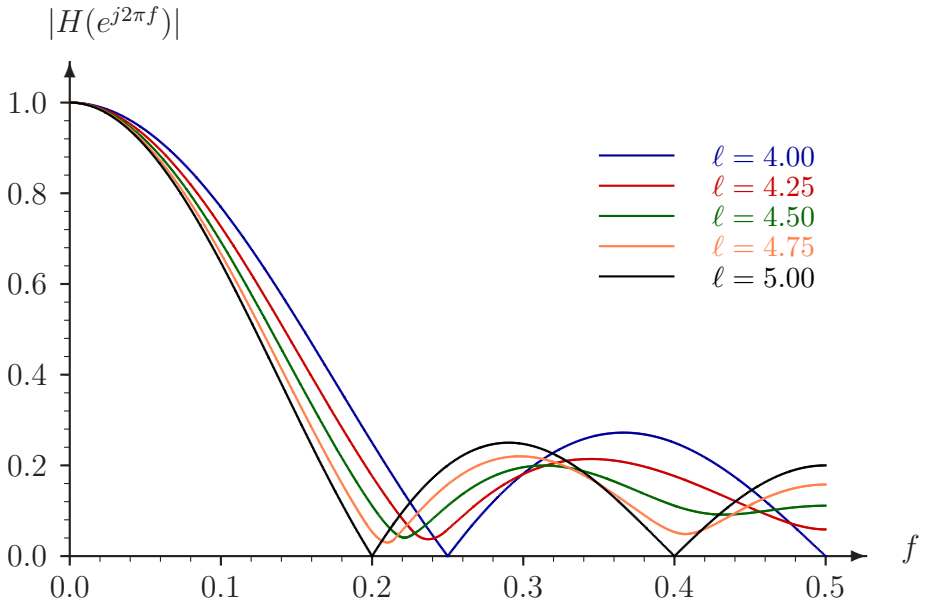

Figure 5.17: Frequency response of linear-phase systems with sampling function $\zeta(x) = b_1(x)$ and PLIP $\phi(x) = b_\ell(x)$ $(\mu = 0)$, for some values of ℓ between 4 and 5.

Theorem 5.1.5 *The inverse of the system functions $H_0(z)$ obtained from pixel light intensity profile $\phi(x) = b_\ell(x)$ $(\mu = 0)$, and sampling function $\zeta(x) = b_1(x)$ always exist when $\ell \neq \lfloor \ell \rfloor$, because in those cases*

$$H_0(e^{j2\pi f}) \neq 0, \quad \forall f \in [0, 1). \tag{5.30}$$

Proof: Defining $L_0 = \lceil \ell \rceil - 1$ and $\gamma_0 = \ell - L$, we assume that $\gamma_0 \neq 0$. Let us consider the system function $H_\mu(z)$ defined by the pixel profile $\phi'(x) = b_\ell(x - \mu)$, where $\mu = (1 - \gamma_0)/2$.

We can use the bound (5.19) of Theorem 5.1.4, and since $\left|H_\mu(e^{j2\pi f})\right| \geq 0$ we have

$$\left|H_0(e^{j2\pi f})\right|^2 \geq \frac{1}{2}(1 - \gamma_0^2)[1 - \cos(2\pi f L)], \quad \forall f \in [0, 1). \tag{5.31}$$

Since $1 - \gamma_0^2 < 1$ we conclude that

$$\left|H_0(e^{j2\pi f})\right|^2 > 0, \quad \forall f \in [0, 1) - \bigcup_{k=0}^{L-1} \{k/L\}. \tag{5.32}$$

The remaining cases, $f = 0, 1/L, \ldots, 1/(L-1)$, correspond to another bound derived from (5.19):

$$\left|H_0(e^{j2\pi k/L})\right|^2 \geq \left|H_\mu(e^{j2\pi k/L})\right|^2. \tag{5.33}$$

Considering that the substitution of $z = e^{j2\pi k/L}$ in equation (5.14) (Lemma 5.1.3) results in

$$\left|H_\mu(e^{j2\pi k/L})\right|^2 = \gamma > 0, \quad k = 0, 1, 2, \ldots, L-1, \tag{5.34}$$

we conclude that

$$\left|H_0(e^{j2\pi f})\right|^2 > 0, \quad \forall f \in [0, 1), \tag{5.35}$$

which is equivalent to the desired result.

$\mathcal{Q.E.D.}$

While the best response is obtained with minimum-phase filters, in imaging applications it is preferable to use linear-phase filters. Unfortunately, the linear-phase filters defined when the PLIP and sampling functions are box functions are not invertible.

Theorem 5.1.6 *Let $H(z)$ be the system functions obtained from pixel light intensity profile $\phi(x) = b_\ell(x - \mu)$, and sampling function $\zeta(x) = b_1(x)$, with $L = \lceil \ell + \mu \rceil - 1$, $\gamma = \ell - L$ (as used in Lemma 5.1.3). Defining $L_0 = \lceil \ell \rceil - 1$, $\gamma_0 = \ell - L_0$, $H(z)$ corresponds to a linear-phase filter when*

$$\mu = \begin{cases} (1 - \gamma_0)/2, & L = L_0, \\ 1 - \gamma_0/2, & L = L_0 + 1, \end{cases} \tag{5.36}$$

The corresponding system function is defined by

$$H(z) = \frac{(1-\mu)z^{-L-1} + \mu z^{-L} - \mu z^{-1} - 1 + \mu}{\ell(z^{-1} - 1)}. \tag{5.37}$$

This system function has all L_0 zeros on the unit circle when $\mu = (1 - \gamma_0)/2$, and when $\mu = 1 - \gamma_0/2$ it has at least $L - 2$ zeros on the unit circle, and at most two real zeros outside the unit-circle.

Proof: From (5.15) we can see that we obtain the symmetric impulse response $h[m]$ required for a linear-phase filter when

$$1 - \mu = \gamma + \mu. \tag{5.38}$$

When $L = L_0$ we have $\gamma = \gamma_0$, and consequently we have a linear-phase filter when $\mu = (1 - \gamma_0)/2$. Similarly, when $L = L_0 + 1$ we have $\gamma = \gamma_0 - 1$ and the linear-phase symmetry occurs when $\mu = 1 - \gamma_0/2$.

A real-valued Fourier transform can be obtained with the proper phase shift to the Fourier transform of a linear-phase impulse response. In our case we can define

$$H_\Re(z) \doteq -\frac{(z^{-1} - 1)z^{(L+1)/2}}{2} H(z) \tag{5.39}$$

$$= (1 - \mu)\left[z^{(L+1)/2} - z^{-(L+1)/2}\right] + \mu\left[z^{(L-1)/2} - z^{-(L-1)/2}\right] \tag{5.40}$$

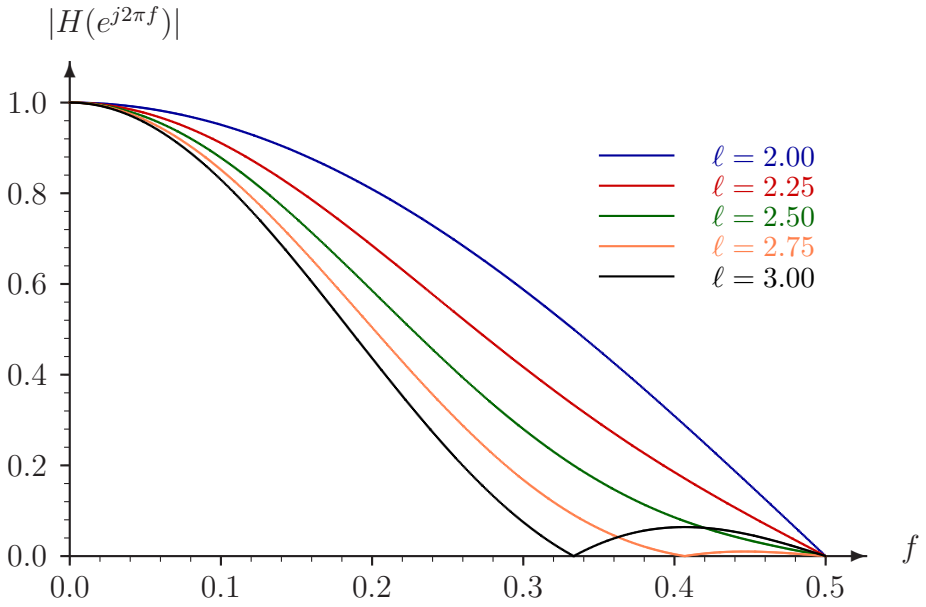

Figure 5.18: Frequency response of linear-phase systems with sampling function $\zeta(x) = b_1(x)$ and PLIP $\phi(x) = b_\ell(x - \mu)$, $\mu = (1 - \gamma_0)/2$, for some values of ℓ between 2 and 3.

and obtain

$$H_{\Re}(\alpha e^{j2\pi}) = \alpha \left\{ (1-\mu) \sin(\pi f[L+1]) + \mu \sin(\pi f[L-1]) \right\}. \tag{5.41}$$

Note that all the zeros of $H_{\Re}(e^{j2\pi f})$ for $f \neq 0$ correspond to zeros in $H(e^{j2\pi f})$, and thus correspond to zeros of $H(z)$ that are located on the unit circle. We have a trivial zero at $f = 0$, i.e., $H_{\Re}(1) = 0$, because $H(z)$ was multiplied by $(z^{-1} - 1)$ to simplify the closed form of $H_{\Re}(z)$.

We can analyze the zeros of (5.41) considering the fact that $\sin(\pi f[L+1]) = \sin(\pi f[L-1])$ when $2Lf = 0, 1, 3, 5, \ldots, 2L-1$. The values of these functions at these points are

$$2 \sin(\pi[n+1/2]) \cos(\pi[n+1/2]/L), \quad , n = 1, 3, \ldots, 2L-1. \tag{5.42}$$

We can observe that in the interval $f \in [0, 1]$ we have $L - 2$ adjacent pairs of these values with alternate signs, independently the value of μ or α. Since the function is continuous, this means that we have $L - 2$ zeros in the unit circle.

Considering that the z-transform of linear-phase filters can only have pairs of complex zeros on the unit circle, or groups of pairs of complex conjugate zeros such that if z_0 is a zero then $1/z_0$ is also a zero, we conclude that the remaining two zeros can only be either a conjugate pair on the unit circle or in the real line.

$\mathcal{Q}.\mathcal{E}.\mathcal{D}.$

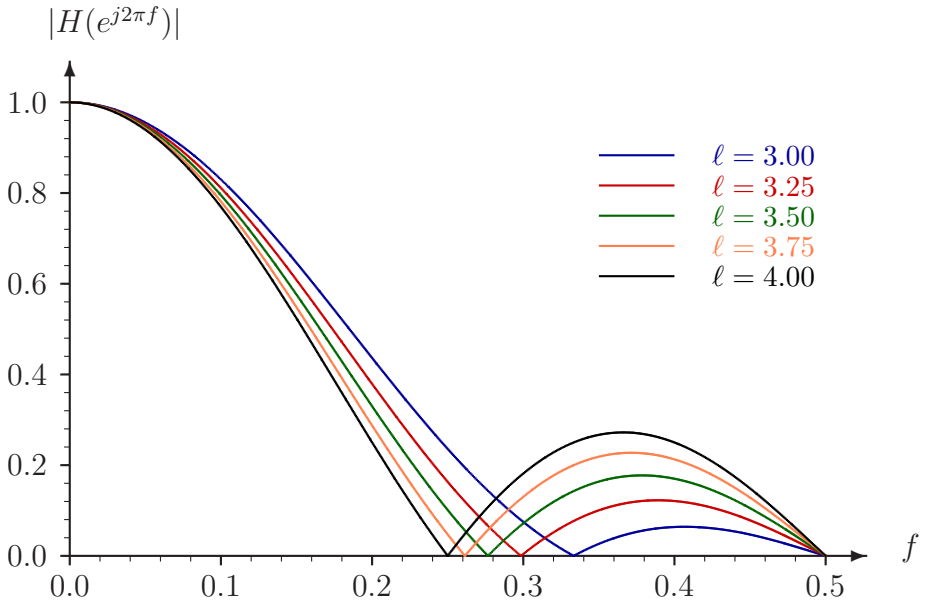

Figure 5.19: Frequency response of linear-phase systems with sampling function $\zeta(x) = b_1(x)$ and PLIP $\phi(x) = b_\ell(x - \mu)$, $\mu = (1 - \gamma_0)/2$, for some values of ℓ between 3 and 4.

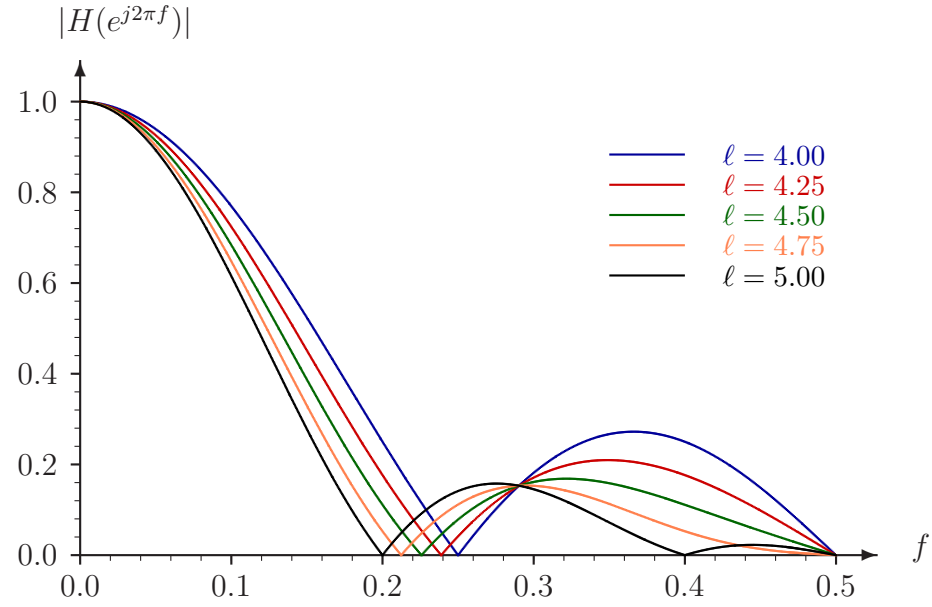

Figure 5.20: Frequency response of linear-phase systems with sampling function $\zeta(x) = b_1(x)$ and PLIP $\phi(x) = b_\ell(x - \mu)$, $\mu = (1 - \gamma_0)/2$, for some values of ℓ between 4 and 5.

ℓ	Zeros of $H(z)$		
2.0	–1		
2.1	(1, ±155.4°)		
2.2	(1, ±146.4°)		
2.3	(1, ±140.3°)		
2.4	(1, ±135.6°)		
2.5	(1, ±131.8°)		
2.6	(1, ±128.7°)		
2.7	(1, ±126.0°)		
2.8	(1, ±123.7°)		
2.9	(1, ±121.8°)		
3.0	(1, ±120°)		
3.1	(1, ±114.1°)	–1	
3.2	(1, ±109.5°)	–1	
3.3	(1, ±105.6°)	–1	
3.4	(1, ±102.4°)	–1	
3.5	(1, ±99.6°)	–1	
3.6	(1, ±97.2°)	–1	
3.7	(1, ±95.1°)	–1	
3.8	(1, ±93.2°)	–1	
3.9	(1, ±91.5°)	–1	
4.0	(1, ±90°)	–1	
4.1	(1, ±87.3°)	(1, ±163.1°)	
4.2	(1, ±84.8°)	(1, ±157.5°)	
4.3	(1, ±82.6°)	(1, ±153.9°)	
4.4	(1, ±80.6°)	(1, ±151.3°)	
4.5	(1, ±78.8°)	(1, ±149.4°)	
4.6	(1, ±77.2°)	(1, ±147.8°)	
4.7	(1, ±75.7°)	(1, ±146.6°)	
4.8	(1, ±74.4°)	(1, ±145.6°)	
4.9	(1, ±73.1°)	(1, ±144.7°)	
5.0	(1, ±72°)	(1, ±144°)	
5.1	(1, ±70.4°)	(1, ±138.1°)	–1
5.2	(1, ±68.9°)	(1, ±133.9°)	–1
5.3	(1, ±67.5°)	(1, ±130.7°)	–1
5.4	(1, ±66.2°)	(1, ±128.2°)	–1
5.5	(1, ±64.9°)	(1, ±126.2°)	–1
5.6	(1, ±63.8°)	(1, ±124.5°)	–1
5.7	(1, ±62.8°)	(1, ±123.1°)	–1
5.8	(1, ±61.8°)	(1, ±121.9°)	–1
5.9	(1, ±60.9°)	(1, ±120.9°)	–1
6.0	(1, ±60°)	(1, ±120°)	–1

Table 5.3: Sets of zeros of the linear-phase system functions $H(z)$ corresponding to $\zeta(x) = b_1(x)$, $\phi(x) = b_\ell(x - \mu)$ ($\mu \neq 0$). Complex pairs are shown in polar notation.

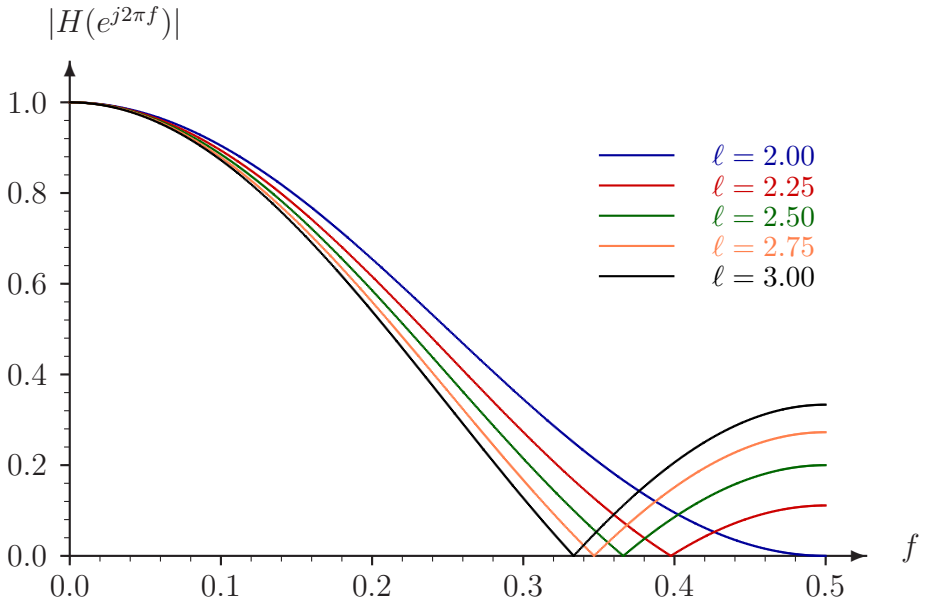

Figure 5.21: Frequency response of linear-phase systems with sampling function $\zeta(x) = b_1(x)$ and PLIP $\phi(x) = b_\ell(x - \mu)$, $\mu = 1 - \gamma_0/2$, for some values of ℓ between 2 and 3.

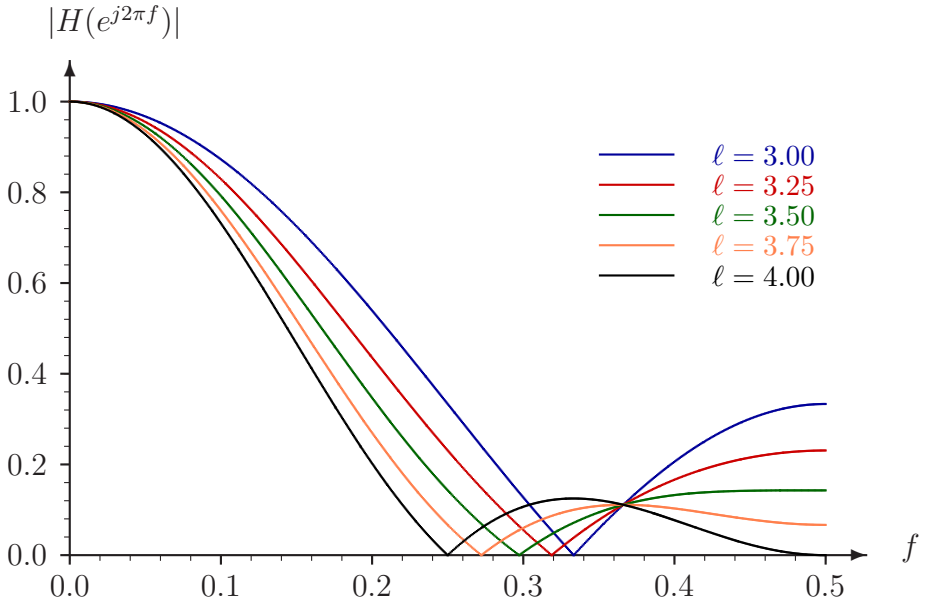

Figure 5.22: Frequency response of linear-phase systems with sampling function $\zeta(x) = b_1(x)$ and PLIP $\phi(x) = b_\ell(x - \mu)$, $\mu = 1 - \gamma_0/2$, for some values of ℓ between 3 and 4.

ℓ	Zeros of $H(z)$			
2.0	–1	–1		
2.1	–1	–18.94	–0.053	
2.2	–1	–8.887	–0.113	
2.3	–1	–5.484	–0.182	
2.4	–1	–3.732	–0.268	
2.5	–1	–2.618	–0.382	
2.6	–1	–1.768	–0.566	
2.7	(1, ±158.2°)	–1		
2.8	(1, ±138.6°)	–1		
2.9	(1, ±127.7°)	–1		
3.0	(1, ±120°)	–1		
3.1	(1, ±118.2°)	–19.003	–0.053	
3.2	(1, ±116.0°)	–9.012	–0.111	
3.3	(1, ±113.4°)	–5.696	–0.176	
3.4	(1, ±110.4°)	–4.056	–0.247	
3.5	(1, ±107.0°)	–3.091	–0.324	
3.6	(1, ±103.4°)	–2.462	–0.406	
3.7	(1, ±99.8°)	–2.022	–0.495	
3.8	(1, ±96.3°)	–1.689	–0.592	
3.9	(1, ±93.0°)	–1.406	–0.711	
4.0	(1, ±90°)	–1	–1	
4.1	(1, ±88.5°)	–1	–19.00	–0.053
4.2	(1, ±86.9°)	–1	–8.999	–0.111
4.3	(1, ±85.1°)	–1	–5.661	–0.177
4.4	(1, ±83.2°)	–1	–3.985	–0.251
4.5	(1, ±81.3°)	–1	–2.966	–0.337
4.6	(1, ±79.3°)	–1	–2.261	–0.442
4.7	(1, ±77.4°)	–1	–1.708	–0.586
4.8	(1, ±75.5°)	–1	–1	–1
4.9	(1, ±73.7°)	(1, ±153.1°)	–1	
5.0	(1, ±72°)	(1, ±144°)	–1	
5.1	(1, ±70.9°)	(1, ±143.2°)	–19.00	–0.053
5.2	(1, ±69.7°)	(1, ±142.3°)	–9.000	–0.111
5.3	(1, ±68.5°)	(1, ±141.1°)	–5.668	–0.176
5.4	(1, ±67.3°)	(1, ±139.5°)	–4.004	–0.250
5.5	(1, ±66.0°)	(1, ±137.3°)	–3.011	–0.332
5.6	(1, ±64.7°)	(1, ±134.6°)	–2.359	–0.424
5.7	(1, ±63.5°)	(1, ±131.1°)	–1.910	–0.524
5.8	(1, ±62.3°)	(1, ±127.3°)	–1.587	–0.630
5.9	(1, ±61.1°)	(1, ±123.5°)	–1.334	–0.750
6.0	(1, ±60°)	(1, ±120°)	–1	–1

Table 5.4: Sets of zeros of the linear-phase system functions $H(z)$ corresponding to $\zeta(x) = b_1(x)$, $\phi(x) = b_\ell(x - mu)$ ($\mu \neq 0$). Complex pairs are shown in polar notation.

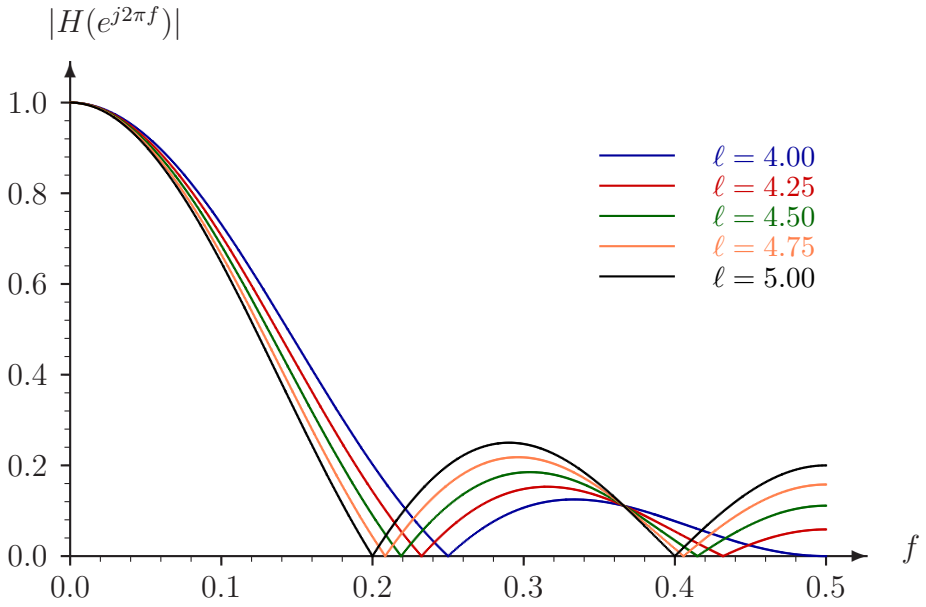

Figure 5.23: Frequency response of linear-phase systems with sampling function $\zeta(x) = b_1(x)$ and PLIP $\phi(x) = b_\ell(x - \mu)$, $\mu = 1 - \gamma_0/2$, for some values of ℓ between 4 and 5.

5.2 Extension for Antialiased Subframes

The results presented in Section 5.1 are derived under the assumption that the pixel light intensity profile $\phi(x)$ is the discontinue function $b_\ell(x)$, while as discussed in Section 2.3, normally projectors have anti-aliasing optical filters, and in those cases a better model is given by $b_{\ell,\sigma}(x)$. Even though this general case is somewhat more complicated, in this section we explain how the intuition provided by the results of Section 5.1 can be used for understanding other situations.

One fundamental result is independent of the value of σ: if ℓ is integer again the inverse systems do not exist, since we must have zeros in the Fourier transform.

Theorem 5.2.1 *Let $H(e^{j2\pi f})$ be the Fourier transform of the systems resulting from pixel light intensity profiles $\phi(x) = b_{\ell,\sigma}(x - \mu)$, $\ell = 1, 2, \ldots$, $\mu \in [0, 1]$, and sampling function $\zeta(x) = b_1(x)$. For all $\sigma \geq 0$ we have*

$$H(e^{j2\pi k/\ell}) = 0, \quad k = 1, 2, \ldots, \ell - 1. \tag{5.43}$$

Proof: Using the definitions of Section 2.3, we can observe in (2.17) that the Fourier transform of $b_{\ell,\sigma}(x)$ is such that for any $\sigma \geq 0$ we have

$$B_{\ell,\sigma}(f) = B_{1,\sigma}(\ell f), \tag{5.44}$$

and

$$B_{1,\sigma}(|k|) = 0, \quad k = 1, 2, \ldots \tag{5.45}$$

Using formula (3.70), derived in Section 3.3.1 for the Fourier transform of critically sampled systems, we have

$$H(e^{j2\pi f}) = \sum_{n=-\infty}^{\infty} \Phi(f-n)Z(f-n) = \sum_{n=-\infty}^{\infty} B_{1,\sigma}(\ell[f-n])B_{1,0}(f-n) \tag{5.46}$$

and thus

$$H(e^{j2\pi k/\ell}) = \sum_{n=-\infty}^{\infty} B_{1,\sigma}(k-\ell n)B_{1,0}(k/\ell - n). \tag{5.47}$$

The theorem's result follows from (5.45) and the fact that $k-\ell n$ is always an integer, and is zero only if k is a multiple of ℓ.

$\mathcal{Q.E.D.}$

The analysis of the systems defined by $b_{\ell,\sigma}(x)$ is somewhat less interesting because the fast decay in the magnitude of $B_{\ell,\sigma}(f)$—meant to reduce aliasing in the original projector resolution–can reduce dramatically all the components that can be used for improving quality via superimposition. For instance, we can observe in Figure 2.3 that even for small values of σ (e.g., $\sigma > 0.1$) we have

$$B_{1,\sigma}(f) \approx 0, \quad \forall |f| > 1 \quad \Longrightarrow \quad B_{\ell,\sigma}(f) \approx 0, \quad \forall |f| > 1/\ell. \tag{5.48}$$

Consequently, when $\ell \geq 2$ we have the Fourier transform of the sampled system satisfying

$$H(e^{j2\pi f}) = \sum_{n=-\infty}^{\infty} B_{\ell,\sigma}(f-n)B_{1,0}(f-n) \approx \begin{cases} B_{l\sigma}(f)B_{1,0}(f), & |f| < 1/\ell, \\ 0, & \text{otherwise.} \end{cases} \tag{5.49}$$

The conclusion is that anti-aliasing filters greatly reduce the possibility of increasing resolution and image quality using superimposition, because the inverse filter must have very large response not only in a few points, but in a whole interval of high frequencies.

5.3 Inverse Filter Approximation

Figures 5.24 and 5.25 show examples of the normalized response of the inverse filter

$$I(e^{j2\pi f}) \doteq \frac{\left|H(e^{j2\pi f})\right|}{|H(1)|\left(w + |H(e^{j2\pi f})|^2\right)}, \tag{5.50}$$

when using box PLIP, $w = 0.01$ and $w = 0.05$. Figures 5.26 and 5.27 show the corresponding overall response

$$G(e^{j2\pi f}) \doteq \frac{\left|H(e^{j2\pi f})\right|^2}{|H(1)|^2\left(w + |H(e^{j2\pi f})|^2\right)}. \tag{5.51}$$

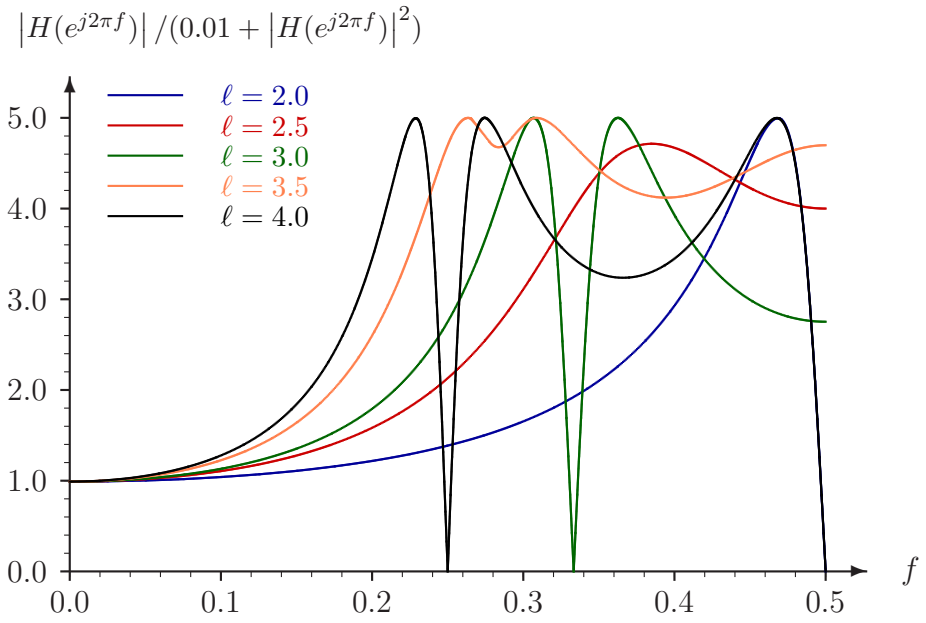

Figure 5.24: Frequency response of approximated inverse filter with PLIP $\phi(x) = b_\ell(x)$, $w = 0.01$.

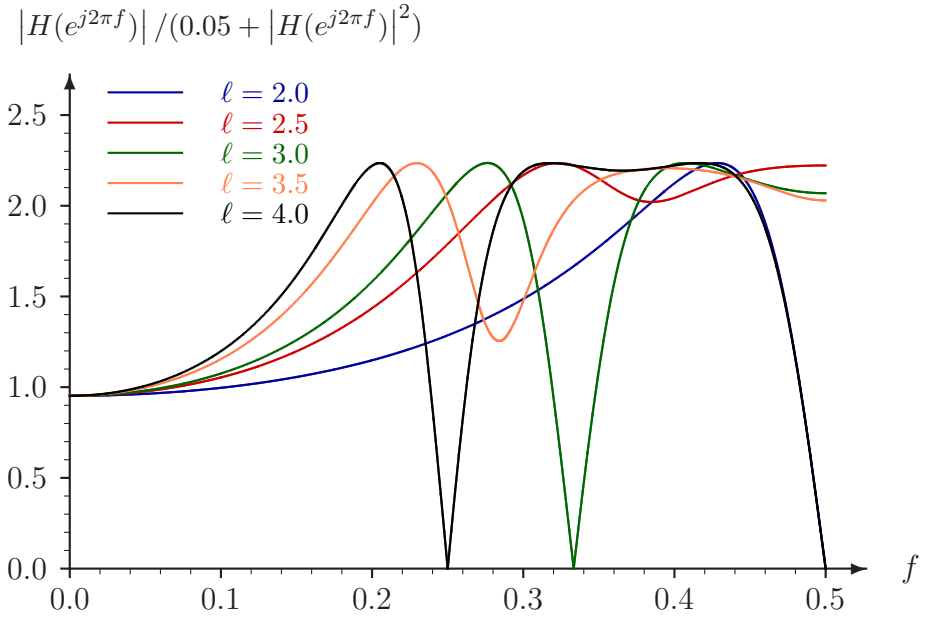

Figure 5.25: Frequency response of approximated inverse filter with PLIP $\phi(x) = b_\ell(x)$, $w = 0.05$.

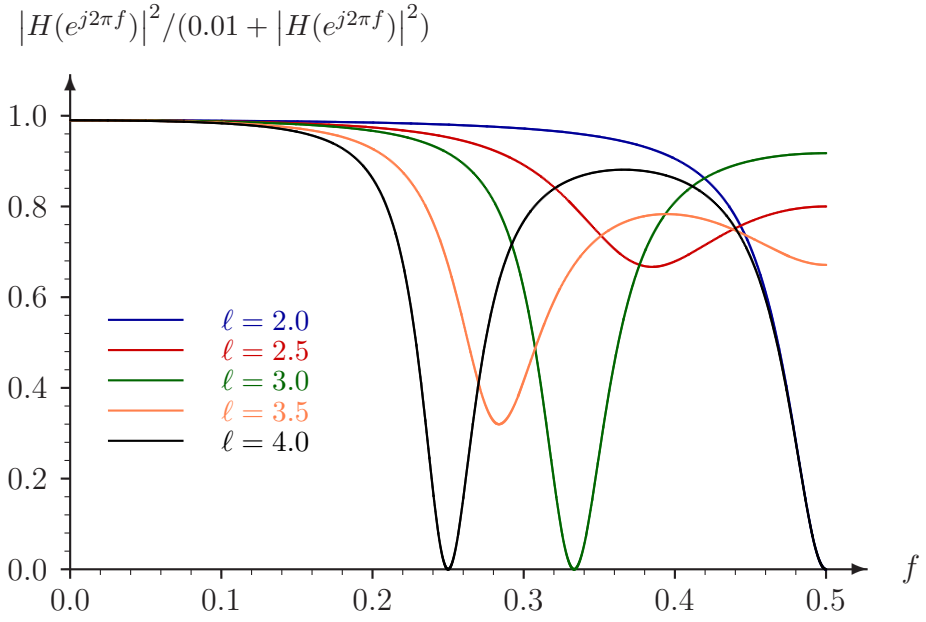

Figure 5.26: Overall frequency response of systems with PLIP $\phi(x) = b_\ell(x)$, after approximated inverse filter using weight $w = 0.01$.

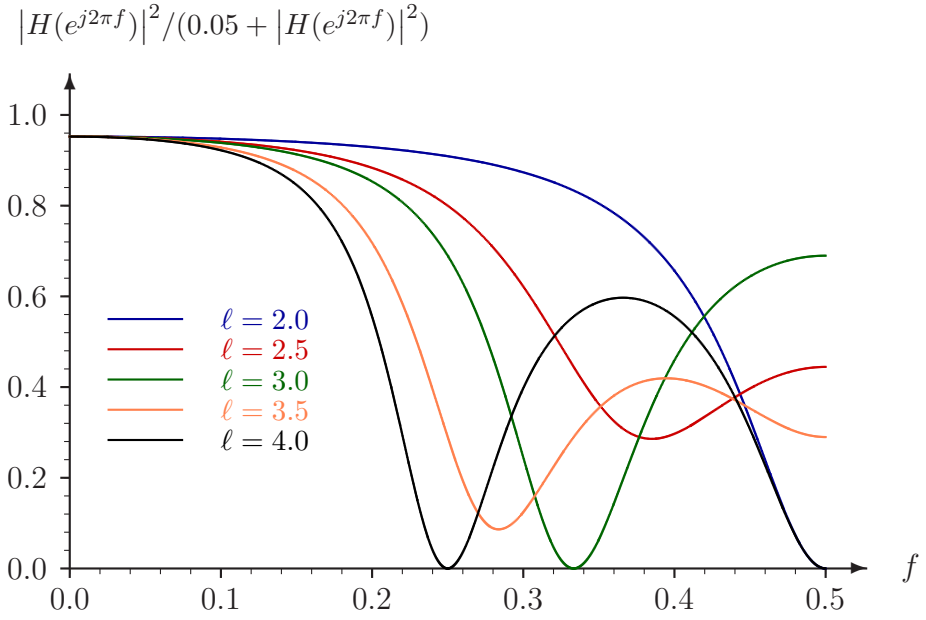

Figure 5.27: Overall frequency response of systems with PLIP $\phi(x) = b_\ell(x)$, after approximated inverse filter using weight $w = 0.05$.

Note that while (4.4) provides a good pseudo-inverse for the post-filtering cases (Figure 4.3), the solution of Theorem 4.2.1 is more convenient for the pre-filtering cases (Figure 4.2) because the frequency responses go to zero to avoid "wasting energy" in components that cannot be reproduced anyway.

Chapter 6

Linear System Experiments

6.1 Numerical Tests of the Linear Systems

While theoretically the two-dimensional separable systems are not very interesting, they are are important in practice, and they provide a good way visualize the theoretical developments for the one-dimensional case.

For instance, observing the frequency response in Figure 5.9, we can assume that for small values of ℓ the inverse filter $1/H(e^{j2\pi f})$ is not too ill-conditioned. Since images naturally have low high-frequency content, we can wonder how much overflow and underflow occur if we try the exact inverse filter.

We use the two large high-quality color images shown in Figure 6.1 in our tests. Figures 6.2 to 6.4 show the results for $\ell = 1.2$, 1.4, and 1.8. Overflow is indicated by setting the color component to its maximum value, and overflow by setting it to its minimum. Gray values indicate pixels where $c[m, n] \in [0, 1]$.

Note that even for $\ell = 1.2$, and for the relatively smooth image 'fruits' the number of pixels outside range is not insignificant, at least in the sense that they cannot be simply ignored. Even though the inverse filter exist when $\ell = 1.8$, its application produces images with so many violations of the projector constraints that it is of no practical value.

The next question is whether the approximations defined by (4.6) and (4.13) can remedy the problem. Tables 6.1 show the percentage of pixels with overflow or underflow after the application of this type of filters.

(a) Test image "Fruits" (2560×2048)

(b) Test image "Bike" (2048×2560)

Figure 6.1: The two color images used for testing the superimposition methods.

Figure 6.2: Visual representation of luminance underflow and overflow when the exact inverse filter is applied for separable two-dimensional rectangular functions, with $\ell = 1.2$. The color component of a pixel is set to its maximum value if an overflow or underflow occurs in that component; otherwise the value is set to its minimum value.

Figure 6.3: Visual representation of luminance underflow and overflow when the exact inverse filter is applied for separable two-dimensional rectangular functions, with $\ell = 1.5$. The color component of a pixel is set to its maximum value if an overflow or underflow occurs in that component; otherwise the value is set to its minimum value.

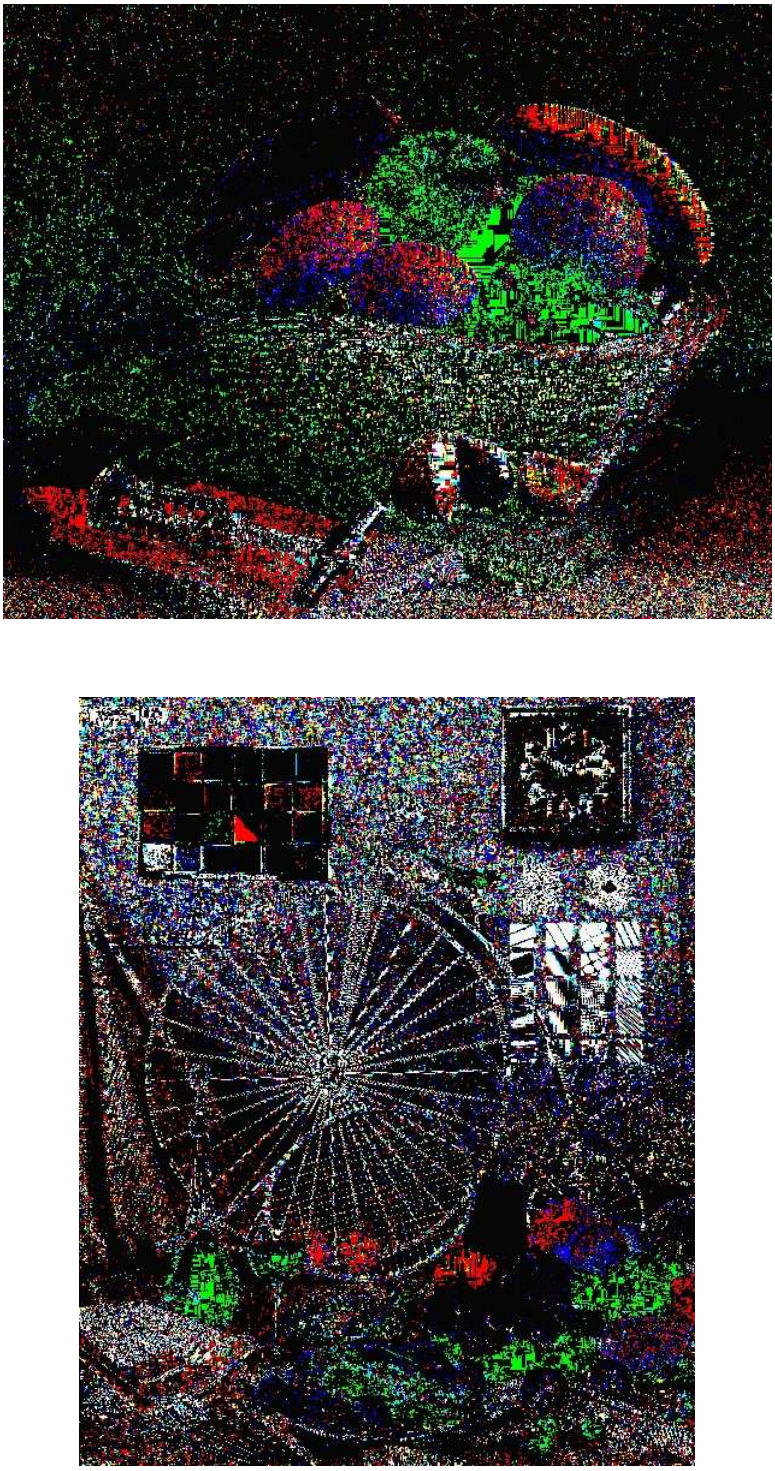

Figure 6.4: Visual representation of luminance underflow and overflow when the exact inverse filter is applied for separable two-dimensional rectangular functions, with $\ell = 1.8$. The color component of a pixel is set to its maximum value if an overflow or underflow occurs in that component; otherwise the value is set to its minimum value.

ℓ	Type	w							
		10^{-5}	0.001	0.01	0.05	0.1	0.2	0.3	0.5
1.2	A	3.1	2.3	1.2	0.3	0.1	0.0	0.0	0.0
	B	3.3	3.5	3.5	3.4	3.3	3.1	2.9	2.7
1.4	A	4.4	3.5	2.4	0.8	0.4	0.1	0.0	0.0
	B	4.6	4.9	4.8	4.5	4.2	3.7	3.4	3.0
1.6	A	6.1	5.1	3.6	1.3	0.5	0.1	0.0	0.0
	B	6.3	6.6	6.3	5.4	4.8	4.1	3.6	3.1
1.8	A	9.4	8.3	5.3	1.6	0.6	0.1	0.0	0.0
	B	9.7	9.6	8.1	6.0	5.1	4.2	3.7	3.2
2.0	A	63.1	13.9	6.1	1.6	0.6	0.1	0.0	0.0
	B	63.1	14.2	8.7	6.1	5.1	4.2	3.8	3.2
2.2	A	12.1	10.7	6.5	2.0	0.8	0.2	0.0	0.0
	B	12.4	12.0	9.1	6.0	5.0	4.0	3.6	3.1
2.4	A	11.6	10.4	7.2	2.4	0.9	0.2	0.1	0.0
	B	11.9	11.9	10.0	6.9	5.5	4.3	3.5	2.8
2.6	A	14.6	13.2	8.7	2.8	1.1	0.2	0.1	0.0
	B	14.9	14.5	11.5	7.4	5.8	4.2	3.7	3.2
2.8	A	21.5	18.5	10.0	3.0	1.2	0.3	0.1	0.0
	B	21.5	19.2	12.6	7.6	5.8	4.7	4.0	3.4
3.0	A	77.0	22.5	10.5	3.1	1.2	0.3	0.1	0.0
	B	77.0	22.8	12.8	8.0	6.3	4.9	4.2	3.4
3.2	A	26.4	22.0	11.2	3.2	1.3	0.3	0.1	0.0
	B	26.5	22.6	13.8	8.2	6.2	4.7	4.0	3.3
3.4	A	23.4	20.7	11.9	3.5	1.3	0.3	0.1	0.0
	B	23.5	21.6	14.6	8.4	6.3	4.7	3.9	3.2
3.6	A	25.4	22.4	12.5	3.7	1.4	0.3	0.1	0.0
	B	25.5	23.0	15.1	8.7	6.4	4.8	4.0	3.3
3.8	A	33.0	26.0	13.0	3.9	1.5	0.3	0.1	0.0
	B	33.0	26.4	15.3	9.0	6.7	5.0	4.2	3.4

Table 6.1: Percentage of pixels in the pre-filtered image 'fruits' that have at least one of the color components outside range [0,1]. Type A corresponds to inverse filter defined by (4.6) and type B to inverse filter defined by (4.13). One-dimensional separable inverse filter.

ℓ	Type	w							
		10^{-5}	0.001	0.01	0.05	0.1	0.2	0.3	0.5
1.2	A	4.3	3.2	1.4	0.3	0.1	0.0	0.0	0.0
	B	4.6	4.8	4.8	4.7	4.5	4.2	3.9	3.5
1.4	A	6.4	5.1	3.1	0.9	0.3	0.0	0.0	0.0
	B	6.7	6.9	6.8	6.2	5.7	5.0	4.5	3.8
1.6	A	9.6	8.3	5.4	1.5	0.5	0.0	0.0	0.0
	B	9.8	9.9	9.2	7.5	6.4	5.3	4.7	3.9
1.8	A	18.8	16.6	8.7	1.8	0.5	0.0	0.0	0.0
	B	18.9	17.7	12.4	8.1	6.7	5.4	4.7	4.0
2.0	A	98.7	33.7	9.7	1.8	0.5	0.0	0.0	0.0
	B	98.7	34.3	13.0	8.1	6.7	5.4	4.7	4.0
2.2	A	34.1	29.4	12.5	2.6	0.7	0.1	0.0	0.0
	B	34.3	30.8	16.8	8.9	6.9	5.3	4.6	3.8
2.4	A	30.9	28.0	14.9	3.4	0.9	0.1	0.0	0.0
	B	31.1	29.6	20.1	10.3	7.6	5.6	4.6	3.6
2.6	A	40.2	36.7	18.7	3.9	1.1	0.1	0.0	0.0
	B	40.3	37.9	24.0	11.1	8.0	5.7	4.7	3.8
2.8	A	59.4	52.2	20.9	4.1	1.1	0.1	0.0	0.0
	B	59.4	52.8	25.9	11.3	8.1	5.9	4.9	3.9
3.0	A	99.9	58.0	20.2	4.1	1.1	0.1	0.0	0.0
	B	99.9	58.4	24.4	11.4	8.3	6.1	5.0	4.0
3.2	A	68.7	60.4	24.7	4.6	1.2	0.1	0.0	0.0
	B	68.7	60.8	30.2	12.1	8.5	6.0	4.9	3.9
3.4	A	63.3	58.3	28.4	5.1	1.3	0.1	0.0	0.0
	B	63.3	58.9	34.5	12.8	8.7	6.0	4.8	3.8
3.6	A	67.0	61.6	30.4	5.5	1.4	0.1	0.0	0.0
	B	67.0	62.1	36.4	13.2	8.9	6.1	4.9	3.8
3.8	A	77.8	67.8	30.0	5.7	1.5	0.1	0.0	0.0
	B	77.8	68.1	35.6	13.5	9.2	6.2	5.1	3.9

Table 6.2: Percentage of pixels in the pre-filtered image 'fruits' that have at least one of the color components outside range [0,1]. Type A corresponds to inverse filter defined by (4.6) and type B to inverse filter defined by (4.13). Two-dimensional separable inverse filter.

ℓ	Type	w							
		10^{-5}	0.001	0.01	0.05	0.1	0.2	0.3	0.5
1.2	A	8.8	7.9	4.0	1.5	0.6	0.0	0.0	0.0
	B	8.9	8.9	8.9	8.5	8.0	7.4	6.8	5.8
1.4	A	12.4	11.6	8.1	2.7	1.4	0.2	0.0	0.0
	B	12.5	12.5	12.2	11.1	10.0	8.6	7.5	6.1
1.6	A	17.9	17.0	12.8	3.9	1.9	0.4	0.0	0.0
	B	18.0	17.9	16.6	13.2	11.1	8.9	7.6	6.0
1.8	A	30.5	28.7	18.6	4.7	2.1	0.3	0.0	0.0
	B	30.5	29.2	22.1	14.1	11.2	8.7	7.5	6.0
2.0	A	99.9	44.5	19.6	4.7	2.2	0.3	0.0	0.0
	B	99.9	44.7	22.9	13.8	11.1	8.7	7.4	5.9
2.2	A	44.0	40.7	24.8	6.3	2.8	0.5	0.0	0.0
	B	44.0	41.1	28.1	16.1	12.2	9.1	7.6	5.8
2.4	A	41.5	39.6	28.2	7.7	3.2	0.7	0.0	0.0
	B	41.6	40.3	31.5	18.2	13.4	9.6	7.7	5.6
2.6	A	49.9	47.4	32.7	8.9	3.6	0.8	0.0	0.0
	B	49.9	47.9	35.7	19.5	13.9	9.8	7.8	5.8
2.8	A	69.3	62.1	35.6	9.4	4.0	0.7	0.0	0.0
	B	69.3	62.3	38.3	19.8	14.2	10.1	8.0	5.8
3.0	A	99.9	69.1	34.9	9.7	4.1	0.8	0.0	0.0
	B	99.9	69.2	37.4	20.0	14.5	10.3	8.1	5.9
3.2	A	80.4	71.2	40.1	10.6	4.3	0.7	0.0	0.0
	B	80.4	71.4	42.5	21.2	14.8	10.1	7.9	5.6
3.4	A	74.4	69.2	43.8	11.5	4.3	0.8	0.0	0.0
	B	74.4	69.4	46.2	22.3	15.1	9.9	7.7	5.4
3.6	A	79.3	73.5	46.0	12.1	4.3	0.8	0.1	0.0
	B	79.3	73.6	48.2	22.9	15.1	9.9	7.7	5.4
3.8	A	91.4	81.1	46.0	12.2	4.5	0.9	0.1	0.0
	B	91.4	81.2	48.1	22.9	15.3	10.1	7.8	5.5

Table 6.3: Percentage of pixels in the pre-filtered image 'bike' that have at least one of the color components outside range [0,1]. Type A corresponds to inverse filter defined by (4.6) and type B to inverse filter defined by (4.13). Two-dimensional separable inverse filter.

Chapter 7

Finite Signal Optimization

An analysis of unconstrained sequences with finite length and that are defined via convolutions requires only simple modifications of the results of the previous sections, but using the Discrete Fourier Transform instead of the Fourier transform [5]. In this section we analyze a considerably more difficult problem: how to efficiently optimize the driver sequence taking into account the constrains of the type $c[m] \in [0, 1]$.

We maintain most of the assumptions used in the definitions used for signals in infinite spaces. However, we need to change the notation. Even though we work with two-dimensional images, it is best to formulate the problem for finite images using standard vector notation. We continue using the convention of using bold lower case letters for vectors, and bold upper case letters for matrices.

7.1 Problem Formulation

Due to the nature of the subframe superposition problem there are several options for choosing the set of pixels where light intensity is to be compared to the reference image. For instance, we can assume that the image boundaries, which include the regions that are not completely covered by all subframes, are optically blocked. In this situation only the intensity of the projected area covered by all subframes is considered, and we have a larger number of elements in the driver sequence $c[m, n]$ than in the reference sequence $r[m, n]$.

Another option is to scale the reference image according to the number of subframes that cover a pixel. For example, the reference value for a pixel covered by a third of the subframes should be divided by three. This way we can the same dimensions for all sequences.

Since we also want to consider systems with sub-critical sampling, it is more convenient to assume the first convention, that all systems have a projected region

that is larger than the reference image.

Let N_x and N_y be the number of pixels in the x and y directions, respectively. The conversion from the two-dimensional sequences to vectors is done as following. The vector $\mathbf{c}$ contains the projected pixel values, and its elements are

$$\begin{aligned} r_i &= r[\lfloor i/M_x \rfloor, i - \lfloor i/M_x \rfloor], \quad i = 0, 1, \ldots, M-1, \qquad (7.1) \\ c_j &= c[\lfloor j/N_x \rfloor - \Delta_x, j - \lfloor j/N_x \rfloor - \Delta_y], \quad j = 0, 1, \ldots, N-1, \qquad (7.2) \end{aligned}$$

where $M = M_x M_y$ and $N = N_x N_y$.

We can also define the $M \times N$ matrix $\mathbf{H}$ as

$$H_{i,j} = h[\lfloor i/M_x \rfloor, i - \lfloor i/M_x \rfloor, \lfloor j/N_x \rfloor - \Delta_x, j - \lfloor j/N_x \rfloor - \Delta_y], \qquad (7.3)$$

and in this new notation equation (3.37) is simply

$$\mathbf{s} = \mathbf{H}\,\mathbf{c}. \qquad (7.4)$$

Since we have more variables than equations, it may seem natural to just find one solution that satisfies $\mathbf{Hc} = \mathbf{r}$. However, all the results for infinite spaces show that we can expect a ill-conditioned matrix $\mathbf{H}$. In the next sections we develop optimization problems that are formulated already expecting that the optimal solution may not be exact ($\mathbf{s} \neq \mathbf{r}$), and we look for approximations that avoid overflow and underflow.

7.1.1 Unconstrained Minimization

Similar to the approach used in Section 4.2, we define the design problem as the minimization of a weighted sum of the error and a measure of coefficients' deviation from the center value:[1]

$$\text{Minimize}_{\mathbf{c}} \quad \Omega_a(\mathbf{c}) = |\mathbf{s} - \mathbf{r}|^2 + w|2\mathbf{c} - \mathbf{1}|^2 = |\mathbf{H}\,\mathbf{c} - \mathbf{r}|^2 + w|2\mathbf{c} - \mathbf{1}|^2 \qquad (7.5)$$

where $\mathbf{1}$ is the M-dimensional vector with all elements equal to one.

One advantage of this formulation is that, as long as parameter w is not zero, the problem is not singular. In addition, there is a lot of flexibility in choosing its value, according to the desired type of solution. One important drawback is that larger values of w produce images with reduced contrast.

The gradient of the objective function is

$$\nabla\Omega_a(\mathbf{c}) = 2\left(\mathbf{H}^\mathsf{T}\mathbf{H} + 4w\mathbf{I}\right)\mathbf{c} - 2\mathbf{H}^\mathsf{T}\mathbf{r} - 4w\mathbf{1}, \qquad (7.6)$$

and consequently the optimal solution is

$$\mathbf{c}^* = \left(\mathbf{H}^\mathsf{T}\mathbf{H} + 4w\mathbf{I}\right)^{-1}\left(\mathbf{H}^\mathsf{T}\mathbf{r} + 2w\mathbf{1}\right). \qquad (7.7)$$

[1] Recall that in Section 4.2 we used a zero value only to avoid infinite sums.

7.1.2 Constrained Minimization

$$\begin{array}{lrcl} \text{Minimize}_{\mathbf{c}} & \Omega_b(\mathbf{c}) & = & |\mathbf{H}\,\mathbf{c} - \mathbf{r}|^2 + w|2\mathbf{c} - \mathbf{1}|^2, \\ \text{subject to} & \mathbf{c} & \geq & \mathbf{0}, \\ & \mathbf{c} & \leq & \mathbf{1}. \end{array} \tag{7.8}$$

In this formulation we use notation conventionally used in optimization: $\mathbf{0}$ and $\mathbf{1}$ are, respectively, the M-dimensional vectors with all elements equal to 0 and 1, and vector inequalities mean constraints for each component of $\mathbf{c}$.

Because of the inequality constraints the optimal solution does not correspond to a zero gradient. The Kuhn-Tucker optimality conditions [3] for this problem are: $\mathbf{c}^*$ is an optimal solution if we have N-dimensional vectors $\mathbf{u}$ and $\mathbf{v}$ such that

$$\begin{array}{rcl} \nabla\Omega_n(\mathbf{c}^*) + \mathbf{u} - \mathbf{v} & = & \mathbf{0}, \\ \mathbf{u}^\mathsf{T}\mathbf{c}^* & = & \mathbf{u}^\mathsf{T}\mathbf{1}, \\ \mathbf{v}^\mathsf{T}\mathbf{c}^* & = & 0, \\ \mathbf{u} & \geq & \mathbf{0}, \\ \mathbf{v} & \geq & \mathbf{0}. \end{array}$$

Note that the objective function $\Omega_b(\mathbf{c})$ is quadratic, and thus convex, and the region of feasible solutions is the interior of a hypercube, which is a convex set. Thus, the local optimum defined by the conditions above corresponds to the global optimum.

7.1.3 Error Weights and Nonlinear Visual Response

Let us first define mathematically our signal optimization problem, and then explain the meaning of some new modeling components.

$$\begin{array}{lrcl} \text{Minimize}_{\mathbf{c}} & \Omega_c(\mathbf{c}) & = & w|2\mathbf{c} - \mathbf{1}|^2 + \displaystyle\sum_{i=0}^{M-1} \varpi_i \left[\nu(s_i) - \nu(r_i)\right]^2, \\ \text{subject to} & \mathbf{s} & = & \mathbf{H}\,\mathbf{c}, \\ & \mathbf{c} & \geq & \mathbf{0}, \\ & \mathbf{c} & \leq & \mathbf{1}. \end{array} \tag{7.9}$$

The objective function measures the difference between the projected and desired pixel values using a type of mean-squared-error (MSE), which is the most convenient for computational purposes. However, since the MSE is not an ideal criterion to evaluate our visual perception of distortion we add two factors that can improve the formulation without overly complicating it. First we use the fact that the human visual system is roughly sensitive to the logarithm of light intensity [34]. Thus, we use a nonlinear function $\nu(\cdot)$ to model this effect.

In addition, we consider that it is possible to pre-analyze the image, and identify regions with different quality requirements. A vector $\mathbf{w}$ with different weights for the errors different pixels allows great flexibility.

$$\nabla\Omega_c(\mathbf{c}) = 2\mathbf{H}^\mathsf{T}\mathbf{q} + 4w(2\mathbf{c} - 1), \tag{7.10}$$

where

$$q_i = \varpi_i\, \nu'(s_i)\, [\nu(s_i) - \nu(r_i)], \tag{7.11}$$

and

$$\nu'(s) = \frac{d\nu(s)}{ds}. \tag{7.12}$$

7.2 Solution Methods

We have seen in Section 7.1 that finding the optimal subframes for image superimposition requires solving an optimization problem in a very well-known form: a convex objective function, which can be simply a quadratic form, with variable "box" constraints, i.e., the only constraints are lower and upper limits on the problem's variables.

There is a large number of options for solving optimization problems with such common characteristics. For example, we can solve the primal or dual versions, use active set, interior-point solutions, penalty functions, etc. [3].

What is unusual in our application is the fact that currently images have typically millions of pixels, and thus our optimization problem has millions of variables and constraints. While this number is considerably larger than some "large-scale" problems discussed in the optimization literature, in the superimposition problem there is limited interaction between variables, in the sense that pixel values in one subframe affect only a few measured pixels in the superimposed image. Furthermore, in imaging applications we have obvious ways of exploiting sparsity by simply organizing data in two-dimensional blocks.

In the next sections we consider the problem, and show that we can use "standard" optimization techniques for solving our problem, but discuss the modifications that can exploit the particular characteristics of our problem.

7.2.1 Block-based strategy

Even when exploiting features of the problem, like matrix sparsity, the complexity of optimization methods can grow quickly with the number of variables and constraints. A strategy that is commonly used in imaging applications is to divide images in

blocks of contiguous pixels, and then solve the problem of each block in turn, using the current solution of the adjacent blocks as boundary conditions.

We call this a solution *strategy* because it can be used with any optimization method. The block should have a size that minimizes the overall computation time, and this depends on the solution method. Small blocks lead to quickly solvable subproblems, but the overall convergence is slow, while the opposite occurs with large blocks.

One additional advantage of block-based strategies is that the process can be defined so that more than one subproblem can be solved simultaneously in two or more processors.

7.2.2 Active-set methods

Active-set methods [3] correspond to process of controlling a set of inequality constraints that are defined temporarily as equality constraints, solving the problem with only equality constraints, and then analyzing the solution to identify which constraints should be added to or removed from the active set.

In our case, we have only variable-limit inequality constraints, which simplifies the active-set method considerably. All variables in the active set are set to their upper or lower limits, and then can be considered as constants, and removed from the optimization problem.

One difficulty with this approach is that the solution method may not take into account the fact that a very large number of variables are very near their limit, and at each iteration it moves in very small steps while adding the constraints of all those variables to the active set.

7.2.3 Interior-point methods

Interior-point methods have been successfully used in large-scale linear and nonlinear optimization.

One empiric, but very simple approach, is to scale the gradient according to the distance to the boundaries. If $\mathbf{g}$ is the gradient vector, and $\mathbf{c}$ the vector with bounded variables, we can use in the optimization search the values

$$\tilde{g}_i = g_i c_i (1 - c_i), \tag{7.13}$$

instead of the gradient.

7.2.4 Projection and splitting methods

Projection and splitting methods had been developed for large-scale optimization problems [26]. Basically, if we have a quadratic problem in the form

$$\begin{array}{ll} \text{Minimize}_{\mathbf{c}} & \frac{1}{2}\mathbf{c}^{\mathsf{T}}\mathbf{G}\mathbf{c} + \mathbf{q}^{\mathsf{T}}\mathbf{c}, \\ \text{subject to} & \mathbf{c} \geq \mathbf{0}, \\ & \mathbf{c} \leq \mathbf{1}. \end{array} \tag{7.14}$$

it solves the problem by solving a sequence of (possibly) simpler problems, in the form

$$\begin{array}{ll} \text{Minimize}_{\mathbf{c}} & \frac{1}{2\rho}\mathbf{c}^{\mathsf{T}}\mathbf{D}\mathbf{c} + \left[\mathbf{q} + (\mathbf{G} - \frac{1}{\rho}\mathbf{D})\hat{\mathbf{c}}\right]^{\mathsf{T}}\mathbf{c}, \\ \text{subject to} & \mathbf{c} \geq \mathbf{0}, \\ & \mathbf{c} \leq \mathbf{1}. \end{array} \tag{7.15}$$

where $\mathbf{D}$ is a diagonal matrix with positive elements, and $\hat{\mathbf{c}}$ is the previous solution.

In our superimposition problem this new optimization problem is indeed easier, because the box constraints makes it separable, and we can find the optimal value of each c_i independently.

Chapter 8

Optimal Solutions

Figure 8.1 shows examples of images that were optimally designed assuming separable systems, pixel light intensity profile $\phi(x) = b_\ell(x)$ and $\zeta(x) = b_1 x$, for different values of ℓ.

Figure 8.2 shows the images with driver signals $c[m, n]$. Note that when ℓ gets larger signals excursions have to increase to compensate for the interference between pixels.

Table 8.1 list the choices for subframe generation. The last row corresponds to the solution of the superimposition optimization problem. Fig. 8.3 shows the typical results obtained with half-pixel 2×2 superimposition, and different subframe generation methods. Comparing the superimposed images with the double-resolution original, the naïve method yields 28.9 dB PSNR, while the adjusted inverse filter (without clipping) and optimal images yield respectively 38.75 dB and 38.18 dB PSNR. When clipping is added, the adjusted inverse filter solution yields a PSNR of 36.32 dB. While this is not a complete practical solution, since it still produces overflows and underflows, the results show that it can be very useful for obtaining good estimates of the achievable improvements in resolution and quality.

Table 8.1: Choices for subframe generation.

Method	**Subframe Generation**
Naïve	identity
Linear	inverse filter
Approximation	adjusted inverse filter
Optimal	optimization solution

(a) $\ell = 2$ (2×2 subframes) (b) $\ell = 3$ (3×3 subframes)

(c) $\ell = 4$ (4×4 subframes) (d) $\ell = 5$ (5×5 subframes)

Figure 8.1: Example of optimal images.

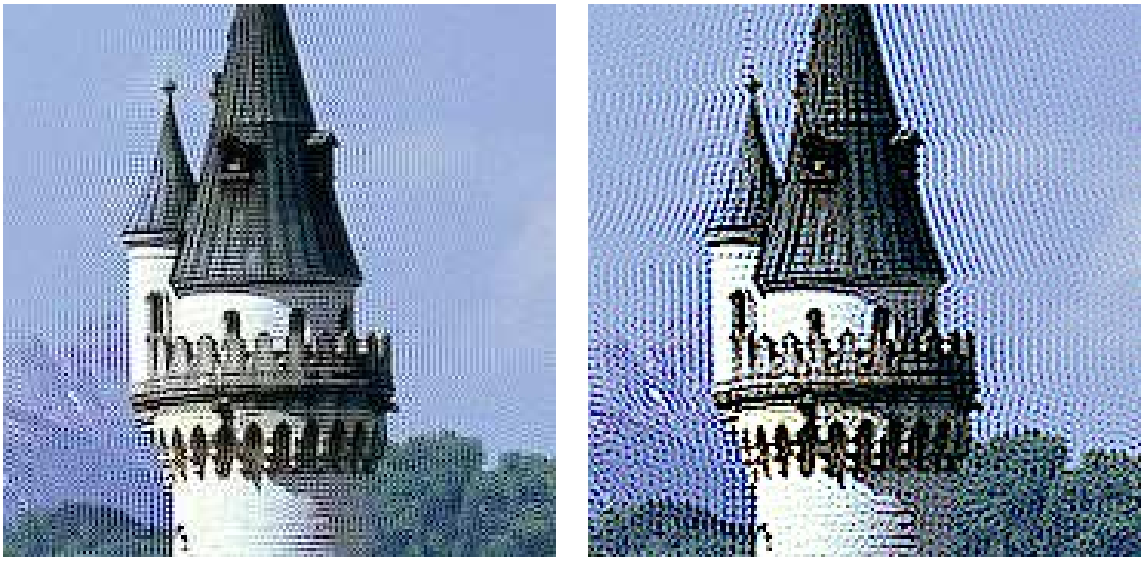

(a) $\ell = 2$ (2×2 subframes)

(b) $\ell = 3$ (3×3 subframes)

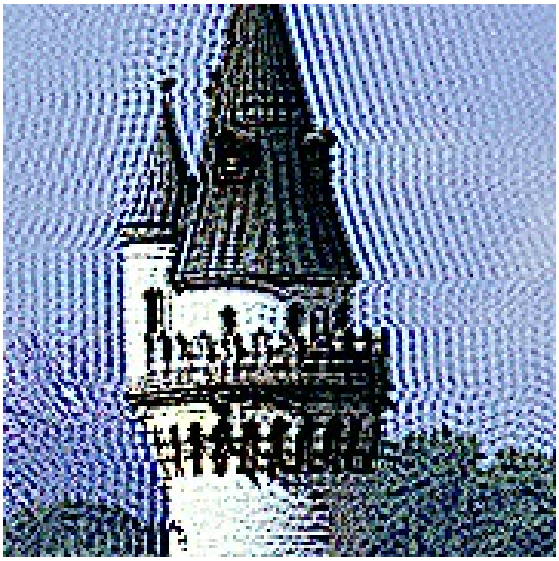

(c) $\ell = 4$ (4×4 subframes)

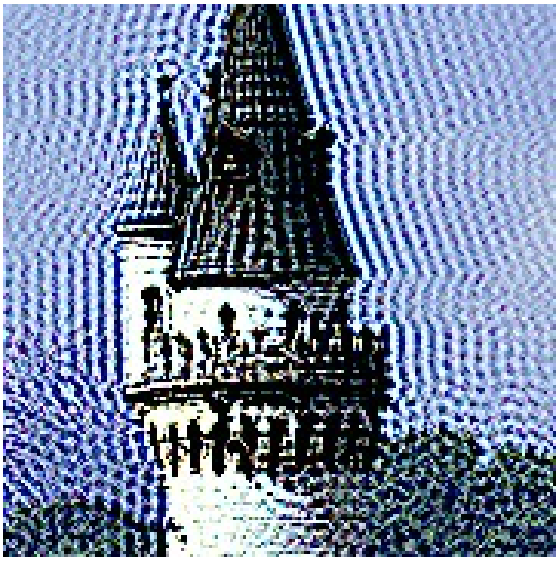

(d) $\ell = 5$ (5×5 subframes)

Figure 8.2: Example of optimal "driver" images.

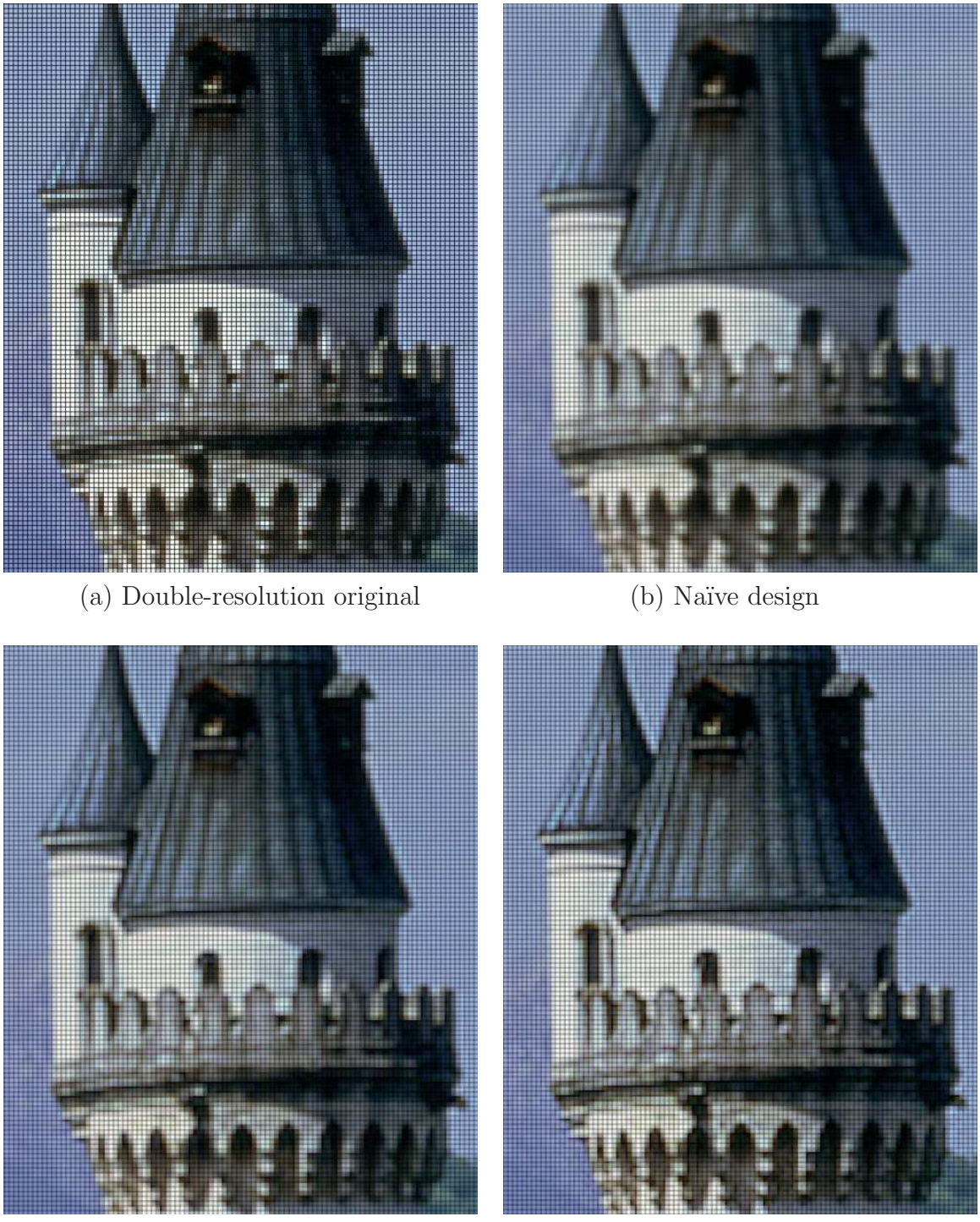

(a) Double-resolution original

(b) Naïve design

(c) Adjusted inverse filter

(d) Optimal generation

Figure 8.3: Comparison of images obtained with different subframe generation methods, half-pixel 2×2 superimposition.

Appendix A

A Simple Display Cost Analysis

The economic analysis of device costs is of course quite complicated, since it should take into consideration a large number of variables concerning markets, technology, etc. However, in some cases it is possible to show some general trends from very simple assumptions. Here we present a simplified cost analysis—of a specific scenario that applies to some of the current technologies used for displays and projectors—which provide a quantitative measure of the general economic aspects that motivate this work.

The objective is to just provide an example that is easy to understand, showing that, under very general assumptions, abrupt increases of display costs can be expected because they are a consequence of basic facts, like the inevitable occurrence of manufacturing defects.

Let us assume that the device for display or projection has N pixels, and uses a direct addressing mode. In addition, assume that due to manufacturing problems, the probability that one pixel is defective is ρ, and that defects occur independently. Under these assumptions, the probability that a manufactured device has less than D defects is

$$p_D(N) = (1-\rho)^N \sum_{k=0}^{D-1} \binom{N}{k} \left(\frac{\rho}{1-\rho}\right)^k. \tag{A.1}$$

Let $m(N)$ denote the manufacturing cost, per pixel, of the device. If the manufactured devices are discarded when D or more pixels are defective, then the final cost of each device sold, per pixel, is defined by

$$c_D(N) = \frac{m(N)}{p_D(N)}. \tag{A.2}$$

For instance, if half the devices have defective pixels and are discarded, then the final cost per device is twice the manufacturing cost of each device.

We can have a better intuition of the growth in costs using the fact that

$$e^{-\rho N} - (1-\rho)^N = \frac{\rho^2 N}{2} - \frac{\rho^3 N(3N-2)}{6} + \cdots \tag{A.3}$$

We want to consider the cases when N is large and ρ is very small, with $\rho N \leq 1$. Consequently, $\rho^2 N$ is very small and thus $e^{-\rho N}$ is a very good approximation of $(1-\rho)^N$.

Using this approximation, we can consider the case when devices are discarded when at least one pixel is defective:

$$c_1(N) \approx e^{\rho N}\, m(N). \tag{A.4}$$

Since, for the same type of technology, $m(N)$ is expected to be nearly constant, this means that the sale value, per pixel, needs to grow exponentially with the number of pixels, N.

If we use P displays or a "wobulated" projector with N/P pixels each, the rate of discarded devices decreases significantly, and we obtain a new final cost function of the type

$$c_D(N,P) = \frac{m(N,P)}{p_D(N/P)}. \tag{A.5}$$

and in particular

$$c_1(N,P) \approx e^{\rho N/P}\, m(N,P). \tag{A.6}$$

The change in the exponential factor means that there can be great cost savings, if the visual quality is somehow maintained, so that the new sale price does not depend much on P, and the combination is done with small increase in the device cost, so that $m(N,P)$ is also weakly dependent on P.

Figure A.1 shows how the cost factor increases with the average number of defects, ρN. We can see that any technique that allows increasing maximum number of defects for rejection, D, also results in great economic gains.

Note that in the cost we consider only one aspect—manufacturing defects in single pixels—which may not be important for all technologies. However, in all cases there are important factors, like signal distribution, power consumption, etc., which also tend to grow steeply when resolution increases.

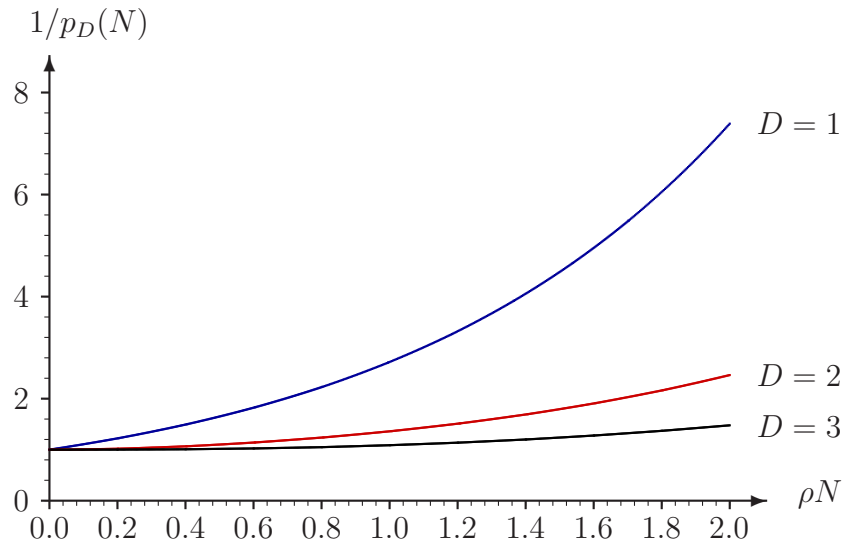

Figure A.1: Simplified model of increase in cost due to manufacturing defects, according to average number of defective pixels, ρN, and maximum number for rejection, D.

Appendix B

Display Gamma Compensation

The gamma (γ) correction was introduced because in the television CRT displays the luminance is a nonlinear function of the input signal, in the form [18, § 5.1]

$$I = av^{\gamma} + b, \tag{B.1}$$

where I is light intensity, $v \in [0, 1]$ is the video signal, a and b are constants related to gain and black level, and γ is a factor commonly in the range from 2.2 to 2.8 (and less frequently in the range from 1 to 3).

This nonlinearity is due to the way the CRT's electronics control the electron beam, and not the phosphor. Since television standards were created in a time when correction circuitry would be expensive, it was decided that the signals would be corrected before transmission.

Standards ITU-R BT.709 and SMPTE-170M defines $\gamma = 2.22$ and the following conversion between pixel value ($p \in [0, 255]$) and luminance ($r \in [0, 1]$) [18, § 10.2]

$$p = 255 \times \begin{cases} 4.5\, r, & 0 \le r < 0.018, \\ 1.099\, r^{0.45} - 0.099, & 0.018 \le r \le 1, \end{cases} \tag{B.2}$$

and its inverse is

$$r = \begin{cases} 8.715 \cdot 10^{-4}\, p, & 0 \le p < 20.66, \\ (3.568 \cdot 10^{-3}\, p + 0.09)^{2.22}, & 20.66 \le p \le 255, \end{cases} \tag{B.3}$$

Figure B.1 shows the curve used for conversion.

The standard SMPTE-240M uses the same value of γ, but with a different conversion

$$p = 255 \times \begin{cases} 4\, r, & 0 \le r < 0.0228, \\ 1.1115\, r^{0.45} - 0.1115, & 0.0228 \le r \le 1, \end{cases} \tag{B.4}$$

The PAL and SECAM video standards use $\gamma = 2.8$.

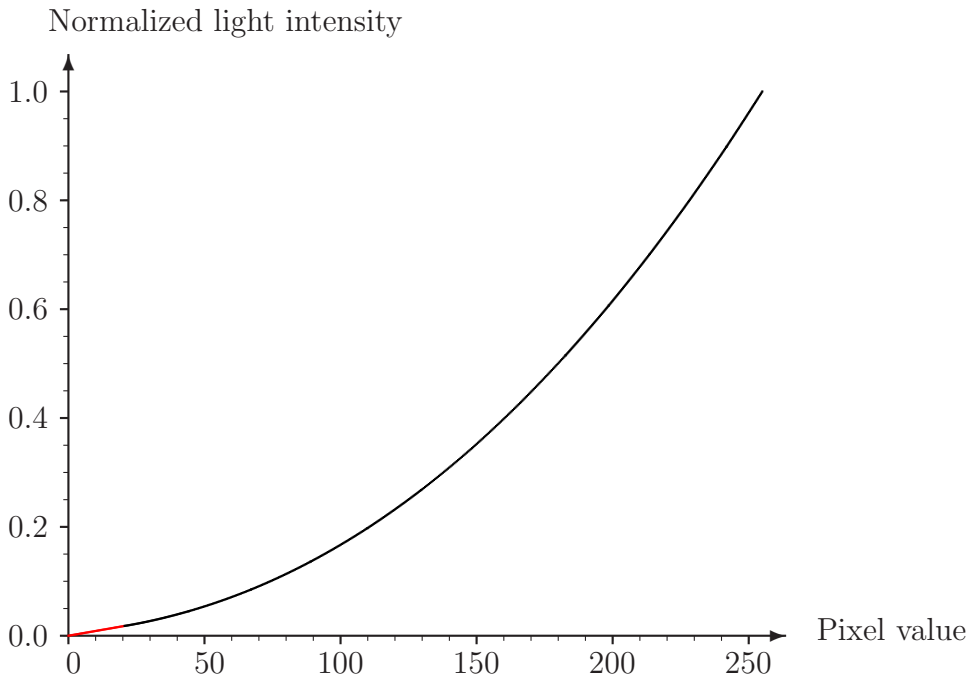

Figure B.1: Conversion from pixel value to normalized light intensity, according to standards ITU-R BT.709 and SMPTE-170M. The red line is the linear part.

Appendix C

Visual System Factors

There are several psychovisual factors related to the human visual system (HVS) that need to be considered when designing imaging systems, which cannot be possibly covered in a small space in this document. In this Appendix we cover only some of the most basic facts, to help make clear the distinction between the mathematical constraints that can be very important in other types of signal processing applications, and the subjective visual quality.

The HVS has limitations and characteristics that can be exploited for cost reduction, without visible quality degradation. One important characteristic is how contrast sensitivity varies with spatial frequency. The main main effect can be easily perceived with images like the one shown in Figure C.1.

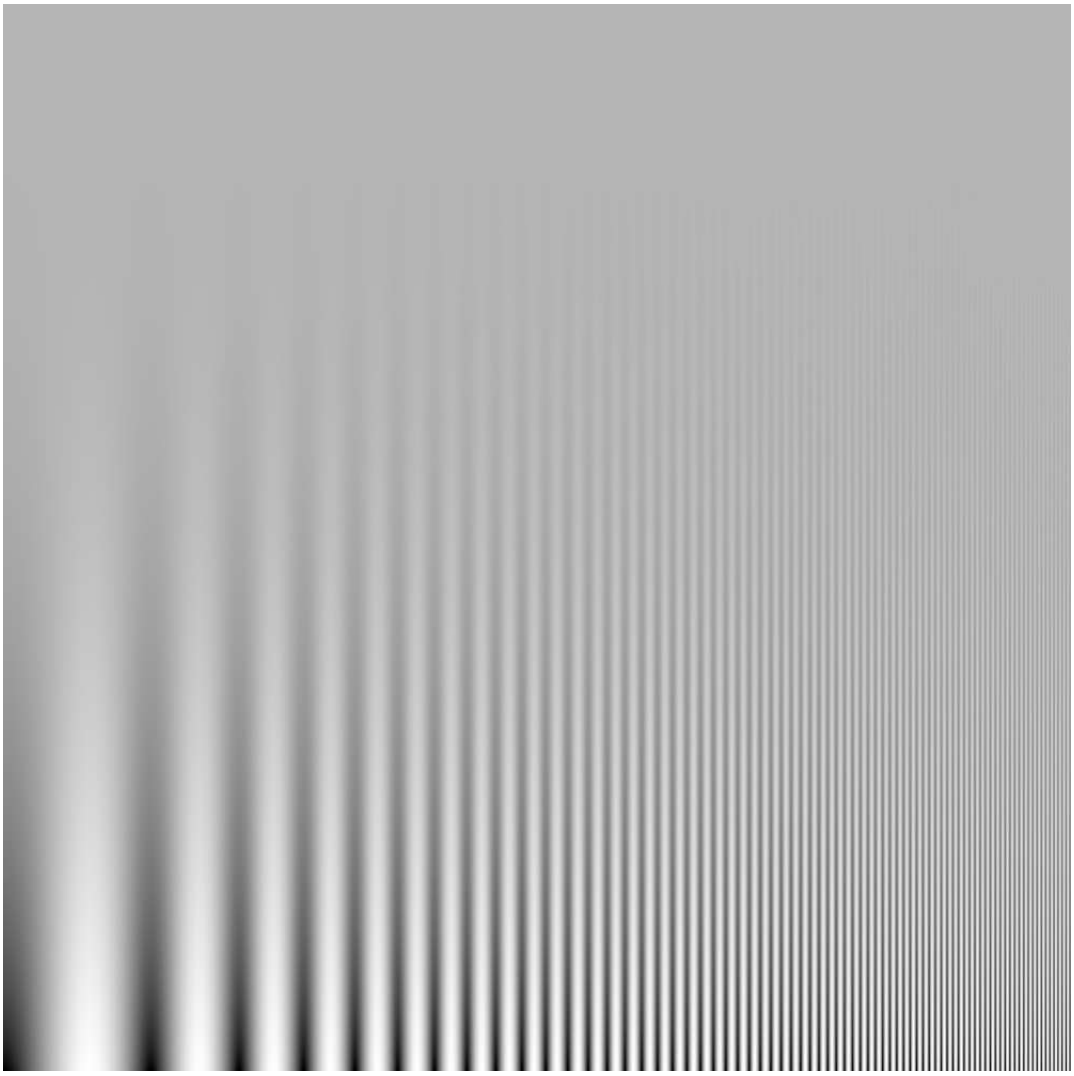

Figure C.1: Image showing how contrast sensitivity varies with spatial frequency.

Appendix D

Discussion of Super-resolution

The term "super-resolution" has been used for techniques that combine several slightly shifted images (or video) of the same scene, in order to obtain an image with higher resolution [38]. In this case, we can say that super-resolution is achieved when some frequency components that are truly present in the original image and that cannot be obtained from simple linear interpolation, are recovered from the multiple measurements. In this case, even very modest improvements over linear interpolation are commonly called super-resolution, since they are, after all, "true" gains in the quality of the acquired image.

This problem is clearly related to the image superimposition problem, since it aims to integrate the information available in a set of low-resolution measurements (in a form of post-processing) in order to obtain an improved image of higher resolution. Basically, in one case we have a set of known low-resolution images, and want to find the high-resolution image that should have generated them, and in the other case the high-resolution image is known, and we want to find the low-resolution versions (pre-processing) that can be combined to generate it.

However, there are two very important differences. For image acquisition, the positions of the low-resolution images are commonly unknown, and have to be estimated, and the resulting uncertainty can greatly reduce the gains [38]. As discussed in Chapter 4, the image superimposition problem would correspond to inverse filtering if there were no limits on the light intensity of each projected pixel, but the inclusion of those constraints can also greatly reduce the technique's effectiveness.

The term super-resolution had not been used for displays or projectors, since the superimposition technique is not well known, and it makes little sense to use it for tiling. In fact, it is very easy to see that, whatever the criterion used for defining the resolution of a single projector, with tiling it is very clear that that resolution is scaled up by integer factors defined by the number of images tiled in the horizontal and vertical direction. Superimposition, on the other hand, changes the pixel light

intensity profile (or pixel point spread function), so the discussion of resolution has to start from very basic definitions.

While it is normally quite complicated to measure true resolution and to compare the visual quality of systems with different pixel light intensity profiles [37], these tasks are even more difficult for image superimposition since there is a nonlinear component in their optimal design, and results are image-dependent. Thus, we believe that for projectors it makes sense to use the term super-resolution in the same loose way that is used for cameras, i.e., say that super-resolution is achieved simply when it is possible to improve quality over a baseline system by adding high frequency components that are true to the original.

In a paper by A. Majumder, called "Is spatial super-resolution feasible using overlapping projectors?" [43], the author reaches the conclusion that in theory super-resolution is possible, but only under such stringent conditions that it is not feasible in practice. In this appendix we discuss the content of that paper to see how its results are related to our work.

While Majumder does not use the term super-resolution in the same way as we explained above, we have difficulty understanding what exactly are the projection system requirements that are desired. As we explain below, we possibly disagree with the assumptions, method, and conclusions in [43].

Our notation is different, but the first part of [43] simply revises sampling theory. For example, while in [43] we have eq. (2), describing a periodic spectrum $C(f)$ defined from a strictly bandlimited signal spectrum $P(f)$, as

$$C(f) = P\left(f - \left\lfloor \frac{f}{f_s} + \frac{1}{2} \right\rfloor f_s\right) \tag{D.1}$$

while we would use a notation like

$$C(f) = P(e^{j2\pi f}). \tag{D.2}$$

We prefer this form because in practice optical signals are never truly bandlimited. Thus, instead of making such assumption, we just use the Fourier transform of the discrete signal sequence.

In Section 2.2 we present our more detailed models for image acquisition and reconstruction, while in [43] the whole process is condensed to the use of periodic comb functions. While it is difficult to understand if our assumptions are also assumed implicitly in [43], below we discuss two main difficulties.

First, the derivation in [43] does not use Dirac's delta functions $\delta(f)$ and Dirac's comb. While the intent is clear, here we redefine the notation using those functions. Dirac's comb $s(t)$ with period T is defined by

$$s(t) = \sum_{k=-\infty}^{\infty} \delta(t - kT) \tag{D.3}$$

and its transform is another Dirac's comb,

$$S(f) = \frac{1}{T} \sum_{n=-\infty}^{\infty} \delta(f - n/T). \tag{D.4}$$

Next, in [43] the analysis of two superimposed projections is modeled simply with the addition of two comb functions, shifted by a distance $l \leq T$. In the spatial domain we have

$$s_o(t) = s(t) + s(t - l), \tag{D.5}$$

which results in

$$\begin{aligned} S_o(f) &= (1 + e^{-j2\pi fl})S(f) \\ &= \sum_{n=-\infty}^{\infty} (1 + e^{-j2\pi fl})\delta(f - n/T) \\ &= \sum_{n=-\infty}^{\infty} (1 + e^{-j2\pi nl/T})\delta(f - n/T). \end{aligned} \tag{D.6}$$

In [43] this transform is defined by simply using its real component, which is

$$\begin{aligned} \Re\{S_o(f)\} &= \sum_{n=-\infty}^{\infty} [1 + \cos(2\pi nl/T)]\delta(f - n/T) \\ &= 2 \sum_{n=-\infty}^{\infty} \cos^2(\pi nl/T)\delta(f - n/T). \end{aligned} \tag{D.7}$$

This difference in results is not very important for the next discussion in [43]. It is assumed that the desired double-resolution signal has Fourier transform $P_o(f)$, and is strictly bandlimited to interval $f \in [-1/T, 1/T]$. The spectrum of the superimposed image $C_o(f)$ is then defined by the convolution[1]

$$\begin{aligned} C_o(f) &= (P_0 * S_o)(f), \\ &= \sum_{n=-\infty}^{\infty} (1 + e^{-j2\pi nl/T})P_o(f - n/T). \end{aligned} \tag{D.8}$$

It is concluded that in the general case there is always a "contamination" of the periodic spectrum, due to the sum of factors $P_o(f - n/T)$. The only exception, i.e., the only case when there is no "contamination" is

$$l = T/2 \quad \Longrightarrow \quad S_o(f) = 2S(f/2) \quad \Longrightarrow \quad C_o(f) = 2 \sum_{n=-\infty}^{\infty} P_o(f - 2n/T). \tag{D.9}$$

[1]We do not understand how exactly this periodic spectrum corresponds to our model of the projected image, but this is not necessary for the discussion here.

The problem with this approach and conclusion is that it does not assume any form of preprocessing, and ignores the fact that the "contamination" effects can be undone.

For instance, since $P_o(f)$ is strictly bandlimited and should have Hermitian symmetry, we can derive the equations

$$\begin{aligned} C_o(f) &= 2P_o(f) + wP_o^*(1/T - f), \\ C_o^*(1/T - f) &= w^*P_o(f) + 2P_o^*(1/T - f), \end{aligned} \tag{D.10}$$

where the asterisk indicates the complex conjugate and $w = 1 + e^{-j2\pi l/T}$. This system has solutions when

$$\begin{vmatrix} 2 & w \\ w^* & 2 \end{vmatrix} = 4 - |w|^2 = 2 - 2\cos(2\pi l/T) \neq 0. \tag{D.11}$$

Thus, except when $l = 0$ and when $l = T$, whatever the values desired for the periodic $C_o(f)$, we can solve the system of equations above to find $P_o(f)$ that will produce the desired results. (Note that this is similar to the frequency-domain design of Section 4.3.) The case $l = T/2$ is simply the case when the matrix above is a multiple of the identity matrix. Maybe it was chosen in [43] as the only solution because the author was unaware techniques for aliasing cancellation, or decided that only trivial solutions are practically acceptable.

What comes next in [43] seems like an extension of this assumption, requiring not only $l = T/2$, but also non-overlapping superimposition, which is equivalent to using optical signals that are spatially orthogonal, so that again no preprocessing is needed. However, it is strange that all the previous discussions were about strictly bandlimited signals, which must have infinite spatial support, and orthogonality is achieved via signals like the $\mathrm{sinc}(x)$ function. There is no explanation of what this jump from frequency to spatial domain means. Both cases, corresponding to signals that are orthogonal in space or frequency, can be considered those that have trivial solutions.

In our model for image superimposition, as shown in the diagram of Figure 3.4, we assume the presence of a subframe generation block, which should be used for reducing the effects of the superimposition that degrade quality. Maybe the main disagreement is in our assumption that since there is limited control of the spectral content of optical signals, some aliasing and presence of signal harmonics is inevitable, but we cannot say that there is no value in the superimposition technique. We can still design signals that minimize those distortions, and produce images with clearly better visual quality.

Bibliography

[1] C.R. Rao and S.K. Mitra, *Generalized Inverse of Matrices and Its Applications*, Wiley, 1971.

[2] H.C. Andrews and B.R. Hunt, *Digital Image Restoration*, Prentice Hall, 1977.

[3] P.E. Gill, W. Murray, and M.H. Wright, *Practical Optimization*, Academic Press, 1981.

[4] W.F. Schreiber and D.E. Troxel, "Transformation between continuous and discrete representations of images: a perceptual approach," *IEEE Trans. Pattern Analysis and Machine Intelligence,* vol. 7, pp. 178–186, March 1985.

[5] A.V. Oppenheim and R.W. Schafer, *Discrete-Time Signal Processing*, Prentice Hall, 1989.

[6] D.P. Mitchell and A.N. Netravali, "Reconstruction filters in computer graphics," *Proc. ACM SIGGRAPH Computer Graphics,* vol. 22(4), pp. 221–228, June 1988.

[7] J.G. Proakis, *Digital Communications*, 2nd. ed., McGraw-Hill, 1989.

[8] A.K. Jain, *Fundamentals of Digital Image Processing*, Prentice Hall, 1989.

[9] S. Barnett, *Matrices: Methods and Applications*, Oxford University Press, 1990.

[10] C.G. Han, P.M. Pardalos, and Y. Ye, "Computational aspects of an interior point algorithm for quadratic problems with box constraints," in T. Coleman and Y. Li (eds.) *Large-Scale Numerical Optimization*, SIAM, 1990.

[11] C. Cruz-Neira, D.J. Sandin, T.A. DeFanti, R.V. Kenyon, and J.C. Hart, "The CAVE: audio visual experience automatic virtual environment," *Comm. ACM,* vol. 35, pp. 64–72, June 1992.

[12] P.P. Vaidyanathan, *Multirate Systems and Filter Banks* Prentice Hall, 1993.

[13] W.H. Press, S.A. Teukolsky, W.T. Vetterling, and B.P. Flannery, *Numerical Recipes in C: The Art of Scientific Computing*, 2nd ed., Cambridge University Press, 1993.

[14] O. Axelsson, *Iterative Solution Methods*, Cambridge University Press, 1994.

[15] G.E. Andrews, *Number Theory*, Dover Publications, Inc., 1994.

[16] A.P. Kadonaga, *Multiple Pass Printing for Achieving Increased Print Resolution,* US Patent 5,469,198, Nov. 1995 (filed Aug. 1992).

[17] Y. Takahashi, T. Nomura, and S. Sakai, "Optical system and characteristics of an LCD projector with interleaved pixels using four LCD projectors," *IEEE Trans. Circuits and Systems for Video Technology,* vol. 5, pp. 41–47, Feb. 1995.

[18] B.G. Haskell, A. Puri, and A.N. Netravali, *Digital Video: An Introduction to MPEG-2*, Chapman & Hall, New York, 1996.

[19] C.L. Holstun, R.A. Askeland, F. Drogo, and B.P. Canfield, *Method for Increased Print Resolution in the Carriage Scan Axis of an Inkjet Printer,* US Patent 5,541,625, July 1996 (filed June 1994).

[20] D.C. Towery, A.E. Cariffe, J.E. Mebane, A.P. Kadonaga, I-S. Chen, and M. Overton, *Double Axis Dot Depletion for 600 DPI Edge Acuity with 300 DPI Print Cartridge* US Patent 5,574,832, Nov. 1996 (filed April 1993).

[21] E.R. Tufte, *Visual Explanations: Images and Quantities, Evidence and Narrative,* Graphics Press, Cheshire, Connecticut 1997.

[22] I. Iglesias, N. Lopez-Gil, and P. Artal, "Reconstruction of the point-spread function of the human eye from two double-pass retinal images by phase-retrieval algorithms," *J. Opt. Soc. Am. A: Opt. Image Sci. Vis.,* vol 15(2), pp. 326–339, Feb. 1998.

[23] R.C. Staunton, "Edge operator error estimation incorporating measurements of CCD TV camera transfer function," *IEE Proc. – Vision, Image and Signal Processing,* vol. 145, pp. 229–235, June 1998.

[24] J. Adams, K. Parulski, and K. Spaulding, "Color processing in digital cameras," *IEEE Micro,* vol. 18, pp. 20–30, Nov.-Dec. 1998.

[25] S.K. Card, J.D. Mackinlay, and B Shneiderman, eds., *Readings in Information Visualization: Using Vision to Think,* Morgan Kaufmann Publishers, San Francisco, California, 1999.

[26] V. Ruggiero and L. Zanni, "Variable Projection Methods for Large Convex Quadratic Programs," in *Recent Trends in Numerical Analysis* (D. Trigiante ed.), Nova Science Publishers Inc., pp 299–313 2000.

[27] C. Ware, *Information Visualization: Perception for Design,* Morgan Kaufmann Publishers, San Francisco, California, 2000.

[28] J. Jan, *Digital Signal Filtering, Analysis and Restoration,* INSPEC, Inc., 2002.

[29] B. Wei, C. Silva, E. Koutsofios, S. Krishnan, and S. North, "Visualization research with large displays," *IEEE Computer Graphics and Applications,* vol. 20, pp. 50–54, July 2000.

[30] M. Hereld, I.R. Judson, and R.L Stevens, "Introduction to building projection-based tiled display systems," *IEEE Computer Graphics and Applications,* vol. 20, pp. 22–28, July 2000.

[31] D.R. Schikore, R.A. Fischer, R. Frank, R. Gaunt, J. Hobson, and B. Whitlock, "High-resolution multiprojector display walls," *IEEE Computer Graphics and Applications,* vol. 20, pp. 38–44, July 2000.

[32] Y. Chen, D.W. Clark, A. Finkelstein, T.C Housel, and K. Li, "Automatic alignment of high-resolution multi-projector displays using an uncalibrated camera," *Proc. IEEE Visualization,* pp. 125–130, Oct. 2000.

[33] E.R. Tufte, *The Visual Display of Quantitative Information,* 2nd. ed., Graphics Press, Cheshire, Connecticut 2001.

[34] R.C. Gonzalez and R.E. Woods, *Digital Image Processing*, 2nd. ed., Prentice Hall, 2002.

[35] K. Isakovic, T. Dudziak, and K. Köchy, "X-Rooms : A PC-based immersive visualization environment," *Proc. Web3D 2002 Symposium* (ACM SIGGRAPH publication), pp. 173-177, Tempe, Arizona, Feb. 2002.

[36] H. Chen, R. Sukthankar, G. Wallace, and K. Li, "Scalable alignment of large-format multi-projector displays using camera homography trees," *Proc. IEEE Visualization,* 2002.

[37] C.P. Fenimore and A.I. Nikolaev, "Assessment of resolution and dynamic range for digital cinema," *Proc. of SPIE,* vol. 5022, Jan. 2003.

[38] S.C. Park, M.K. Park, and M.G. Kang, "Super-resolution image reconstruction: a technical overview," *IEEE Signal Proc. Mag.,* pp. 21-36, May 2003.

[39] J. Duhl, R. Kirzner, S.D. Hendrick, S. Feldman, and J. Rahal, *Worldwide Interactive Data Visualization Tools Forecast, 2002–2007,* IDC Market Analysis Report, Framingham, Massachusetts, 2003.

[40] S. Khatri, *Large Screen Displays, Annual Report,* Stanford Resources, San Jose, California, 2003.

[41] C. Poynton, *Digital Video and HDTV: Algorithms and Interfaces,* Morgan Kaufmann Publishers, San Francisco, California, 2003.

[42] C. Li, H. Lin, and J. Shi, "A survey of multi-projector tiled display wall construction," *Proc. 3rd IEEE Int. Conf. Image and Graphics,* pp. 452–455, Dec. 2004.

[43] A. Majumder, "Is spatial super-resolution feasible using overlapping projectors?," *Proc. IEEE Int. Conf. Acoustics, Speech, and Signal Processing,* vol. 4, pp. 209–212, March 2005.

[44] W. Allen and R. Ulichney, "Wobulation: doubling the addressed resolution of projection displays," *SID Symposium Digest of Technical Papers,* vol. 36, pp. 1514–1517, May 2005.